Engineering and Applied Science Theses & Dissertations

McKelvey School of Engineering

Spring 5-15-2018

Developing Photoacoustic Tomography Devices for Translational Medicine and Basic Science Research

Tsz Wai Wong
Washington University in St. Louis

Follow this and additional works at: https://openscholarship.wustl.edu/eng_etds

Part of the Bioimaging and Biomedical Optics Commons, and the Optics Commons

WASHINGTON UNIVERSITY IN ST. LOUIS

School of Engineering and Applied Science
Department of Biomedical Engineering

Dissertation Examination Committee:
Lihong V. Wang, Co-Chair
Mark A. Anastasio, Co-Chair
Deborah V. Novack
Jung-Tsung Shen
Lan Yang

Developing Photoacoustic Tomography Devices for
Translational Medicine and Basic Science Research
by
(Terence) Tsz Wai Wong

A dissertation presented to
The Graduate School
of Washington University in
partial fulfillment of the
requirements for the degree
of Doctor of Philosophy

May 2018
St. Louis, Missouri

Table of Contents

List of Figures

Acknowledgments

I would like to express my sincere thanks to my advisor Prof. Lihong V. Wang, for his support, patience, and guidance throughout my Ph.D. journey. It has been my greatest honor to be his student, learning the way to perform first-rate research, understanding the importance of a positive attitude, and experiencing the significance of solving vital medical/scientific problems. I treasure everything I learned from him and this excellent platform. I would also like to say thank you to many lab members for their generous help, including Ruiying Zhang, Liren Zhu, Pengfei Hai, Hsun-Chia Hsu, Yang Li, Junhui Shi, Xiaowei Liu, Toru Imai, Yuecheng Shen, Chi Zhang, Junjie Yao, Lidai Wang, Konstantin Maslov, Garcia-Uribe Alejandro, and Yong Zhou. Without their inspirations and supports, my work cannot be accomplished smoothly.

I am thankful to my committee members, Drs. Mark Anastasio, Deborah Novack, Jung-Tsung Shen, and Lan Yang. Especially, I thank Dr. Deborah Novack for her patience and help for my medical project; I thank Dr. Mark Anastasio for his valuable advice through the progress of my thesis; I thank Drs. Jung-Tsung Shen and Lan Yang for their valuable advice and supports.

Last but certainly not least, I owe my special thanks to my friends, family, and fiancée for their boundless loves, constant encouragements, and unconditioned supports, which have made this dissertation possible.

(Terence) Tsz Wai Wong

Washington University in St. Louis

May 2018

Dedicated to my family and fiancée

ABSTRACT OF THE DISSERTATION

Developing Photoacoustic Tomography Devices for

Translational Medicine and Basic Science Research

by

(Terence) Tsz Wai Wong

Doctor of Philosophy in Biomedical Engineering

Washington University in St. Louis, 2018

Professor Lihong V. Wang, Co-Chair

Professor Mark A. Anastasio, Co-Chair

Photoacoustic (PA) tomography (PAT) provides volumetric images of biological tissue with scalable spatial resolutions and imaging depths, while preserving the same imaging contrast—optical absorption. Taking the advantage of its 100% sensitivity to optical absorption, PAT has been widely applied in structural, functional, and molecular imaging, with both endogenous and exogenous contrasts, at superior depths than pure optical methods. Intuitively, hemoglobin has been the most commonly studied biomolecule in PAT due to its strong absorption in the visible wavelength regime.

One of the main focuses of this dissertation is to investigate an underexplored wavelength regime—ultraviolet (UV), which allows us to image cell nuclei without labels and generate histology-like images naturally from unprocessed biological tissue. These preparation-free and easy-to-interpret characteristics open up new possibilities for PAT to become readily applicable to other important biomedical problems (e.g., surgical margin analysis, Chapter 2) or basic science studies (e.g., whole-organ imaging, Chapter 3). For instance, we developed and optimized a PA microscopy system with UV laser illumination (UV-PAM) to achieve fast, label-free,

multilayered, and histology-like imaging of human breast cancer in Chapter 2. These imaging abilities are essential to intraoperative surgical margin analysis, which enables promptly directed re-excision and reduces the number of repeat surgeries.

We have incorporated the Grüneisen relaxation (GR) effect with UV-PAM to improve the performance of our UV-PAM system (e.g., the axial resolution), thus providing more accurate three-dimensional (3D) information (Chapter 4). The nonlinear PA signals caused by the GR effect enable optical sectioning capability, revealing important 3D cell nuclear distributions and internal structures for cancer diagnosis.

In the final focus of this dissertation, we have implemented a low-cost PA computed tomography (PACT) system with a single xenon flash lamp as the illumination source (Chapter 5). Lasers have been commonly used as illumination light sources in PACT. However, lasers are usually expensive and bulky, limiting their applicability in many clinical usages. Therefore, the use of a single xenon flash lamp as an alternative light source was explored. We found that PACT images acquired with flash lamp illumination were comparable to those acquired with laser illumination. This low-cost and portable PACT system opens up new potentials, such as low-cost skin melanoma imaging in undeveloped countries.

Chapter 1 Introduction

This chapter introduces the two primary imaging modes of photoacoustic tomography (PAT): photoacoustic microscopy (PAM) and photoacoustic computed tomography (PACT). The motivations of developing novel PAT systems to address different biomedical problems for translation medicine and basic science research are then discussed.

1.1 Introduction to Photoacoustic Tomography

In PAT, when biological tissue is excited by laser pulses, laser energy is absorbed by biomolecules and converted into heat through non-radiative relaxation. The heat is further converted to a pressure rise through thermoelastic expansion. The initial pressure rise propagates as an ultrasound wave in the tissue, which is referred to as a photoacoustic (PA) wave[1,2]. An ultrasonic transducer or transducer array is used to detect the PA waves. Subsequently, the detected PA signals are used to reconstruct an image that maps the original optical energy deposition on the biological tissue. Due to low ultrasonic scattering, PAT indirectly improves tissue transparency by ~1,000 times, consequently breaking the diffusion limit (~1 mm in depth) and achieving multiple-centimeter deep tissue imaging with rich optical absorption contrast. Furthermore, the image resolution and penetration depth of PAT are highly scalable with ultrasonic frequency, which is the only imaging modality that can fill the gap between microscopic and macroscopic images.

PAT can be categorized into two primary imaging modes: PAM and PACT. In a standard PAM configuration, a laser light is focused onto the biological tissue. A single-element focused ultrasonic transducer is confocally-aligned with the laser focal spot for sensitive detection. By

1

raster scanning the specimen, a three-dimensional PAM image can be reconstructed. In a usual PACT configuration, a broad laser beam is needed for illumination. The light is scattered and diffused into the biological tissue. Parallel detection by a multi-element ultrasonic transducer array is commonly used. Each single laser shot generates one PACT image. In both PAM and PACT, the PA amplitude is proportional to the optical absorption coefficient of the absorber in units of m^{-1}, the non-radiative quantum yield, and the local optical fluence (or exposure) in the unit of J/m^2. In addition, other biological information can also be extracted from the measured PA signals, such as elastography[3–5], temperature[6], and pH value[7].

1.2　Motivations

Chapter 2 describes the development and optimization of a PAM system with ultraviolet (UV) laser illumination for achieving label-free multilayered histology-like imaging of unprocessed human breast cancer. The rich DNA/RNA absorption at the UV wavelength enables UV-PAM to reveal histology-like contrast without sample preparation and labeling. UV-PAM holds promise as an intraoperatively imaging tool that allows immediate directed re-excision, reducing the number of repeat surgeries.

Chapter 3 explores the full potential of applying PAM system for whole-organ imaging. To reveal details of whole organs (e.g., a mouse brain, lung, and kidney) with microscopic resolution, we developed microtomy-assisted photoacoustic microscopy (mPAM) to acquire serial distortion-free and registration-free images with endogenous absorption contrasts. Dual-wavelengths have also been employed to image different biomolecules. mPAM offers a new way to better understand complex biological organs.

2

Chapter 4 introduces the idea of combining Grüneisen relaxation (GR) effect with UV-PAM to improve the axial resolution for accurate three-dimensional (3D) information visualization. Conventionally, PAM provides superior lateral resolution, which is governed by the diffraction limit of light. However, the axial resolution is determined ultrasonically. We introduced GRUV-PAM to obtain optically defined axial resolution for revealing detailed 3D cell nuclear distributions and internal structures, which are important diagnostic features for cancers.

Chapter 5 demonstrates the possibility of building a low-cost PACT system with a xenon flash lamp illumination for facilitating the development of PAT in clinical usage. Traditionally, a laser is needed as the light source for PACT. However, lasers are usually expensive and bulky, hindering the rapid clinical dissemination of PAT. We demonstrated that an alternative light source–a single xenon flash lamp can be used, getting images comparable to that obtained with a laser. This replacement drastically reduces the cost and improves the portability, potentially facilitating the translational development of PAT in clinics.

Chapter 6 summarizes all the findings in different chapters. The future research directions for each work are also discussed.

Chapter 2 Photoacoustic Microscopy for Label-free Fast Histology of Human Breast Cancer

This chapter describes the possibility of applying photoacoustic microscopy for speeding up the tumor margin analysis, providing intraoperative feedbacks to surgeons during the initial surgery. Currently, the standard of care requires post-operative pathology to ensure complete cancer removal, which normally takes days for lengthy sample preparation procedure, causing 20–60% of patients undergoing second surgeries to achieve clear margins. Intuitively, a label-free imaging modality which can provide histology-like images of unprocessed tissue could potentially solve this challenging medical problem, revolutionizing the surgical practice. In this chapter, we demonstrate that by taking advantage of the intrinsic optical contrast of unprocessed breast tissue, photoacoustic microscopy can achieve multilayered histology-like imaging of the tissue surface and subsurface. The work in this chapter has been published in *Science Advances*[8].

2.1 Background

In 2017, an estimated ~250,000 new cases of invasive and non-invasive breast cancer were diagnosed in US women[9]. Of these, 60–75% were treated with breast conserving surgery (BCS) as the initial therapy. The goal of BCS is to excise the tumor with a rim of normal surrounding tissue, so that no cancer cells remain at the cut margin (a negative margin, **Fig. 2.1a**), while preserving as much normal breast tissue as possible. The current standard is to find no tumor at

the edge of the specimen via histological analysis[10], because negative margins reduce the local recurrence rate[11–13]. Thus, those patients with cancer cells at the cut margin (a positive margin, **Fig. 2.1b**) most commonly require a second surgical procedure to obtain clear margins. Re-excision surgeries increase health care costs and the risk of complications, burden patients physically and psychologically, and potentially delay recommended adjuvant treatment. Several approaches have been used to decrease the positive margin rate to avoid re-excision[14,15]. However, these techniques may be ineffective in reducing the re-operative rate[16–20], difficult to master by surgeons[21], or time-consuming for large specimens[22,23]. As a result, despite the employment of pre-operative methods and intraoperative techniques, 20–60% of patients undergoing BCS require second surgeries due to positive surgical margins[24–32].
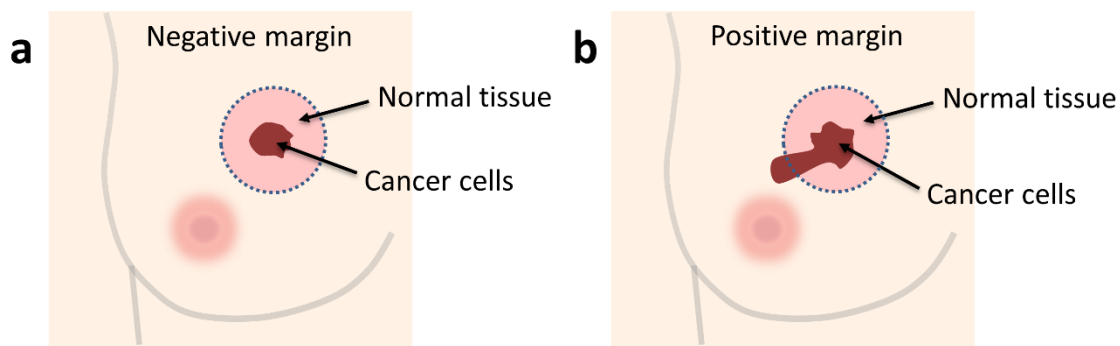
Figure 2.1 Illustrations of negative and positive margins. The circles (blue dashed lines) outline the region of excised breast tissue. (a) In the negative margin, all the cancer cells are encapsulated by normal tissue. (b) In the positive margin, cancer cells are present at the margin of the excised cancer. There are potentially residual cancer cells left in a patient.

The standard of care for surgical margin assessment is post-operative examination of histopathology sections for cancer cells. Intraoperatively, histological examination of tissue can be performed by frozen sectioning, which is limited by the difficulties of freezing adipose-rich tissue, typical of breast specimens, and the amount of time required to analyze large surface areas of tissue. For these reasons, frozen section histology has not been widely incorporated into surgical practice for margin assessment during BCS. The ideal tool for margin assessment would have the

same accuracy as histological analysis without the need for processing specimens. To achieve this goal, we have developed and refined label-free photoacoustic (PA) tomography (PAT) for breast specimens. PAT requires minimal tissue handling, thus shortening specimen preparation and diagnosis. Label-free PA imaging with cellular resolution of surgical specimens could potentially provide fast and accurate breast tumor margin analysis at the time of the initial procedure, which would provide immediate feedback to surgeons for intraoperative decision-making.

PAT is a rapidly growing imaging modality that can provide volumetric images of biological tissue with scalable spatial resolutions and imaging depths[33,34]. PAT can be categorized into two primary imaging modes: photoacoustic microscopy (PAM) and photoacoustic computed tomography (PACT). In optical-resolution PAM mode, the imaging resolution is limited by the diffraction of light and the imaging depth is governed by ballistic photons. Unlike other fluorescence- or scattering-based optical imaging modalities, PAT is based on optical absorption contrast, which, with appropriate wavelength illumination, is highly specific for a variety of targets[33,34]. Using multi-wavelength illumination, different cellular and biological components can be imaged, such as cell nuclei[35], cytochromes[36], blood[37], melanin pigment[38], and lipid[39], all without the need for an exogenous contrast agent. Ultraviolet (UV) laser illumination has the advantage of highlighting cell nuclei, thus providing the same contrast as hematoxylin labeling used in conventional histology and measuring features related to the histological landscape without the need for labels[35]. Hence, together with an acoustically defined axial resolution, UV-PAM can provide multi-layered histology-like imaging of the surface of breast tissue without physical sectioning, which is not achievable by bright-field optical imaging. In this study, we developed and optimized a UV-PAM system to enable label-free, high-resolution, and specific imaging of fixed, unprocessed breast tissue.

6

2.2   Materials and Methods

2.2.1 Human Breast Tissue *Ex Vivo* Imaging Experiments

After informed consent was obtained, breast cancer specimens were collected from women with newly diagnosed stage I/II breast cancer undergoing BCS. The protocol was approved by the Institutional Review Board at Washington University in St. Louis. After excision, breast tumor specimens were placed in formalin and sectioned through the tumor under the supervision of a pathologist (D. V. N.). One half of the specimen was used for histological analysis, and the other half was used for PAM imaging.

2.2.2 Transmission-mode UV-PAM System

Our transmission-mode UV-PAM system (**Fig. 2.2**) employs light at 266 nm, emitted by a Nd:YLF Q-switched UV laser (QL266-010-O, CrystaLaser, Inc.). The laser beam is expanded 50 times by a pair of lenses (LA4647-UV and LA4663-UV, Thorlabs, Inc.) and spatially filtered by a 25-μm–diameter pinhole (#59-255, Edmund Optics, Inc.). The beam is subsequently focused by an aspherical lens (A25-25FPX-S-X, Asphericon, GmbH) to illuminate the specimen from below. The specimen is sandwiched between a lab-made water tank with a membrane, which is placed on the sample holder, and a quartz slide/cover slip. Water fills the gap between the membrane and the specimen to ensure effective acoustic coupling. The PA waves are generated at the bottom surface of the specimen. Finally, the upward propagating PA waves are focused by a lab-made acoustic lens and detected by a water-immersed ultrasonic transducer (V214-BB-RM, Olympus NDT, Inc.) with a central frequency of 50 MHz. The working distance of the ultrasonic transducer is ~6 mm.
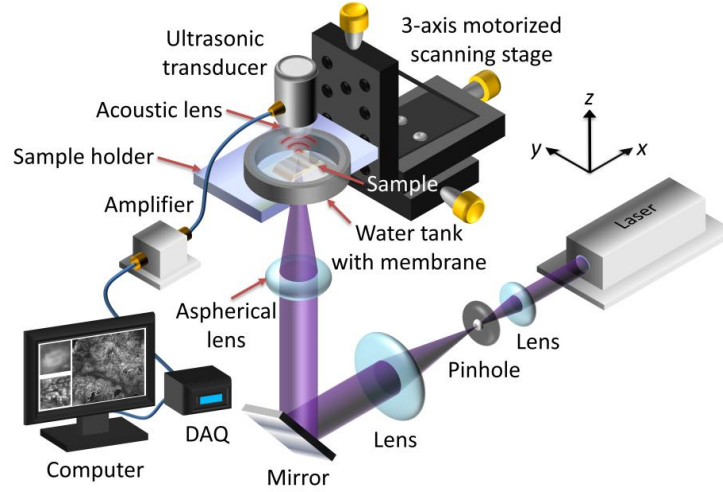
Figure 2.2 Schematic of the UV-PAM system for surgical margin imaging. The UV laser beam is first spatially filtered and expanded by a pair of lenses and a pinhole. The beam is then focused through an aspherical lens onto the bottom of the breast tissue specimen (sample), which is placed inside a water tank on top of a sample holder. Some generated acoustic waves propagate through the tissue and reach a focused ultrasonic transducer. The received acoustic pressure is transduced into an electric signal, which is then amplified and recorded by a data acquisition (DAQ) card. During data acquisition, a maximum amplitude projection (MAP) image from the measured B-scan data is displayed on a computer screen within approximately one second. By raster scanning the sample holder, a MAP image from the C-scan data is also displayed.

2.2.3 Lateral and Axial Resolution Measurements by Gold Nanoparticles

The lateral and axial resolutions of the UV-PAM system were measured by imaging 50-nm–diameter gold nanoparticles (**Fig. 2.3a**). Five gold nanoparticles were segmented and averaged to provide data points for Gaussian profile fitting to measure the lateral resolution. The full width at half maximum (FWHM) of the Gaussian fit profile is ~330 nm (**Fig. 2.3b**), which is close to the theoretical value of ~280 nm for the 0.48 NA of the aspherical lens. For measuring the axial resolution, the A-line signal of the gold nanoparticle's center position was used (**Fig. 2.3a**). The FWHM of the amplitude of the Hilbert-transformed A-line signal reveals the axial resolution of the imaging system. It measures ~32.5 ns (**Fig. 2.3c**), which corresponds to ~48 μm for a speed of sound of ~1480 m/s. The theoretical value is calculated to be ~42 μm, similar to the experimental value.

8
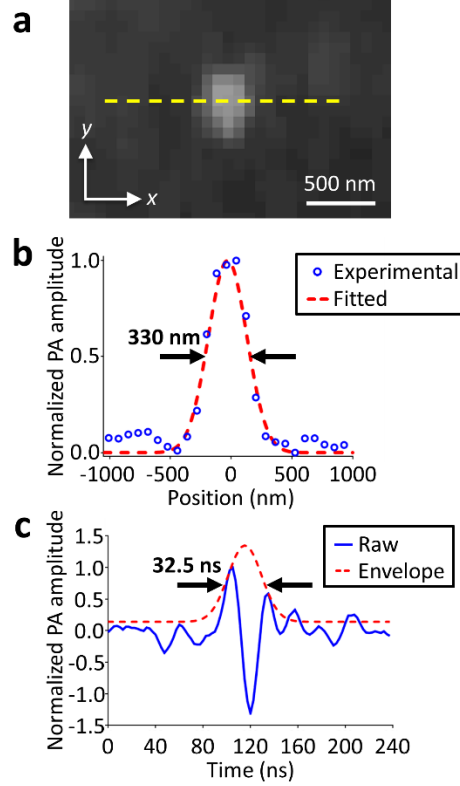
Figure 2.3 Experimentally measured spatial and axial resolutions of the UV-PAM system. (a) UV-PAM image of a gold nanoparticle 50 nm in diameter. The profile along the yellow dashed line is extracted for averaging. (b) Averaged line profile of five gold nanoparticles (blue circles). With Gaussian fitting (red dashed line), the lateral resolution is estimated to be 330 nm. (c) A-line signal (blue solid line) of the center position of the gold nanoparticle shown in (a). The axial resolution was determined by analyzing the FWHM of the amplitude of the Hilbert-transformed A-line signal (red dashed line). The axial resolution is estimated to be 32.5 ns, which corresponds to 48 µm.

2.2.4 UV-PAM of Fixed, Paraffin-embedded Breast Tumor Specimen Versus Conventional Microscopy of Specimen Processed with Standard Histology

The procedure for preparing thin breast tissue slices without and with H&E staining is shown in **Fig. 2.4**. For UV-PAM imaging, a quartz slide, which is a UV transparent material, was used instead of a glass slide below the sectioned breast tumor. This material ensured effective light delivery to the breast tissue. The quartz slide was put on the sample holder, and the tissue was covered by a water tank with a membrane window. Note that no cover slip was used and water was added between the tissue-to-membrane interfaces to ensure effective acoustic coupling. Lastly,

9

the water tank was filled with water and the focused ultrasonic transducer was immersed for acoustic wave detection. After PA imaging, the tissue slice was sent back to the pathologist for H&E staining and corresponding histologic imaging.
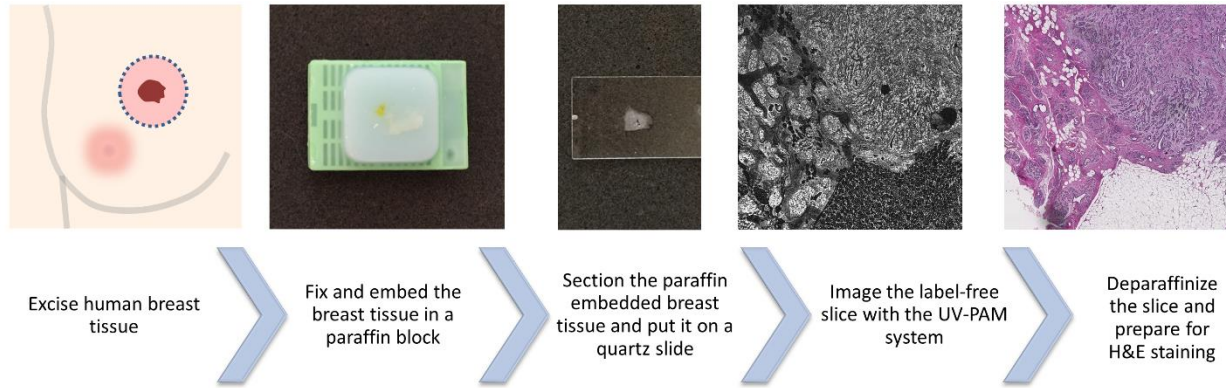
Figure 2.4 Procedure for obtaining thin breast tissue slices without and with H&E staining. A breast tumor was first excised by our surgeon, then fixed and embedded in a paraffin block. After that, the paraffin block was sectioned and put on a quartz slide, which was then imaged by our UV-PAM system. Afterwards, the tissue slice was deparaffinized and H&E stained to obtain a corresponding histology image.

2.2.5 UV-PAM of Fixed, Unprocessed Breast Tumor Specimens Versus Conventional Microscopy of Specimens Processed with Standard Histology

Preparation of all breast tumor specimens followed the same protocol. The specimens were promptly delivered from the pathologist to the PA imaging lab. During delivery, the specimen was immersed in 10% neutral buffered formalin (NBF) to maintain its rigidity and shape. Upon arrival, the breast tumor was put on a quartz cover slip, which served as both a flat platform for the rough breast tissue surface and as a transparent optical window for UV light illumination. When the specimen was further sandwiched by the water tank membrane, the breast tissue, which is ragged at the edges, was stretched over the quartz cover slip surface. This imaging platform design enabled wide-FOV in-focus imaging. As before, the water tank was put on the sample holder and filled with water for acoustic coupling. The acoustic waves generated were detected by the immersed

10

ultrasonic transducer. After PA imaging, the thick breast tissue was put back into the NBF and returned to the pathologist. The breast tissue then underwent standard histology procedures for H&E staining. To make full FOV comparison with UV-PAM images, the H&E-stained slide was imaged with bright-field microscopy (Nanozoomer, Hamamatsu Photonics K.K.).

2.2.6 Data Acquisition and Processing

We developed a LabVIEW® software based data acquisition program. After acquiring all the user inputs, the computer transfers all the parameters to a central controller (sbRIO-9623, National Instruments, Corp.), which integrates with a reconfigurable field-programmable gate array. The controller triggers the UV laser and the data acquisition card (ATS9350, Alazar Technologies, Inc.) installed in the computer, and data are recorded on the computer hard disk, with real time display on the computer screen. The controller also triggers the x and y scanning stages (PLS-85, PI miCos, GmbH) in synchronization with the laser, for point-by-point scanning of the specimen surface. Each laser pulse generates a 1D PA image (A-line) by recording the time course of the PA signal. Volumetric image of the specific optical absorption (J/m^3) of the specimen can be obtained by raster scanning a motorized stage.

2.2.7 Calculations of the Cell Nuclear Cross-sectional Area and Internuclear Distance

Since cell nuclei have higher optical absorption than other tissue components at the illumination wavelength, they generated stronger PA signals. To distinguish cell nuclei from background, we set a contrast-to-noise ratio threshold of 6 dB, where noise was defined as the standard deviation of the background area's amplitude. Based on the threshold, the PA image was then converted into a binary image. The cell nuclei were identified (i.e., segmented) based on the binary PA image. As

the lateral resolution of UV-PAM (0.33 µm) was much finer than the axial resolution (48 µm), the

cell nuclear cross section area was calculated in the lateral plane. After the cell nuclei were

identified, the center positions of the cell nuclei were located and used to compute the shortest

adjacent distance to a neighboring cell nucleus to represent the internuclear distance.

2.3   Results

2.3.1 UV-PAM System for Unprocessed Human Breast Cancer Imaging

Our UV-PAM system (**Fig. 2.2**), which can handle specimens of various thicknesses, produces

images by detecting acoustic waves generated by laser-induced rapid thermoelastic expansion[33,34].

A focused ultrasonic transducer detects the one-dimensional (1D) depth-resolved PA signals (A-

lines). Cross-sectional images (B-scans) or volumetric images (C-scans) can be produced

respectively by linear or raster scanning using a motorized scanning stage. The UV-PAM system

records and displays the PA B-scan images in real time during data acquisition. Because different

absorbers intrinsically possess different optical absorption spectra, when one absorber dominates

at a chosen wavelength, a single-wavelength laser can be used to probe a specific biological

component without resorting to exogenous labels. In cancer histology, the size variation and

packing densities of cell nuclei can be used to identify cancer cell clusters[40]. Therefore, UV light

(266 nm), which DNA and RNA in cell nuclei absorb by an order of magnitude more strongly than

other biological components[35], is used for illumination in our UV-PAM system. At this short

wavelength, high spatial resolution can be achieved. The lateral imaging resolution was

experimentally measured to be ~330 nm (**Fig. 2.3b**), comparable to that of a conventional bright-

field optical microscope with a high numerical aperture (NA) and sufficient to identify individual

cell nuclei. Therefore, UV-PAM images should be able to reveal individual cell nuclear information without labeling.

2.3.2 Imaging of a Section of Breast Tumor Specimen without and with Hematoxylin and Eosin Staining

To initially validate the performance of UV-PAM for breast tissue imaging, we imaged a section of tissue cut from a formalin-fixed paraffin-embedded block of breast tissue that had not been stained with hematoxylin and eosin (H&E) (**Fig. 2.4**). We raster scanned a thin slice over a 5.0 x 5.0 mm^2 area along the *x* and *y* axes for ~100 min. Note that in PAM, raster scanning generally produces a volumetric image. However, since the section slice was only 5 μm thick, finer than our axial resolution (**Fig. 2.3c**), only two dimensional (2D) images are presented (**Fig. 2.5**). As a result of the intrinsic optical absorption, cell nuclei appear to be the brightest in UV-PAM images. After PA imaging, the slice was deparaffinized, H&E stained, and imaged with optical microscopy. Comparison of the cell architecture between the UV-PAM image (**Fig. 2.5a**) and the H&E-stained image (**Fig. 2.5b**) reveals multiple similarities. Well-defined borders between normal tissue and tumor, which is mostly invasive ductal carcinoma, are outlined with green dashed lines in the images (**Fig. 2.5**, **a** and **b**). The normal region (red dashed region, **Fig. 2.5c**) in the UV-PAM image (**Fig. 2.5a**) has a correlation coefficient of 0.74 with its corresponding position in the H&E-stained image (**Fig. 2.5d**). We overlaid the magnified H&E-stained image on its respective UV-PAM image to show their similarity (**Fig. 2.5e**). Similarly, the tumor region (yellow dashed region, **Fig. 2.5f**) in the UV-PAM images has a correlation coefficient of 0.64 with its H&E-stained image (**Fig. 2.5g**). The overlaid image is shown in **Fig. 2.5h**. The areas with imperfect spatial overlap were mainly due to structures that had been locally deformed during the subsequent sample preparation after PA imaging, which can be easily seen by comparing the features on the top right-hand corners

of **Fig. 2.5** (**c** and **d**), marked with blue dashed lines and arrows. We emphasize that although the correlation coefficients were diminished by local deformation, corresponding fundamental characteristics of the tissue structures are present in both UV-PAM and H&E-stained images. (i) Purple, (ii) pink and red, and (iii) white in the H&E-stained images correspond to (i) the brightest, (ii) moderately bright, and (iii) dark features in the gray-scale UV-PAM images. This color
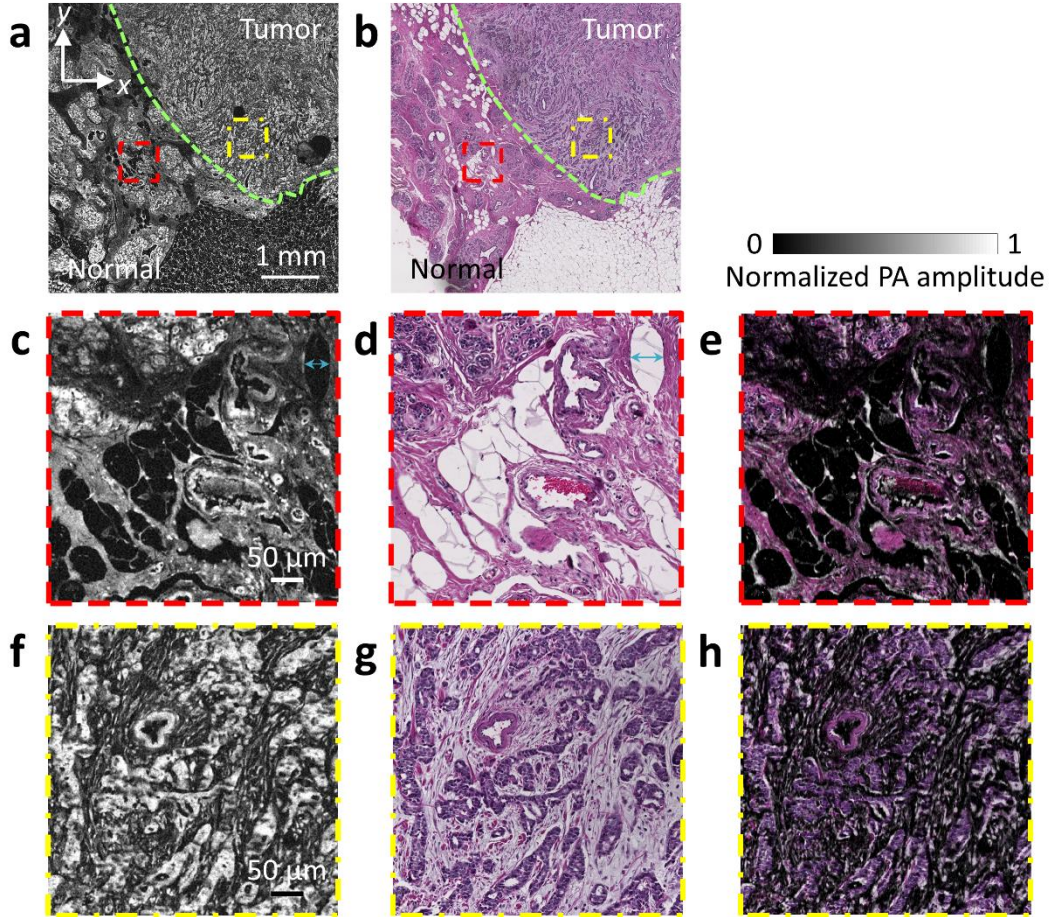
Figure 2.5 Imaging of thin breast tissue slices without and with H&E staining. (a) Unstained paraffin-embedded breast tissue slice imaged by the UV-PAM system. (b) H&E-stained deparaffinized breast tissue slice imaged by a standard microscope. The green dashed lines in (a) and (b) outline the boundaries of the normal and tumor regions. The upper right area is the tumor region, and the bottom left area is the normal region. (c and d) Zoomed-in UV-PAM and H&E-stained images of the normal regions (red dashed regions) in (a) and (b), respectively. The blue dashed lines and arrows on the top right-hand corners in (c) and (d) label a representative local deformation. (e) Overlay image of (d) on (c). (f and g) Zoomed-in UV-PAM and H&E-stained images of the tumor regions (yellow dashed regions) in (a) and (b), respectively. (h) Overlay image of (g) on (f).

correspondence agrees well with the optical absorption-based contrast expectation. Purple labels the cell nuclei, which intrinsically absorb UV light most strongly. Pink and red indicate cytoplasm, connective tissue, and other extracellular substances, which absorb UV light less strongly. White represents adipocytes, which appear as a void due to loss of lipid during tissue processing, and appear dark in UV-PAM images because no absorbers were present to produce acoustic signals.

2.3.3 Label-free UV-PAM of Fixed, Unprocessed Human Breast Tumors Versus Traditional Microscopy of Specimens Processed with Standard Histology

To show the full potential of UV-PAM, we imaged formalin-fixed but unprocessed human breast tumors (**Figs. 2.6**, **2.7**, and **2.8**). After surgical excision, the breast tumors were fixed in formalin to prevent tissue degradation. Small samples were taken from the tumor/normal interface and sent for PA imaging. We emphasize that prior to PA imaging, the breast tumors were only fixed, and did not undergo any further processing. Subsequently the specimens were processed according to standard tissue preparation protocols (i.e., paraffin embedding, sectioning, and H&E staining). Sections corresponding to the UV-PAM images were analyzed by conventional bright-field optical microscopy. Since the UV-PAM system images the surface and subsurface of a specimen (**Fig. 2.9**), to prepare the best corresponding H&E-stained images, superficial sections were utilized. These H&E-stained sections did not exactly replicate the surface imaged by UV-PAM, but the image features are still remarkably similar.
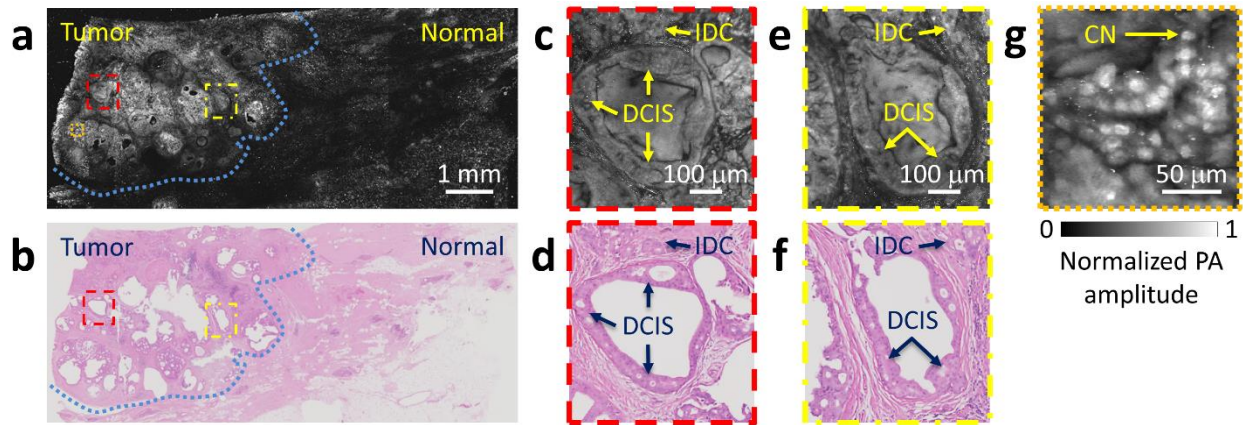
Figure 2.6 Imaging of a breast tumor from the first patient. (a) UV-PAM image of the fixed, unprocessed breast tumor. (b) H&E-stained histologic image of the same area shown in (a) acquired after processing, sectioning, and staining the excised breast tissue. The blue dashed lines in (a) and (b) outline the interface between the normal and tumor regions. (c and d) Zoomed-in UV-PAM and H&E-stained images of the red dashed regions in (a) and (b), respectively. (e and f) Zoomed-in UV-PAM and H&E images of the yellow dashed regions in (a) and (b), respectively. IDC, invasive ductal carcinoma; DCIS, ductal carcinoma *in situ*. (g) Zoomed-in UV-PAM image of the orange dashed region in (a). CN, cell nuclei.
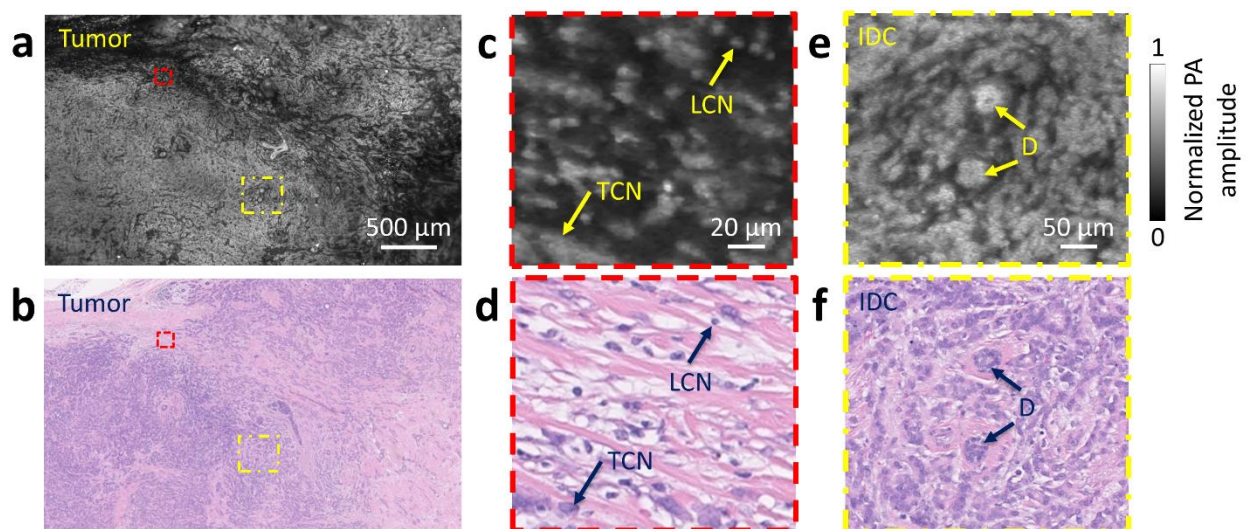
Figure 2.7 Imaging of a breast tumor from the second patient. (a) UV-PAM image of the fixed, unprocessed breast tumor. (b) H&E-stained histologic image of the same area shown in (a) acquired after processing, sectioning, and staining the excised breast tissue. (c and d) Zoomed-in UV-PAM and H&E images of the red dashed regions in (a) and (b), respectively. LCN, lymphocyte cell nucleus; TCN, tumor cell nucleus. (e and f) Zoomed-in UV-PAM and H&E-stained images of the yellow dashed regions in (a) and (b), respectively. IDC, invasive ductal carcinoma; D, duct. The two ducts are surrounded by invasive ductal carcinoma.

16
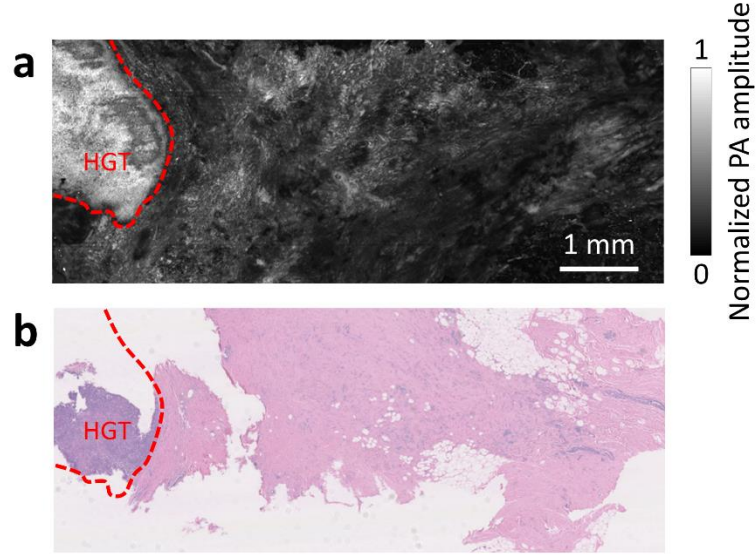
Figure 2.8 Imaging of a breast tumor from the third patient. (a) UV-PAM image of the fixed, unprocessed breast tumor. (b) H&E-stained histologic image of the same area shown in (a) acquired after processing, sectioning, and staining the excised breast tissue. The red dashed lines in (a) and (b) outline the boundaries of the high grade tumor (HGT).
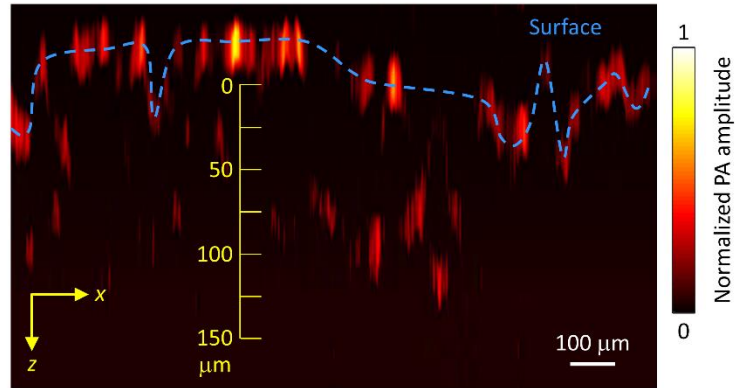
Figure 2.9 Representative *xz* **projected human breast tumor image acquired over 10.0 x 4.2 mm² from the first patient specimen.** The blue dashed line outlines the surface of the breast tissue. With UV light illumination, the deepest cellular structures are ~100 μm in depth measured from the tissue surface.

For the fixed, unprocessed breast tumor specimen from the first patient, the region of interest (ROI) was 10.0 x 4.2 mm² (**Fig. 2.10a**). **Fig. 2.6a** shows a UV-PAM image of the ROI. The scanning time was ~180 min. The specimen was put in a lab-made sample holder, which flattened the tissue for wide field-of-view (FOV) in-focus imaging. A section was re-imaged to

show the image's reproducibility (**Fig. 2.11**). **Fig. 2.12** shows three snapshots of a series of close-up UV-PAM images of a row of the ROI. Fundamental characteristics of the cancer structures (**Fig. 2.12a**), tumor margin (**Fig. 2.12b**), and normal tissue (**Fig. 2.12c**) can all be identified respectively in the close-up scanning UV-PAM images. **Fig. 2.13a** shows a series of depth-resolved UV-PAM images of a portion of the ROI. Two close-up depth-resolved UV-PAM images (**Fig. 2.13b** and **c**) of the cancer regions are also simultaneously shown to illustrate the strength of the multi-layered imaging capability provided by UV-PAM over conventional histology. After PA imaging, the corresponding sections were prepared histologically and images were acquired (**Fig. 2.6b**). The close-up UV-PAM images (**Fig. 2.6**, **c** and **e**) reveal features similar to their corresponding H&E-stained images (**Fig. 2.6**, **d** and **f**). Each image centers on expanded breast ducts with a cribriform pattern of cellular proliferation, characteristic of ductal carcinoma *in situ*, that can be readily discerned in both the UV-PAM and H&E-stained images. Smaller nests of densely packed nuclei, representing invasive ductal carcinoma, can also be seen along the top edge in **Fig. 2.6** (**c** to **f**). From another close-up UV-PAM image (**Fig. 2.6g**), it is clear that our imaging system is capable of imaging individual cell nuclei.
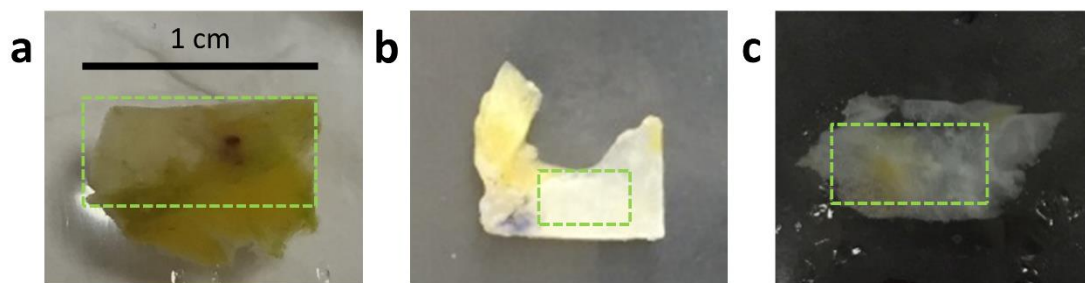
Figure 2.10 Photographs of the breast tissue specimens. (a) First patient's specimen with a thickness of ~2 mm. (b) Second patient's specimen with a thickness of ~3 mm. (c) Third patient's specimen with a thickness of ~1 mm. The green dashed regions are the imaging FOV for both UV-PAM and standard histology.

For the second patient, a ROI of 7.5 x 4.5 mm^2 (**Fig. 2.10b**) was imaged by our UV-PAM system (**Fig. 2.7a**). The corresponding H&E-stained image is shown in **Fig. 2.7b**. The close-up

UV-PAM image (**Fig. 2.7c**) shows a number of small bright cell nuclei that correspond to lymphocytes on the histology image (**Fig. 2.7d**). Lymphocytes are often associated with cancer. Comparing the two close-up images (**Fig. 2.7**, **c** and **d**), we observe denser lymphocytes in our UV-PAM image. This difference can be explained by the greater imaging penetration depth of UV-PAM (**Fig. 2.9**) in comparison to the sectioned slice thickness of the H&E-stained tissue.
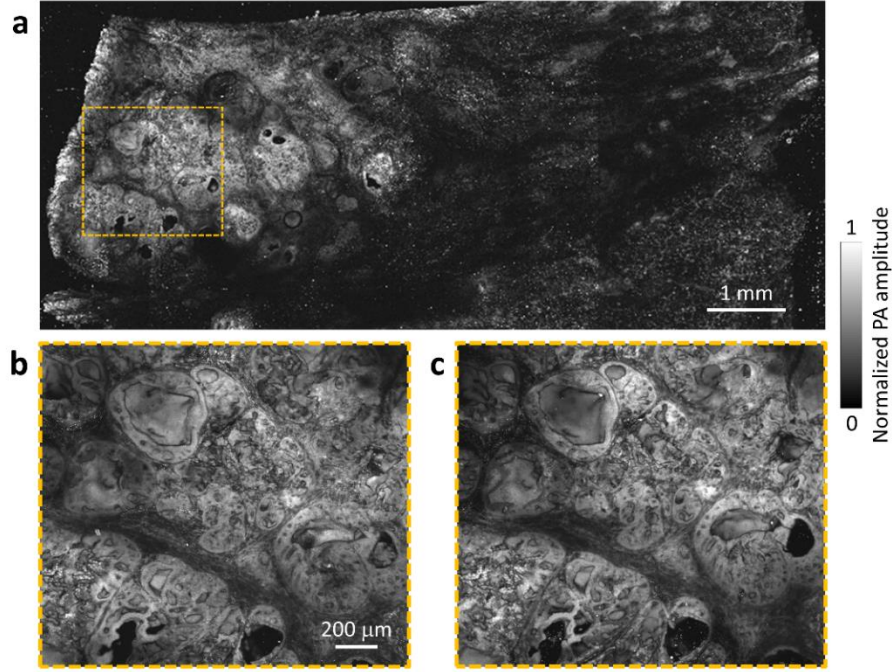
Figure 2.11 Reproducibility of the UV-PAM system for breast tumor tissue imaging. (a) UV-PAM image of the first patient's specimen, which is shown in Fig. 2.6a. (b) First re-imaging of the zoomed-in portion in (a) (orange dashed region). (c) Second re-imaging of the same zoomed-in area. Note that between images (b) and (c), the specimen was removed from the water tank and sample holder, and then put back in.
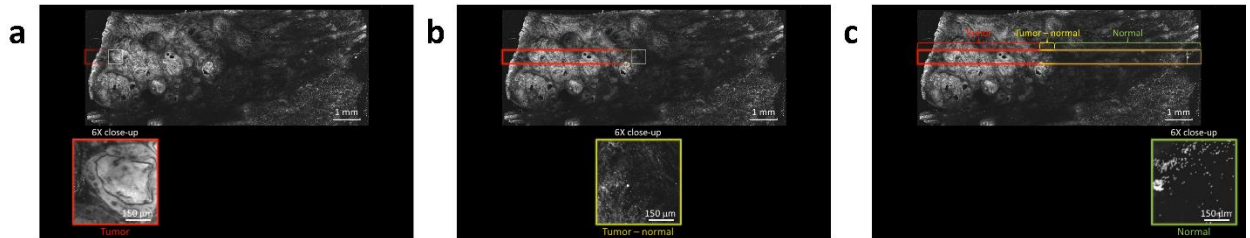
Figure 2.12 Three snapshots of a series of close-up UV-PAM images of a row of the ROI. Fundamental characteristics of the cancer structures (a), tumor margin (b), and normal tissue (c) can all be identified respectively in the close-up scanning UV-PAM images. Red, tumor; Yellow, margin; Green, normal.
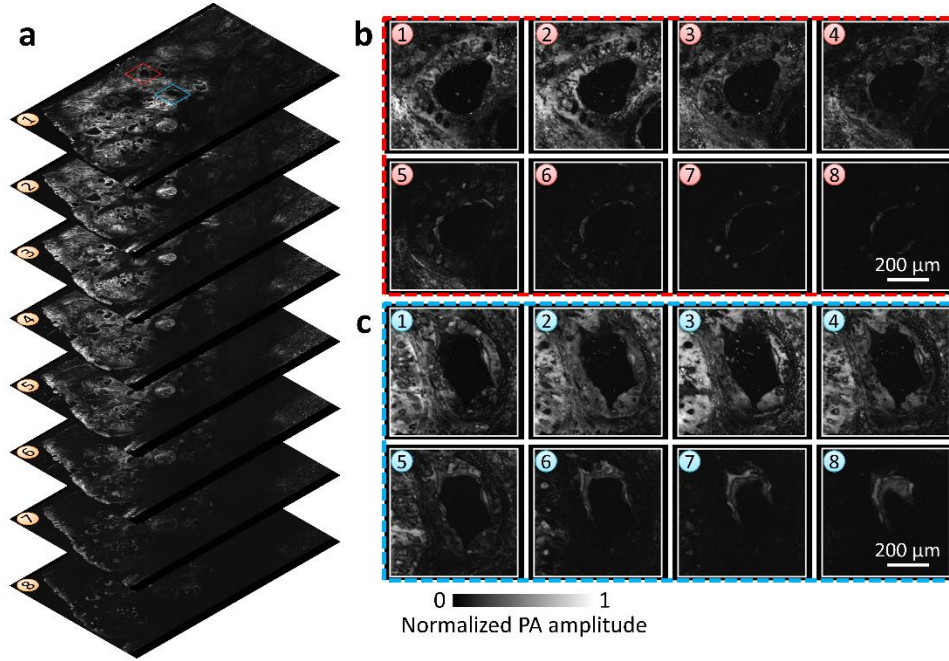
Figure 2.13 Series of depth-resolved images of the first patient's breast tumor specimen imaged by UV-PAM. (a) UV-PAM images of the entire FOV. (b and c) Close-up UV-PAM images of the respective regions marked (red and blue) in (a). All depth-resolved images are shown at 8 depths with an axial step size of 22 µm.

When the cell nuclei are densely packed along the lateral and axial directions, individual cell nuclei cannot be resolved, resulting in a bright and dense feature, as seen in another close-up UV-PAM image (**Fig. 2.7e**). In this case, the corresponding H&E-stained image (**Fig. 2.7f**) demonstrates densely packed breast tumor cells. For a third patient sample, the ROI was 7.8 x 3.0 mm^2 (**Fig. 2.10c**). As with the second patient, in our UV-PAM image we can see a bright signal in the left region (**Fig. 2.8a**). This region also represents a high-grade tumor, as shown in the corresponding H&E-stained image (**Fig. 2.8b**). This H&E-stained image reveals relatively large empty regions, which are fully filled in the UV-PAM image, due to the rough surface of the third specimen. Therefore, these UV-PAM and H&E-stained images (**Fig. 2.8**, **a** and **b**) clearly show that the greater imaging depth allows the UV-PAM system to provide more cellular structural information than a corresponding H&E-stained thin section of the same tissue.

20
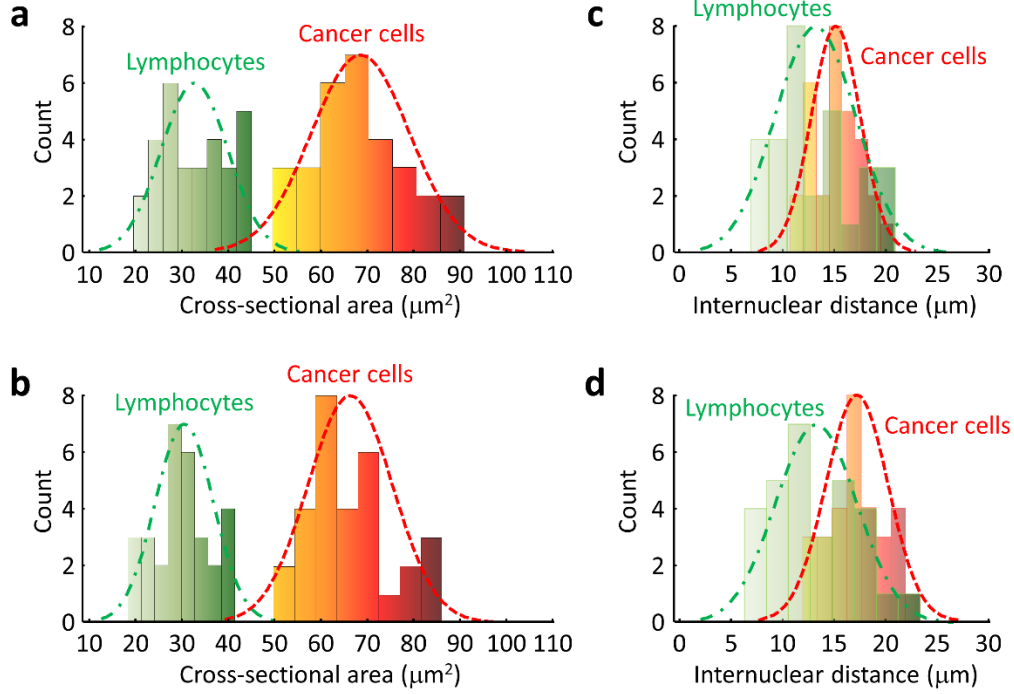
Figure 2.14 Distributions of cell nuclear area values and internuclear distances in the breast tumor specimens (Figs. 2.6 and 2.7), where bin interval = 8 and *n* = 30 for each distribution. (a) Histogram of the cell nuclear cross-sectional areas imaged by UV-PAM (Figs. 2.6c and 2.7c). The green dashed line is a Gaussian fit for lymphocytes, with a mean of 32.8 μm^2 and an SD of 7.0 μm^2. The red dashed line is a Gaussian fit for cancer cells, with a mean of 67.6 μm^2 and an SD of 11.0 μm^2. (b) Histogram of the cell nuclei cross-sectional areas imaged by histology (Figs. 2.6d and 2.7d). The green dashed line is a Gaussian fit for lymphocytes, with a mean of 30.1 μm^2 and a SD of 6.7 μm^2. The red dashed line is a Gaussian fit for cancer cells, with a mean of 66.0 μm^2 and a SD of 9.2 μm^2. (c) Histogram of the internuclear distances imaged by UV-PAM (Figs. 2.6c and 2.7c). The green dashed line is a Gaussian fit for lymphocytes, with a mean of 13.1 μm and an SD of 3.8 μm. The red dashed line is a Gaussian fit for cancer cells, with a mean of 15.4 μm and an SD of 2.4 μm. (d) Histogram of the internuclear distances imaged by histology (Figs. 2.6d and 2.7d). The green dashed line is a Gaussian fit for lymphocytes, with a mean of 13.2 μm and an SD of 4.1 μm. The red dashed line is a Gaussian fit for cancer cells, with a mean of 17.2 μm and an SD of 2.9 μm.

To show that diagnostic features can be computed quantitatively from our UV-PAM images, the sizes and the internuclear distances of the cell nuclei from various cell types were measured in both UV-PAM and H&E-stained images. In particular, nuclear features from breast cancer cells were derived from **Fig. 2.6** (**c** and **d**), while lymphocyte nuclear features were derived from **Fig. 2.7** (**c** and **d**). Our results show that the calculated distribution of the nuclear area per cell values from UV-PAM images is similar to that from H&E-stained images (**Fig. 2.14**, **a** and **b**)

21

in terms of mean values and standard deviations (SD). Based-on the nuclear cross-sectional area, breast cancer cells and lymphocytes can be readily distinguished (**Fig. 2.14**, **a** and **b**). Our results also show that the calculated distributions of the internuclear distances of breast cancer cells and lymphocytes from the UV-PAM images are similar to those from the H&E-stained images (**Fig. 2.14**, **c** and **d**) with good agreement in mean and SD values. These results further support the accuracy of the information that can be extracted from UV-PAM images, which would potentially enable accurate PAM-based histological assessment of cancer specimens.

2.4 Conclusions and Discussions

Implementation of an intraoperative UV-PAM system for breast tumor excision could be transformative. Our UV-PAM system was able to image fixed, unprocessed breast tumors with an image quality comparable to that of conventional histology using processed, paraffin embedded, sectioned, and H&E-stained specimens (**Figs. 2.6**, **2.7**, and **2.8**). While fixed breast tumors were imaged in this study to maintain tissue integrity during relatively long intervals between surgery and processing for histology, fresh breast tumors are expected to provide similar imaging contrast[41]. With relevant information regarding such tissue features as the average nuclear size and internuclear distance (**Fig. 2.14**), typically obtained from histology, UV-PAM images could be used to detect cancer cell clusters at the margins of tissue specimens during a surgical procedure, allowing immediate action to achieve clear margins. Although benign breast epithelial cells are too few in the UV-PAM images to be compared with cancer cells, the close correspondence between UV-PAM and histology for both lymphocytes and cancer cells provides the proof-of-concept that UV-PAM can be utilized to examine diagnostically relevant parameters.

To fulfill clinical needs of intraoperative assessment, the imaging throughput has to be improved. Currently, acquiring a ~1.0 x 1.0 cm^2 image with spatial resolution comparable to that of a traditional high-NA optical microscope takes ~7 hours. However, multichannel parallel imaging can shorten the scanning time by orders of magnitude. For instance, the laser beam can be focused to more than 80X80 spots by a micro-lens array while the generated PA waves are received by an ultrasonic transducer array simultaneously[42]. For intra-operative margin analysis of surgical specimens, it would be ideal to scan the entire surface of a specimen although the current gold standard histology is to spot check only selected regions due to limited throughput. As a typical breast lumpectomy specimen has a diameter less than 5.0 cm with a thickness of ~1.0 cm, the total surface area is less than ~55.0 cm^2, which could be imaged within 4 min. With this imaging duration combined with computer-aided detection[43], feedback could be provided to surgeons intraoperatively.

The functionality of the UV-PAM system can be boosted in two ways. First, instead of imaging excised, fixed, and unprocessed breast tissue using a bench-top UV-PAM system, it is possible to design the UV-PAM system in a handheld probe configuration that allows *in vivo* imaging of breast tissue. With a high-repetition-rate laser, real-time UV-PAM images can be provided with an imaging FOV of ~3.0 x 3.0 mm^2. This capability would enable "virtual" histology-guided BCS, which would allow surgeons to see histology-like images of remaining breast tissue after tumor excision and allow immediate detection and removal of residual tumor. UV light *in vivo* can be safely used at the targeted imaging depth of ~100 μm since the corresponding surface's laser exposure is <0.1 mJ/cm^2 for the current UV-PAM images, and thus well within the American National Standards Institute safety standard, which sets the maximum permissible exposure at 3 mJ/cm^2 for this wavelength[41]. Second, the imaging specificity of the

23

UV-PAM system can be improved by using a multi-wavelength technique. Although UV illumination can probe cell nuclei, other breast tissue structures, such as stroma and microcalcification, absorb UV light at lower, but still similar levels, and appear moderately bright with comparable signal amplitudes in the UV-PAM images. With hydroxyapatite absorption contrast, employing a 700 nm laser would allow the identification of microcalcifications[44], which are associated with some breast cancers[45,46].

One limitation of the UV-PAM imaging performed here is that densely packed cell nuclei create a bright signal (**Fig. 2.7**, **a**, **b**, **e** and **f** and **Fig. 2.8**, **a** and **b**), preventing the observation of individual cell nuclei. This effect is likely due to the difference in imaged thicknesses (~100 μm in UV-PAM versus ~5 μm in H&E). The intense signal could lead to false positive margin calls when dense lymphocytes rather than tumor cells generate this pattern. Equipping the UV-PAM system with optical sectioning capability, which can be achieved by several different approaches, such as Grüneisen relaxation[47], would improve the axial resolution. With optical sectioning, UV-PAM could image a thickness of breast tissue equivalent to standard histological sections, likely eliminating this confounding imaging pattern. Furthermore, with improved axial resolution, it is possible to reconstruct a detailed volumetric image of breast tumor specimens with more resolvable points along the axial direction, enabling three-dimensional information extraction. This previously inaccessible information could potentially boost the accuracy of specimen analysis.

In summary, we have developed and optimized UV-PAM of breast tissues, generating images of cellular structures and organizations similar to that seen on histological sections stained with H&E. Diagnostic features, such as the sizes and internuclear distances of cell nuclei, can be computed accurately from our UV-PAM images. These features have been found to relate to

cytologic and histologic grade, tumor size, nodal status, and clinical stage[48] (40). With these useful parameters, automatic algorithms could be developed to recognize malignancy in UV-PAM images. We believe that this is the first step towards the development of an intraoperative margin assessment tool that can be used by surgeons and pathologists to detect and distinguish cancer cells and normal cells at surgical margins. While we have concentrated on breast tissue, we believe that UV-PAM can be optimized for other cancer specimens where margin status is critical for patient outcome, such as pancreatic cancer and glioblastoma.

Chapter 3 Label-free Automated Three-dimensional Imaging of Whole Organs by Microtomy-assisted Photoacoustic Microscopy

Three-dimensional (3D) optical imaging of whole biological organs with microscopic resolution has remained a challenge. Most versions of such imaging techniques require special preparation of the tissue specimen. In this chapter, we demonstrate microtomy-assisted photoacoustic microscopy (mPAM) of mouse brains and other organs, which automatically acquires serial distortion-free and registration-free images with endogenous absorption contrasts. Without tissue staining or clearing, mPAM generates micrometer-resolution 3D images of paraffin- or agarose-embedded whole organs with high fidelity, achieved by label-free simultaneous sensing of DNA/RNA, hemoglobins, and lipids. mPAM provides histology-like imaging of cell nuclei, blood vessels, axons, and other anatomical structures, enabling the application of histopathological interpretation at the organelle level to analyze a whole organ. Its deep tissue imaging capability leads to less sectioning, resulting in negligible sectioning artifact. mPAM offers a new way to better understand complex biological organs. The work in this chapter has been published in *Nature Communications*[49].

3.1 Background

In biomedical imaging, all optical techniques face a fundamental trade-off between spatial resolution and tissue penetration; hence, obtaining an organelle-level resolution image of a whole organ has remained a challenging and yet appealing scientific pursuit. Over the past decade, optical microscopy assisted by mechanical sectioning or chemical clearing of tissue has been demonstrated as a powerful technique to overcome this dilemma, one of particular use in imaging the neural network[50–55]. Thanks to recent advances in computing power, the acquired data, typically terabytes in size, can be automatically processed to visualize the three-dimensional (3D) structure in a whole brain. However, this type of techniques needs lengthy special preparation of the tissue specimen, which hinders broad application in life sciences. For example, diffusion staining of a whole brain[52] is extremely slow due to the scant extracellular space in the central nervous system. Similarly, electrophoretic removal of lipids in the brain[55], resulting in a transparent brain for easy staining and imaging, causes an uncertain loss of biological information. Therefore, finding an imaging method applicable to minimally processed tissue, ideally fresh tissue, can provide new insights into complex biological systems and make whole-organ microscopy a universal laboratory technique.

Among all 3D imaging techniques, histology is an attractive way to analyze specimens because histopathological interpretation can be readily applied from organelle to organ levels. However, ordinary wide-field optical microscopy cannot provide optical sectioning, resulting in blurry images when a thick tissue is imaged. To get high resolution and high contrast histologic images, thick tissue always requires mechanical sectioning before imaging. Therefore, 3D histology can be obtained only by registering images of all thin slices, each subjected to a different level of inaccuracy, despite considerable rectification efforts in the field[56–61]. In addition,

sectioning before imaging can also cause undesired tissue ruptures in each thin slice, further reducing the quality of registered images. So far, sharply imaging the presented surface of tissue before sectioning it remains a challenging and yet appealing goal in histology.

Here, we propose a new label-free 3D imaging technique, named microtomy-assisted photoacoustic microscopy (mPAM), for potentially imaging all biomolecules with 100% endogenous natural staining in whole organs with less sectioning and high fidelity. Photoacoustic (PA) microscopy (PAM)[1,33] is a fast developing label-free imaging method. While in an unstained piece of tissue, most endogenous biomolecules do not fluoresce; however, all of them absorb photons at some wavelengths. Most absorbed light energy will be converted into heat, which results in an acoustic pressure rise propagating as ultrasound—the signal source for PAM. Label-free PAM has been demonstrated in such broad biomedical applications as imaging DNA/RNA[35], cytochromes[36], hemoglobins[37], melanin[38], and lipids[62] at an optical wavelength ranging from ultra-violet (UV) to near-infrared. This list of imaging targets is expanding with the ongoing exploration of endogenous absorption, and label-free imaging of all biomolecules remains possible. Moreover, PAM in reflection mode is applicable to large tissue volumes and does not require preparation of thin tissue sections[50]. Combined with a microtome for serial removal of previously imaged tissue sections, PAM performs well as a tool for imaging biomolecules of interest in an unstained organ at subcellular resolution. Furthermore, PAM's label-free nature enables it to image differently embedded organs for different applications, e.g., paraffin and agarose are the most common embedding materials used in conventional histology and neuroscience[63], respectively. In this paper, we demonstrate the first label-free mPAM, using UV light for histology-like imaging without staining[8], in whole organs (e.g., mouse brains), most of them formalin-fixed and paraffin- or agarose-embedded for minimal morphological deformation. A fresh mouse kidney embedded

28

in agarose is also imaged. In addition, mPAM with dual wavelength illuminations is also employed to image a mouse brain slice, demonstrating the potential for label-free imaging of multiple biomolecules. With visible light illumination, mPAM shows its deep tissue imaging capability, which enables less slicing and hence reduces sectioning artifacts.

3.2   Materials and Methods

3.2.1 Organ Preparation

The organs were extracted from Swiss Webster mice (Hsd:ND4, Harlan Laboratories). The brain, one lung, and the kidney were harvested immediately after each mouse was sacrificed. The brain and lung were fixed in 10% neutral-buffered formalin at room temperature for 5 days. Afterwards, the brain and the lung were embedded in paraffin as block specimens, following standard histology procedure, and then sectioned by a microtome into thin slices as required. Four more brains were embedded in 4% agarose as block specimens, and then sectioned by a microtome into thin slices with different sectioning thicknesses. The fresh kidney was sectioned by hand to a ~1 mm thick slice, then embedded in 4% agarose as a block specimen. All experimental animal procedures were carried out in conformity with a laboratory animal protocol approved by the Animal Studies Committee of Washington University in St. Louis.

3.2.2 mPAM System

The user interface of the mPAM system is programmed in LabVIEW. After acquiring all the inputs from the user, the computer transfers all the parameters to a central controller (sbRIO-9623, National Instruments, Corp.) which integrates a real-time processor (400 MHz) and a reconfigurable field-programmable gate array. The controller triggers an Nd:YLF Q-switched UV

laser (QL266-010-O, CrystaLaser, Inc.) to generate laser pulses with a 266 nm wavelength, 7 ns pulse width, ~5 nJ pulse energy on the imaging targets, and 10 kHz pulse repetition rate, or an OPO laser (NT242-SH, Altos Photonics, Inc.) to generate laser pulses with a 420 nm wavelength, 5 ns pulse width, ~200 nJ pulse energy on the imaging targets, and 1 kHz pulse repetition rate. The laser beam is focused onto the organ immersed in water by a custom-made water-immersion UV objective lens (consisting of an aspheric lens, a concave lens, and a convex lens (NT49-696, NT48-674, NT46-313, Edmund Optics, Inc.)); **Fig. 3.1**) with a numerical aperture (NA) of 0.16. The excited photoacoustic waves from the organ are detected by a custom-made ring-shaped ultrasonic transducer (42 MHz center frequency, 76% -6 dB bandwidth), which has a central hole for light delivery. The signals are then amplified, digitized by a data acquisition card (installed on the computer and triggered by the controller; ATS9350, Alazar Technologies, Inc.), recorded on the computer hard disk, and displayed in real time on the computer screen. The controller also triggers the scanning stages (*x* and *z* stages: PLS-85, PI miCos, GmbH; *y* stage: LS-180, PI miCos, GmbH), in synchronization with the laser, for point-by-point imaging of the organ surface. By calculating the amplitude of each A-line photoacoustic signal, we obtain a 2D image of the specific optical absorption (J/m^3) of the organ. After each surface image is acquired, the organ, controlled by the scanning stages, is automatically sectioned by a microtome blade mounted inside the water tank. The sliced-off paraffin-embedded thin sections of the organ float to the water surface and are confined within a specific area. The sliced-off agarose-embedded thin sections sink to the bottom of the water tank. The imaging and sectioning process is repeated as required. Later, the serial 2D images are processed for 3D visualization. Note that, to avoid laser overload, we paused the laser for 30 minutes between consecutive raster scans. We did not observe any power drop of the laser throughout acquisition of all the volumetric images. With our current design and setting, the

imaging speed is limited by the laser repetition rate to 10^4 pixels per second. The lateral scanning

step size is 0.625 µm. At 10^4 pixels per second, the required scanning speed of a motorized stage

is ~6.25 mm/s. The motorized stage that we used for the fast scanning axis (PLS-85) can scan at

up to 50 mm/s. Therefore, the motorized stage is not the limiting factor on the imaging speed.
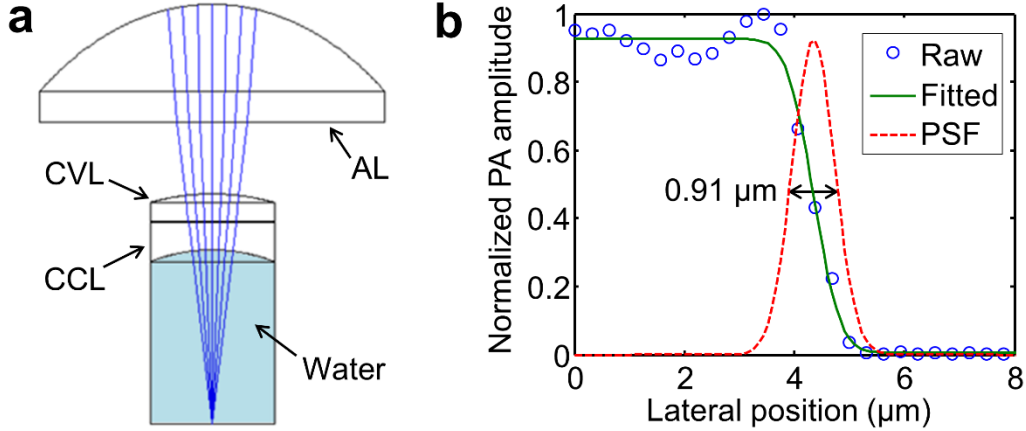
Figure 3.1 Resolution of mPAM. (a) Zemax design of the optical objective for focusing UV light into water. AL, aspheric lens; CCL, concave lens; CVL, convex lens. (b) By imaging a sharp edge and fitting the data to the error function, the system's point spread function (PSF), which is a product of two orthogonal line-spread functions, is obtained. The lateral resolution of mPAM, defined by the full-width at half maximum of the PSF, is 0.91 µm.

3.2.3 Lateral and Axial Resolution Measurements

The mPAM system's lateral resolution is determined by the optical focusing, because in the focal

plane only those biomolecules inside the optical focus are excited[64]. According to Zemax

simulation, the UV objective lens can provide a diffraction-limited resolution as fine as 0.34 µm

at 0.4 NA. But in practice the optical NA is limited to 0.16 by the size of the central hole of the

ring-shaped ultrasonic transducer. Accordingly, the lateral resolution is 0.91 µm, as validated by

experiments (**Fig. 3.1b**). The axial resolution of a linear photoacoustic system is determined by

the bandwidth of the ultrasonic transducer[65] (estimated as 25 µm for mPAM). However, here the

strong UV absorption from embedded organs is likely to be the limiting factor for axial resolution,

31

because the estimated imaging depth is ~20 μm (**Fig. 3.2**). Thus the axial resolution of mPAM is

~20 μm.
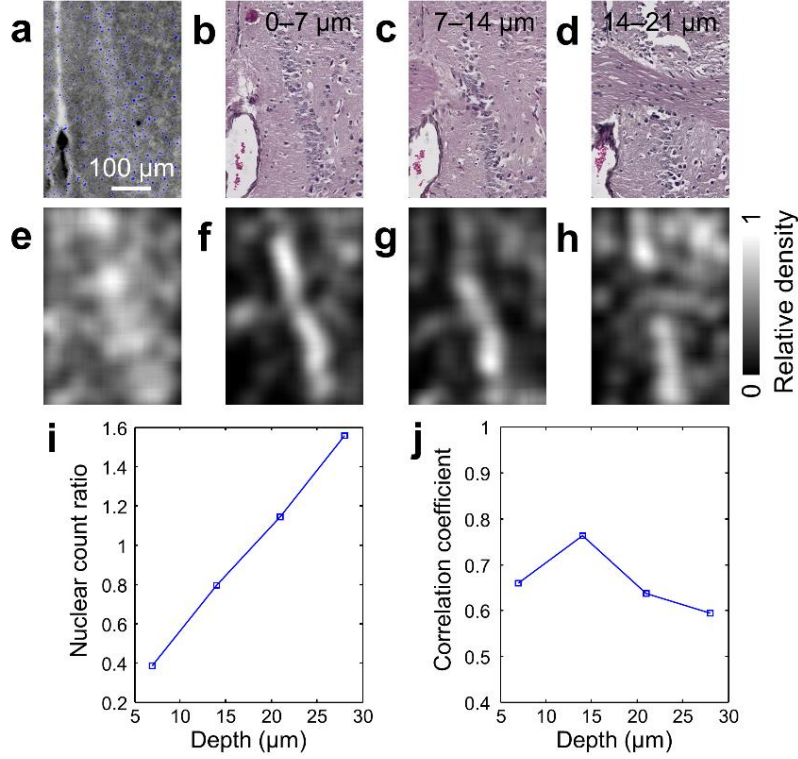
Figure 3.2 Imaging depth of mPAM in a tissue block. (a) mPAM image of a paraffin block surface, with nuclei marked in blue. (b)–(d) H&E images of paraffin sections sliced from the block surface in sequence, each with a 7 μm thickness. (e)–(h) Nuclear density maps of (a)–(d), respectively. (i) The ratio of the nuclear count in the H&E images within the given depth range to that in the mPAM image. (j) The correlation coefficient between the nuclear density map of the H&E images within the given depth range and that of the mPAM image.

3.2.4 Image Processing

We designed a Hessian filter to mathematically extract the cell nuclei from the 2D mPAM images

(**Fig. 3.3**). For a 2D image function $f(x, y)$, a Hessian matrix was constructed for each pixel[66]:

$$
H = \begin{bmatrix} \dfrac{\partial^2 f}{\partial x^2} & \dfrac{\partial^2 f}{\partial x \partial y} \\ \dfrac{\partial^2 f}{\partial x \partial y} & \dfrac{\partial^2 f}{\partial^2 y} \end{bmatrix}.
\tag{3.1}
$$

32

The two eigenvalues of H in equation (3.1) were then calculated. Negative and large eigenvalues suggest a bright and round local structure[66], i.e., a cell nucleus in our case. Hence the output image pixel value was set to either the product of the two eigenvalues if both were negative, or simply to zero otherwise. Last, a slight thresholding was applied to the output nuclear image to remove excessive background.
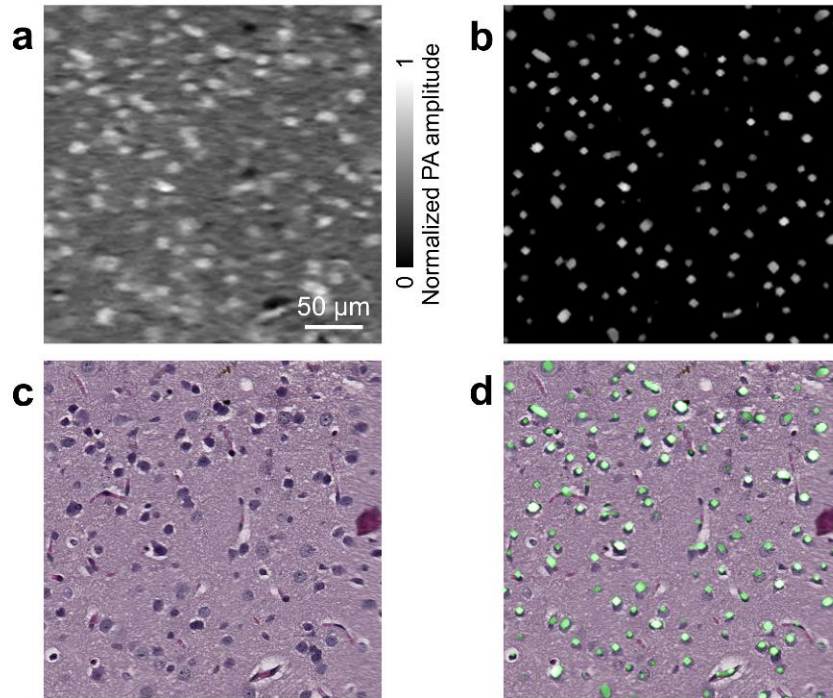
Figure 3.3 Comparison between mPAM and H&E images of a paraffin mouse brain section. (a) Label-free mPAM image. (b) Nuclei extracted from (a) by a Hessian filter. (c) Optical microscopy image acquired after H&E staining. (d) Superimposed image of (b) and (c), with (b) pseudo-colored in green.

When a paraffin block is imaged, the paraffin also generates photoacoustic signals and appears as granular structures in the images. These spurious "nuclei" were extracted by the Hessian filter in the paraffin areas. In this way, we separated tissue from paraffin automatically in the images (**Fig. 3.4**), based on the fact that tissue areas have a larger average pixel value and a smaller variation than paraffin areas. The local average and variation values were calculated for each pixel. The pixel was marked as tissue if the average was larger than an empirical threshold and the

variation was smaller than an empirical threshold, or marked as paraffin otherwise. Then the spurious nuclei in the paraffin areas were removed.
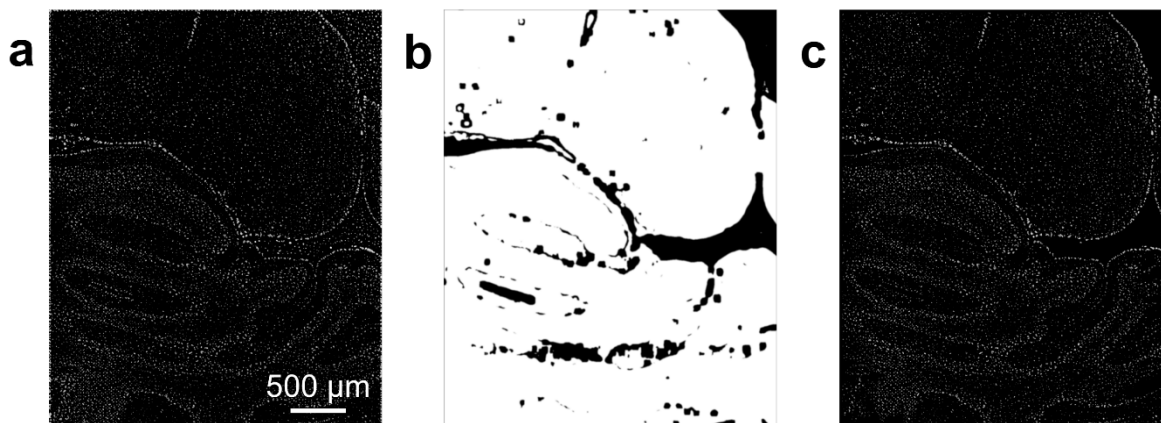
Figure 3.4 Extracting nuclei from label-free mPAM images of a mouse brain embedded in a paraffin block. (a) Fig. 3.7c processed by a Hessian filter. (b) Nuclear mask calculated from Fig. 3.7c, which separates tissue (bright) from paraffin (dark). (c) Nuclear image obtained by masking (a) with (b).

The serial 2D images acquired by mPAM were converted to step-through videos by Amira or MATLAB for 3D visualization. Image co-registration was not needed because the mechanical scanning was stable and the specimen suffered no sectioning deformation while being imaged.

3.2.5 Image Analysis

To evaluate the nuclear imaging results of mPAM, H&E images were used as the gold standard. We defined the nuclear sensitivity as the ratio of the number of true nuclei identified by mPAM to the number of all nuclei identified by H&E staining. Similarly, we defined the nuclear specificity as the ratio of the area of true non-nuclear tissue identified by mPAM to the area of all non-nuclear tissue identified by H&E, and defined nuclear PPV as the ratio of the number of nuclei that were true in the mPAM images to the number of all nuclei (including the spurious ones) identified in the mPAM images. To calculate the sensitivity, specificity, and PPV for **Fig. 3.5**, we selected and analyzed four regions of the brain, each containing 100–200 nuclei.
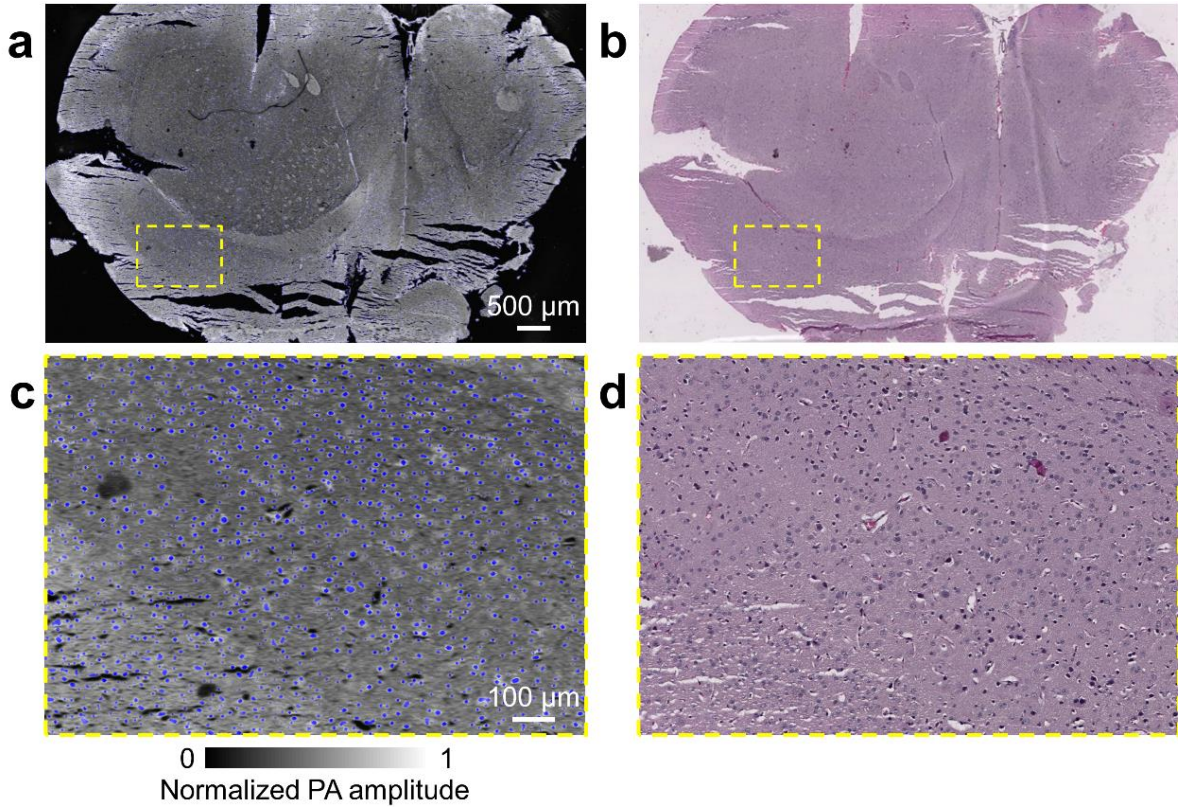
Figure 3.5 Imaging of a paraffin section of a mouse brain. (a) Label-free mPAM image, where the cell nuclei are enhanced by a Hessian filter and marked in blue. (b) Optical microscopy image acquired after H&E staining. (c),(d) Close-up images of (a) and (b), respectively, corresponding to the yellow dashed regions in (a) and (b). The nuclei are clearly resolved by mPAM.

To generate the nuclear density map, we first generated a nuclear image by Hessian filtering. Each nucleus in the image was reduced to one pixel with unit amplitude, and the background was set to zero amplitude. Then each pixel of this new image was replaced by the average of the $50 \times 50 \ \mu m^2$ surrounding area, creating a nuclear density map where each pixel value equaled the relative nuclear density of the $50 \times 50 \ \mu m^2$ surrounding area.

35

3.3 Results

3.3.1 mPAM System for Whole-organ Imaging and Sectioning

In mPAM (**Fig. 3.6a**), an organ (e.g., a mouse brain) or a tissue block, either formalin-fixed or
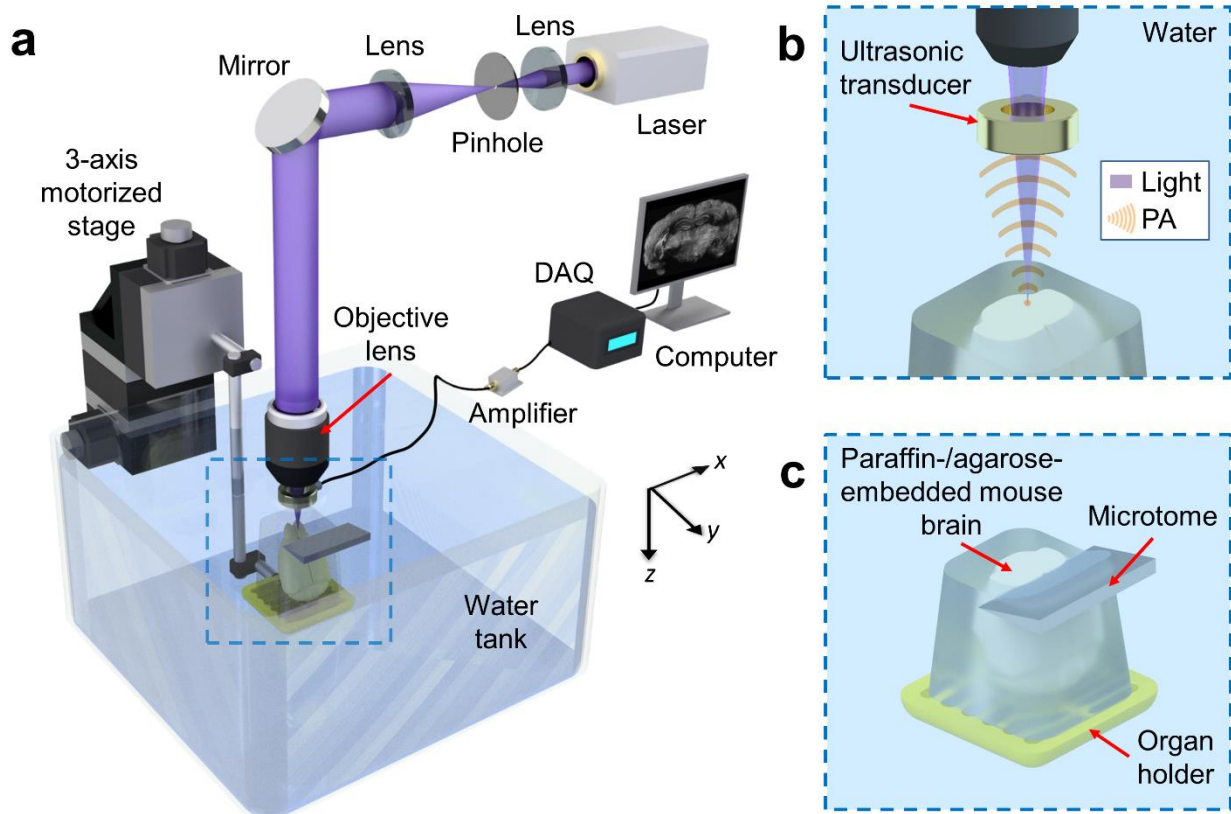
Figure 3.6 Schematic of the mPAM system for whole-organ imaging and sectioning. (a) The UV laser beam is first spatially filtered and expanded by a pair of lenses and a pinhole. The beam is then focused through an objective lens and passed through a ring-shaped ultrasonic transducer onto the surface of the paraffin-/agarose-embedded organ (e.g., a mouse brain), which is placed inside a water tank on top of a sample holder. Some generated acoustic waves propagate backward and reach the ring-shaped focused ultrasonic transducer. The received acoustic pressure is transduced into an electric signal, which is then amplified and recorded by a data acquisition (DAQ) card. During data acquisition, a maximum amplitude projection image from the measured B-scan data is displayed on a computer screen in approximately one second. By raster scanning the sample holder, a maximum amplitude projection image of the exposed tissue surface is also acquired. The imaged surface is then sectioned by a microtome, and a new surface is imaged automatically. This process continues until the sectioned layers reach the preset depth. (b) Close-up of the blue dashed region in (a) during imaging. The UV light passes through the ring-shaped focused ultrasonic transducer, inducing acoustic waves which are partially back-propagated and received by the same ultrasonic transducer. (c) Close-up of the blue dashed region in (a) during sectioning. The imaged surface's (cross section) is being cut by the microtome.

36

fresh, and paraffin- or agarose-embedded, is mounted on an organ holder immersed in water. The tissue is automatically imaged under a computer control. A laser generates pulses at 266 nm wavelength (and 420 nm for dual wavelength illumination) to predominantly excite DNA/RNA in the tissue, and the generated PA waves are detected by a ring-shaped focused ultrasonic transducer (**Fig. 3.6b**). The 3-axis motorized stage controls both the scanning for imaging and the tissue sectioning by the microtome. The mPAM system records and displays the cross-sectional images (e.g., coronal sections of a mouse brain) in real time during data acquisition. The exposed top tissue surface is imaged, then a thin layer is shaved off (**Fig. 3.6c**), and the new surface is imaged. This sequence is repeated to obtain a 3D image. The mPAM system currently provides a lateral resolution of 0.91 μm (**Fig. 3.1**), more than sufficient to image individual cell nuclei without labeling. Moreover, our mPAM system can handle organs of various sizes because it is implemented in reflection mode.

3.3.2 Imaging a Formalin-fixed Paraffin-embedded Mouse Brain

First, we validated the mPAM system by imaging a formalin-fixed thin paraffin section of a mouse brain (**Fig. 3.5**). The unstained paraffin section, fixed on a quartz slide that is UV transparent, was imaged by mPAM (**Fig. 3.5a**) and then stained with hematoxylin and eosin (H&E) (**Fig. 3.5b**) for comparison with conventional histology. The corresponding close-up images are shown in **Fig. 3.5c**, **d**, respectively. The cell nuclei in the mPAM image were enhanced by Hessian filtering (**Fig. 3.5a**, **c**) and are highlighted in blue. The step-by-step cell nuclear extraction results of the Hessian filtering are shown in **Fig. 3.3**. The grey matter and white matter can be differentiated in the mPAM image because the former has a higher density of nuclei than the latter. The nuclei in the mPAM image match well with those in the H&E image. Using the H&E image as the gold standard, in identifying nuclei, mPAM has a sensitivity of 93.2%, a specificity of 99.8%, and a positive

37

predictive value (PPV) of 96.7%. This experiment shows that mPAM can pinpoint cell nuclei sensitively and specifically in a paraffin-embedded organ section.

Next, we used mPAM to image a formalin-fixed and paraffin-embedded mouse brain block. Similar to imaging a thin section, a Hessian filter was employed for cell nuclear extraction (**Fig. 3.4a**). Compared with imaging a thin section, imaging an unstained paraffin block resulted in a stronger background, and thereby a lower image contrast for nuclei. The stronger background from paraffin caused false positive cell nuclear identifications, which could be eliminated by calculating the nuclear mask of the mPAM image (**Fig. 3.4b, c**). Due to UV-light attenuation, the nuclear signal was expected to decrease exponentially with depth. To estimate the mPAM imaging depth in the block (**Fig. 3.2a**), which is related to the selection of sectioning thickness in 3D mPAM, the mouse brain block was sectioned at the surface by a standard microtome for quantitative analysis. We obtained a series of H&E images of these sections, each 7 μm thick (**Fig. 3.2b–d**). Due to the deformation caused by sectioning, the nuclei in the H&E section images cannot be matched exactly with those in the mPAM block image (as we did in **Figs. 3.4**, **3.6**). However, the distributions of nuclei in the mPAM and H&E images are strongly correlated. To quantify this correlation, the nuclear count and nuclear density were calculated for these images (**Fig. 3.2e–h**). The ratio of the nuclear count in the H&E images within a given depth range to that in the mPAM image was calculated to be closest to unity for a depth range of 21 μm (**Fig. 3.2i**). The correlation coefficient was calculated between the nuclear density map of the H&E images within a given depth range and that of the mPAM image, yielding a maximum of 0.78 over a depth range of 14 μm (**Fig. 3.2j**). In fact, the sensitivity of mPAM to nuclei decreases gradually with depth, depending on both the light attenuation with depth and the absorption coefficients of different nuclei, but this phenomenon is difficult to model accurately and so is not taken into account. Given

the values of the nuclear count ratio and the correlation coefficient, we estimated that mPAM imaged 14–21 μm deep in the block.
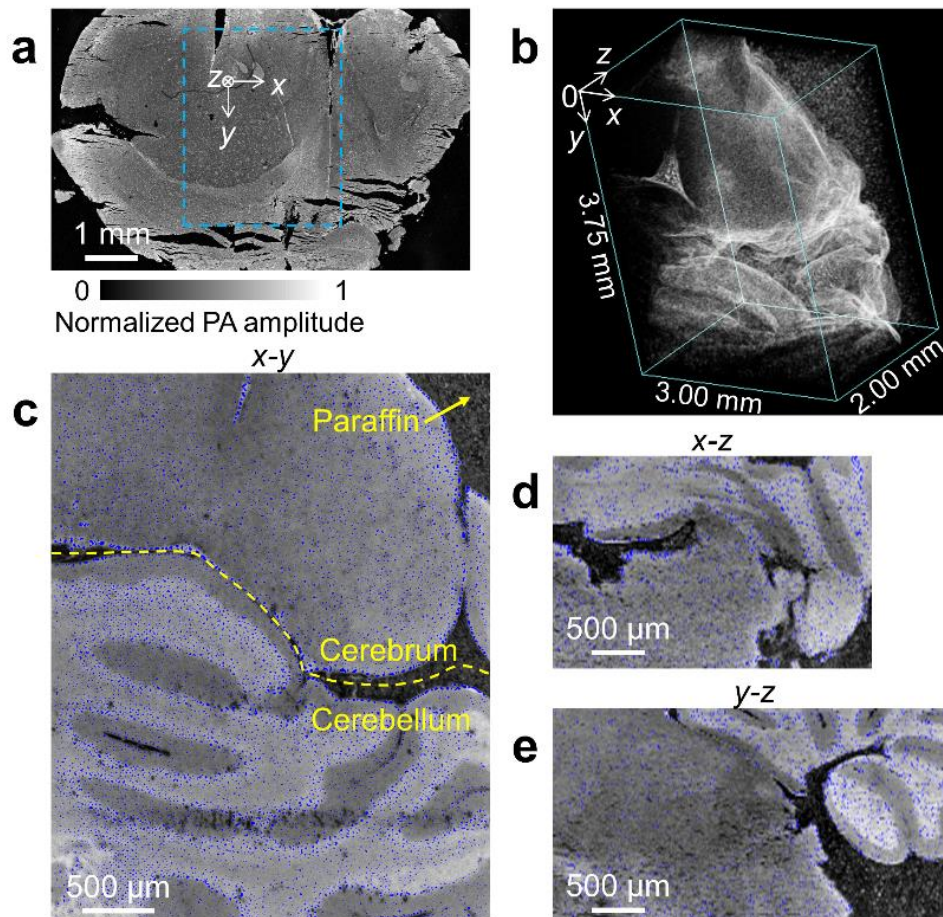
Figure 3.7 3D label-free mPAM image of an unstained mouse brain embedded in a paraffin block. (a) A section of the entire mouse brain image (coronal view). (b) A 3D view of the imaged brain block corresponding to the marked region in (a). (c) x-y image at $z = 0.16$ mm (coronal view), with the cell nuclei marked in blue. The yellow dashed line outlines the boundary between the cerebrum and the cerebellum. (d) x-z image at $y = 2.31$ mm (transverse view). (e) y-z image at $x = 0.63$ mm (sagittal view).

Next, we demonstrated the full capacity of mPAM for 3D high-resolution imaging (**Fig. 3.7**). An unstained mouse brain block (as used previously) was imaged on the surface (**Fig. 3.7a**) and sectioned repeatedly and re-imaged at 20 μm thickness by mPAM. The imaged volume of 3.0 mm by 3.8 mm by 2.0 mm (**Fig. 3.7b**) took ~70 hours for data acquisition. The volume covered both the cerebrum and the cerebellum (**Fig. 3.7c**). Representative x-y, x-z, and y-z images are

39

shown in **Fig. 3.7c–e**, respectively. Cell nuclei are highlighted in blue. Since the images were acquired at the block surface before sectioning, mPAM did not present artifacts of deformed or discontinuous structures, which are common problems in histology. In **Fig. 3.5b**, for example, deformation is especially evident at the bottom. The serial two-dimensional (2D) images were combined into a 3D image without the need for image registration. **Fig. 3.8** shows three snapshots of the 3D mPAM image of the mouse brain in different view angles. Individual cell nuclei can be clearly revealed in stepping through different positions and view angles.

Figure 3.8 Three snapshots of an mPAM volumetric image of a paraffin-embedded mouse brain with an imaging volume of 3.8 mm by 3.0 mm by 2.0 mm, in different view angles. (a)–(c) View angles 1– 3. The volumetric image was obtained by directly stacking 101 coronal sections with a 20 µm section thickness. The cell nuclei are extracted and shown as yellow bright dots.

3.3.3 Imaging Formalin-fixed Agarose-embedded Mouse Brains

We used agarose-embedded organs to further demonstrate applying mPAM to different embedding materials. The advantages of using agarose-embedding are two-fold: (i) Unlike paraffin, agarose is highly UV transparent and does not infiltrate into tissue[67], which improves the imaging contrast of mPAM, and (ii) agarose can be used for embedding fresh tissue[68], which enables mPAM to be readily used in life science studies. The only drawback is that agarose is a softer embedding material than paraffin, which limits obtaining thin sections. Nevertheless, a section thickness as small as 50–100 µm can be achieved with the integration of a vibratome[69], which is enough for numerous applications.

As an initial validation, a formalin-fixed paraffin-embedded mouse brain slice was imaged by mPAM and used as a reference (**Fig. 3.9a**). The slice was then deparaffinized, embedded in agarose, and re-imaged by mPAM (**Fig. 3.9b**). For comparison, an adjacent brain section was H&E stained and imaged by a conventional wide-field microscope (**Fig. 3.9c**). The corresponding close-up images are shown in **Fig. 3.9d–f**, respectively. The close-up images clearly show that a deparaffinized and agarose-embedded brain slice can reveal individual cell nuclei without any contrast enhancement algorithm, which was also validated with the H&E close-up image. Paraffin is a UV absorbing material that infiltrates tissue. Thus, when it was washed out (i.e., deparaffinized), the background signal was reduced, and the contrast of all the original tissue structures was boosted (**Fig. 3.9d, e**). This experiment shows that with agarose embedding, mPAM can pinpoint cell nuclei without any contrast enhancement algorithm, further improving the accuracy of cell nuclear identification.
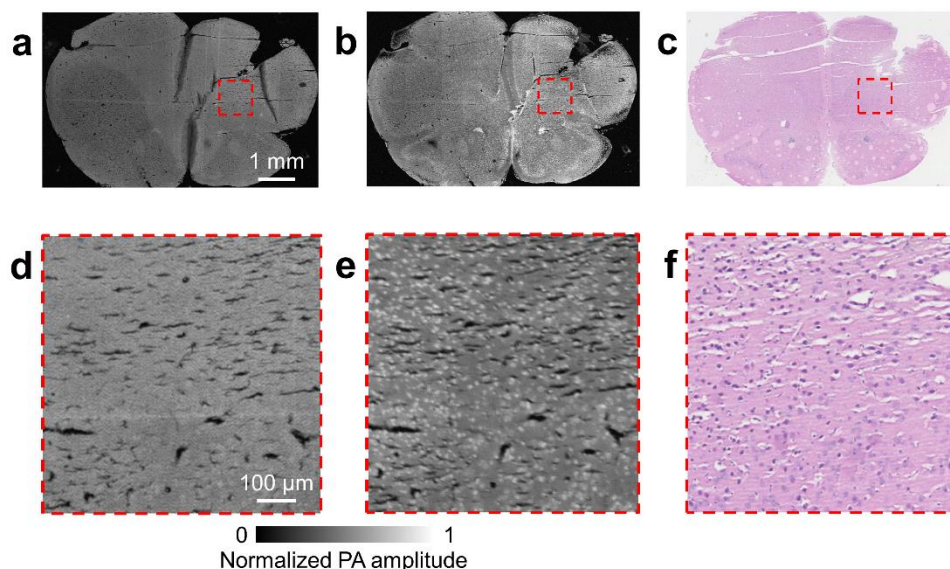
Figure 3.9 Imaging of paraffin-embedded and deparaffinized sections of a mouse brain. (a) Label-free mPAM image of the paraffin section. (b) Label-free mPAM image of the deparaffinized section. (c) Optical microscopy image of the adjacent section after H&E staining. (d)–(f) Close-up images of (a)–(c), respectively, corresponding to the red dashed regions in (a)–(c). The mPAM image of the deparaffinized section shows cell nuclei clearly without resorting to image processing by Hessian filter.

As a proof of concept with a microtome, we imaged an entire formalin-fixed agarose-embedded mouse brain, with a 200 µm section thickness. The imaged volume of 9.5 mm by 7.5 mm by 11.0 mm (**Fig. 3.10a**) took ~15 days for data acquisition. The lateral ventricles, hippocampus, and cerebellum can be observed in the 3D image, which was obtained by stacking 56 coronal sections of the mouse brain (**Fig. 3.10a**). Three representative individual coronal sections with their corresponding positions in the mouse brain are shown in **Fig. 3.11**. Three snapshots of close-up images of a row of representative coronal sections are shown in **Fig. 3.12** to illustrate the high imaging resolution of mPAM. To show high-quality coronal sections without the integration of a vibratome, which is the ideal sectioning tool for agarose-embedded organs[67], we used a larger sectioning thickness of 500 µm (**Fig. 3.10b–k**). The sections' corresponding positions are labeled in the 3D mouse brain mPAM image (**Fig. 3.10a**).
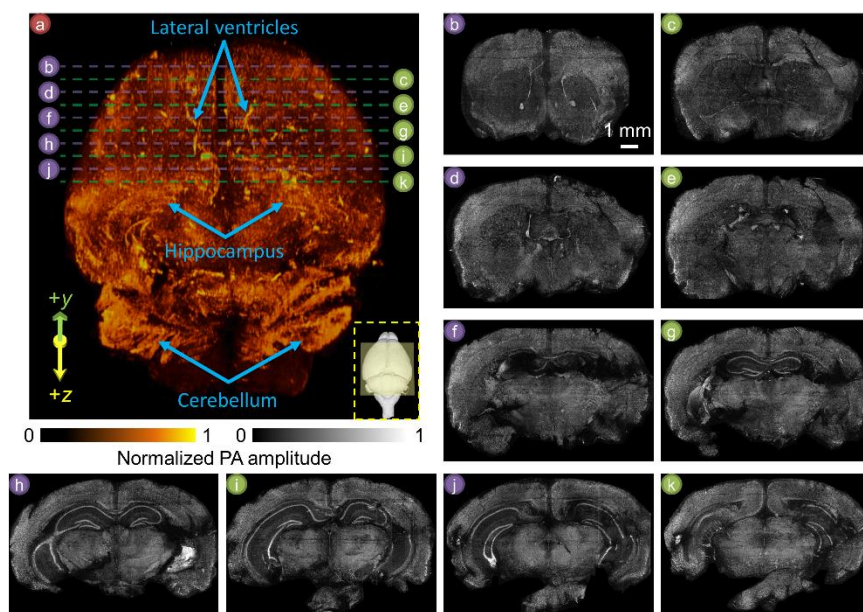
Figure 3.10 3D label-free mPAM image of an unstained mouse brain embedded in an agarose block.
(a) An mPAM volumetric image of a mouse brain with a sectioning step size of 200 µm. The bottom right yellow dashed inset shows the corresponding projection and its imaging area of a 3D mouse brain model[70] (yellow shaded region). Three features, namely the lateral ventricles, hippocampus, and cerebellum, are labeled on the 3D mPAM image. (b)–(k) The relative positions of ten coronal views are labeled in (a), and they are shown individually. The separation between each section is 500 µm.
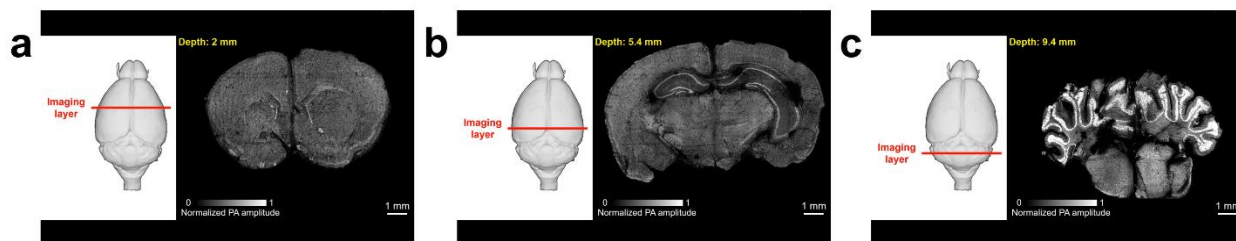
Figure 3.11 Three representative coronal sections of an agarose-embedded mouse brain imaged by mPAM. (a)–(c) Positions 1–3.The imaging field-of-view is 9.5 mm by 7.5 mm. A 3D mouse brain model is shown on the left[70], with a red line indicating the relative position of the current coronal section in the entire mouse brain.
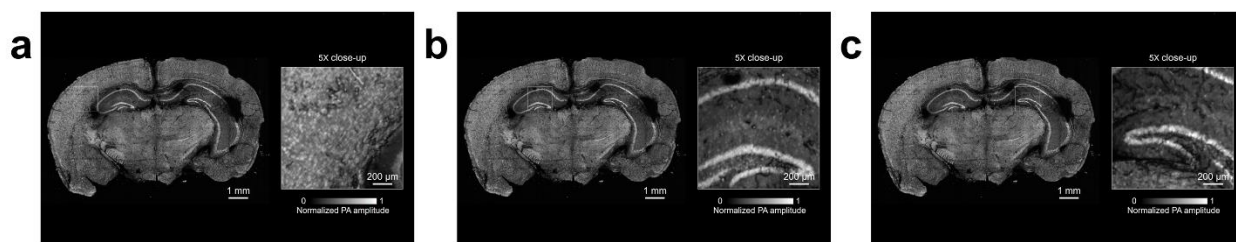
Figure 3.12 Three snapshots of a series of close-up images of a row of representative agarose-embedded mouse brain coronal sections imaged by mPAM. (a)–(c) Positions 1–3. The 5X close-up scanning window has a size of ~1.25 x 1.25 mm^2.

To further show the strength of label-free mPAM that many biologically important features of the mouse brain could be imaged, two more formalin-fixed agarose-embedded mouse brains were imaged with different sectioning thicknesses, 300 and 400 µm. Together with the aforementioned 200 and 500 µm sectioning thicknesses, we covered biological features that can be found in every 200, 300, 400, and 500 µm. **Fig. 3.13** shows a collection of images of features extracted from all four agarose-embedded mouse brains. These features clearly reveal the unique capability of label-free mPAM, which allows imaging of different biomolecules that otherwise would require different labeling/dyes for simultaneous visualization. For instance, the leftmost mPAM images in **Fig. 3.13a–c** show cell nuclei, blood vessels, and the olfactory limb by imaging DNA/RNA, hemoglobins, and lipids with UV light illumination alone. Moreover, features such as

43

myelinated axons and third ventricle can be imaged without staining due to their rich DNA/RNA and lipid contrasts (**Fig. 3.13d**). By illustrating all the features with a single imaging modality and minimal tissue processing, mPAM enables understanding and exploring the structural or connection changes of different biological structures under different conditions, such as different diseases and stages, with high fidelity.
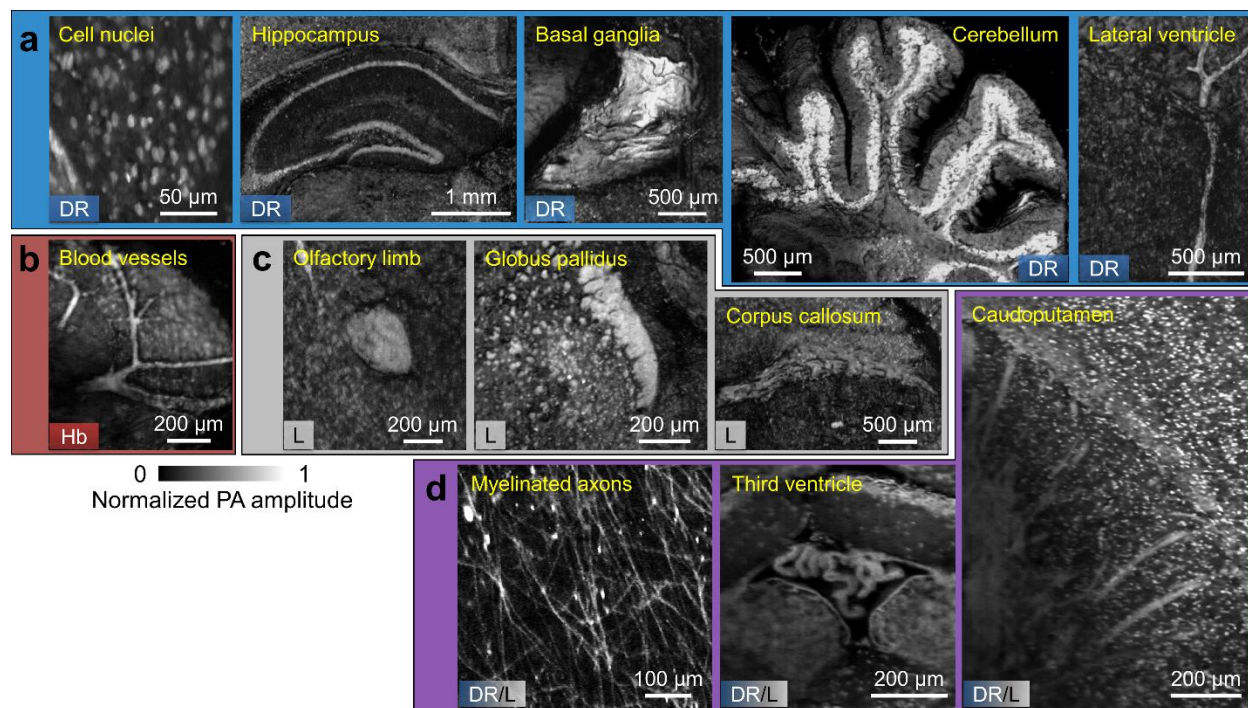
Figure 3.13 Image gallery of features extracted from label-free mPAM images of four unstained mouse brains embedded in agarose blocks. All features are shown in coronal view. Collections of images showing the biomolecules that provide absorption contrast due to (a) DNA/RNA (DR), (b) hemoglobins (Hb), and (c) lipids (L). (d) Images of myelinated axons, third ventricle, and caudoputamen due to both DNA/RNA and lipids contrasts.

To increase the imaging specificity, multi-wavelength illumination can be used to decouple signal contributions from different biomolecules[71], with each illumination wavelength falling into a strong absorption band of a biomolecule. To show that mPAM can image more endogenous biomolecules, we used dual-wavelength illumination (266 and 420 nm) to image an agarose-embedded brain slice (**Fig. 3.14a, b**). With 266 nm laser illumination, **Fig. 3.14a** shows mostly

DNA/RNA and lipid contrasts, whereas with 420 nm laser illumination, **Fig. 3.14b** shows mostly

cytochrome contrast. The overlay image (**Fig. 3.14c**) is displayed in two-channel pseudo colors,

which represent the optical absorption color contrasts of the biomolecules at the two wavelengths

and illustrates that more biomolecules are imaged by dual-wavelength mPAM than by single-

wavelength mPAM.
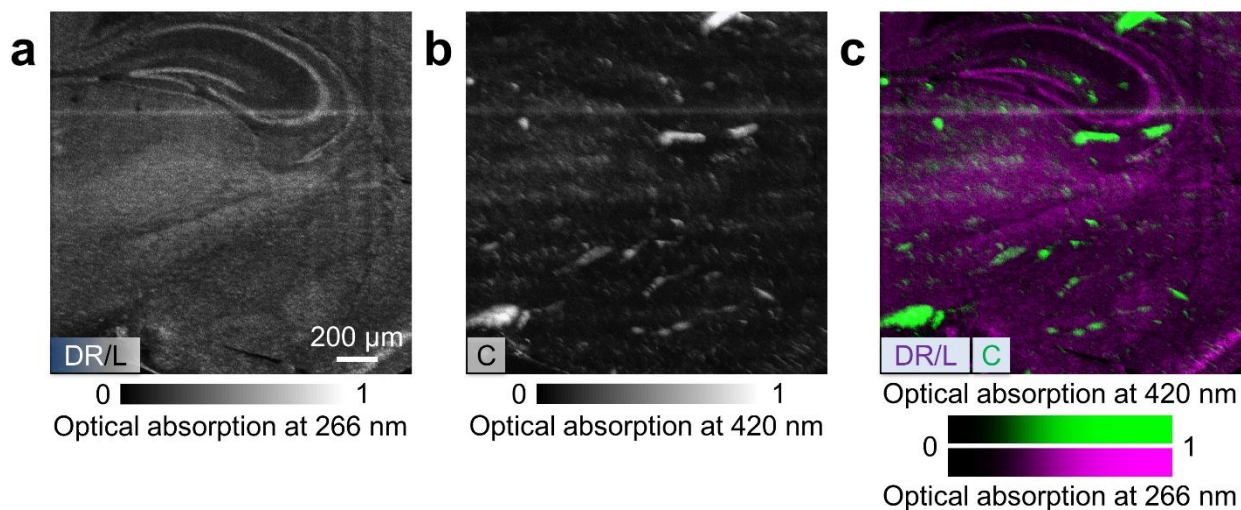
Figure 3.14 Imaging of an agarose-embedded mouse brain section by mPAM with dual wavelengths.
(a) Label-free mPAM image with 266 nm laser illumination, which mostly shows DNA/RNA (DR) and
lipid (L) contrasts. (b) Label-free mPAM image with 420 nm laser illumination, which shows cytochrome
(C) contrast. (c) Overlay image of (a) and (b), where pseudo colors are used to illustrate the optical
absorption color contrast of the biomolecules.

To show that deep tissue imaging can also be achieved with mPAM[72], we used 420 nm

light to illuminate a 1 mm thick mouse brain slice. A representative *xz* projected image of the

mouse brain is provided in **Fig. 3.15**, which shows cytochrome contrast based structures ~800 µm

deep. Therefore, where cytochrome is the target of interest, we can further reduce the number of

slices, resulting in even fewer sectioning artifacts.
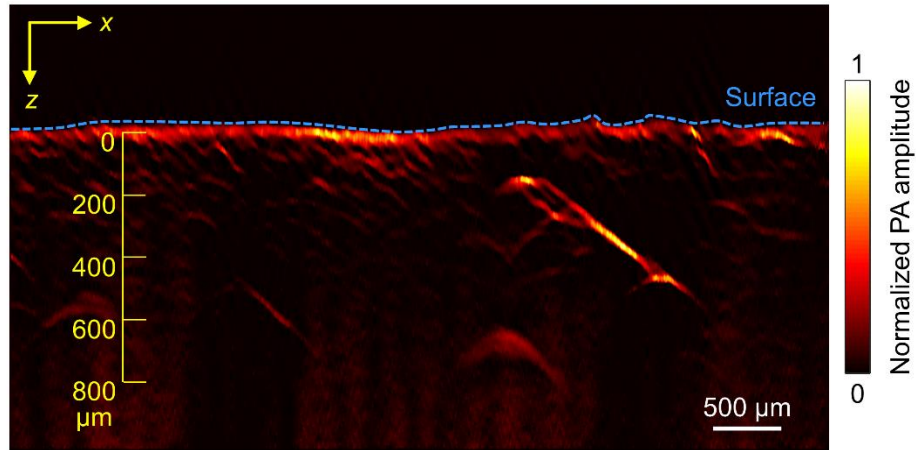
Figure 3.15 Representative *xz* projected 1 mm thick mouse brain image acquired over 6.0 x 0.1 mm². The blue dashed line outlines the surface of the mouse brain. With 420 nm light illumination, the deepest cytochrome contrast based structures are ~800 μm in depth measured from the mouse brain surface.

3.3.4 Imaging a Formalin-fixed Paraffin-embedded Mouse Lung and a Fresh Agarose-embedded Mouse Kidney

Finally, to demonstrate that label-free mPAM can image different organs and even fresh tissue, we imaged a mouse lung and kidney. The mouse lung was formalin-fixed and embedded in paraffin, and the fresh mouse kidney was embedded in agarose. For the mouse lung, two mPAM images of sections show different recognizable features (**Fig. 3.16a, b**). A close-up mPAM image of the paraffin-embedded mouse lung (**Fig. 3.16c**) shows that individual cell nuclei can be extracted (in blue). Similarly, to show the high-resolution 3D imaging capability of mPAM, we imaged 61 sections with a 20 μm section thickness. The imaged volume was 1.5 mm by 1.0 mm by 1.2 mm. Cell nuclei are shown clearly in different coronal sections (**Fig. 3.17**). For the fresh mouse kidney, an entire section was imaged by mPAM (**Fig. 3.16d**). A close-up mPAM image (**Fig. 3.16e**) clearly shows the typical fiber-like structures in the medulla region of the mouse kidney. These results indicate that mPAM can provide histology-like imaging of organs that are either formalin-fixed or fresh, and paraffin or agarose-embedded.
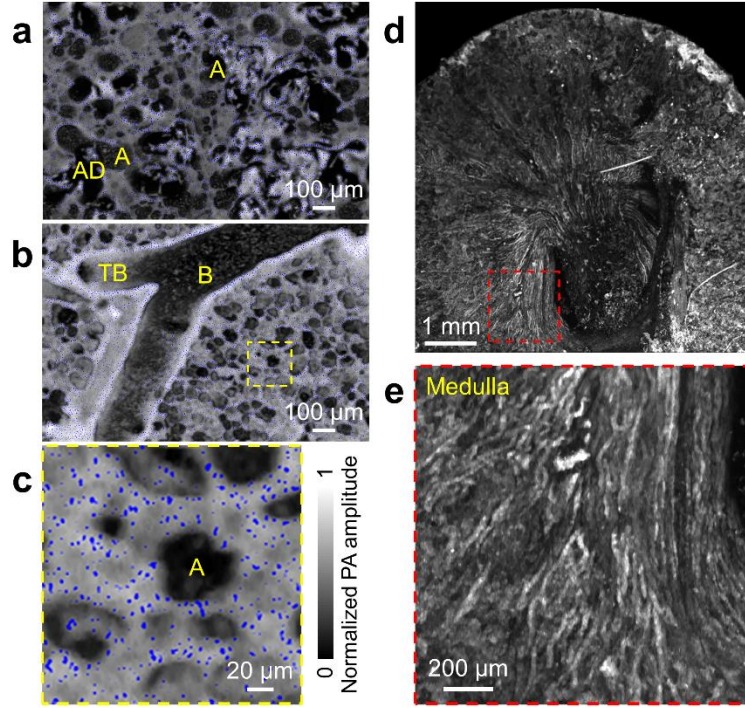
Figure 3.16 Label-free mPAM images of an unstained formalin-fixed mouse lung embedded in a paraffin block and an unstained fresh mouse kidney embedded in an agarose block. (a),(b) Two *x-y* sections of the mouse lung. (c) Close-up image of the yellow dashed region in (b). A, alveoli; AD, alveolar duct; B, bronchiole; TB, terminal bronchiole. (d) A *x-y* section of the mouse kidney. (e) Close-up image of the red dashed region in (d).
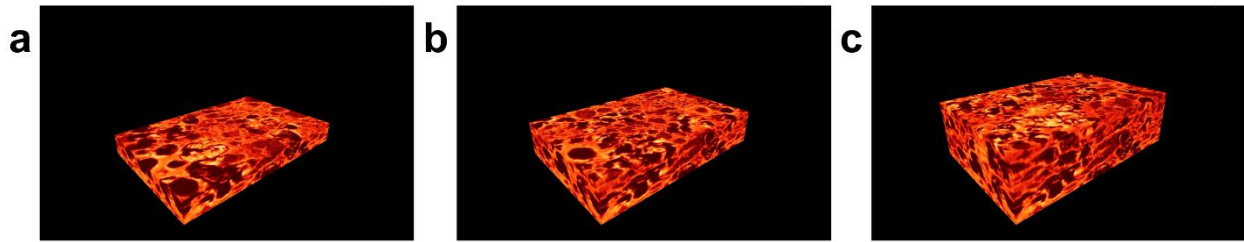
Figure 3.17 Three representative coronal views of an mPAM volumetric image of a paraffin-embedded mouse lung with an imaging volume of 1.5 mm by 1.0 mm by 1.2 mm. The volumetric image was obtained by directly stacking 61 coronal sections with a 20 µm sectioning thickness. The cell nuclei are extracted and shown as yellow bright dots.

3.4 Conclusions and Discussions

mPAM offers a new way to analyze disease-induced structural changes or the system function of

a whole organ. By imaging cell nuclei and blood vessels, mPAM can also serve as a minimal-

artifact substitute for histology. mPAM facilitates rapid 3D imaging of large tissue specimens. It can be readily applied to most standard paraffin blocks used in histology, e.g., paraffin blocks of an entire mouse brain or lung (**Figs. 3.7**, **3.8**, **3.16**, **3.17**). Such large volume registration-free histologic 3D imaging is impossible with any of the current choices for whole-organ microscopy. Moreover, mPAM can also be applied to fixed or fresh agarose-embedded tissue imaging (**Figs. 3.10–3.13**, **3.16**), and so should find broad applications in basic life science studies.

mPAM is currently in the early stages of development, and significant technical improvements will be realized in the future. First, the laser repetition rate of only 10 kHz made it very slow to image a whole organ (e.g., a mouse brain). In our experiment, it took ~70 hours to image about one-twentieth of the volume of a mouse brain, and ~15 days to image an entire mouse brain which was not densely sectioned. With the combination of a fast laser[73] and a fast scanning mechanism[37,74] in the future, the imaging speed is expected to be increased by two orders of magnitude, achieving subcellular imaging of a whole densely sectioned mouse brain within one day. In addition, by implementing multiple channels using a microlens array[42,75], the acquisition can be accelerated by additional orders of magnitude. Second, by incorporating the capability to employ more and different wavelengths in the future, mPAM can potentially probe many more endogenous biomolecules and specific cells, such as only neurons in brains, at their absorption peak wavelengths. Third, with the integration of a vibratome in the mPAM system, it is possible to achieve high-quality and densely sectioned images, even for agarose-embedded fresh tissue. With these further developments, mPAM may become a universal laboratory technique for whole-organ microscopy, with diverse applications in life sciences.

Chapter 4 Label-free Cell Nuclear Imaging by Grüneisen Relaxation Photoacoustic Microscopy

In Chapter 2, we have shown that photoacoustic microscopy (PAM) with ultraviolet (UV) laser illumination could be a promising imaging tool that provides fast, label-free, and multilayered histologic imaging of human breast tissue. Thus far, the axial resolution has been determined ultrasonically. To enable optically defined axial resolution, in this chapter, we exploit the Grüneisen relaxation (GR) effect. By imaging mouse brain slices, we show that GRUV-PAM reveals detailed information about three-dimensional cell nuclear distributions and internal structures, which are important diagnostic features for cancers. The work described in this chapter was published in Optics Letters[76].

4.1 Background

Photoacoustic (PA) tomography (PAT) has been demonstrated as a powerful tool in biomedicine, offering multi-scale imaging capability while providing rich optical absorption contrast[1, 34,77,78]. The absorption coefficient is an endogenous biomarker of various biological components in tissue. When tissue is irradiated by a short-pulsed laser, the absorption of the incident photons thermo-elastically generates wide-band ultrasonic waves, which can be detected by an ultrasonic transducer for image reconstruction. Because biomolecules all absorb differently at different wavelengths, PAT can selectively image different biomolecules with illumination laser

wavelengths properly chosen according to the biomolecules' absorption spectra. Among PAT implementations, optical-resolution photoacoustic microscopy (OR-PAM) achieves the highest resolution by tightly focusing the illumination region with a diffraction-limited light spot. OR-PAM has been used to image cell nuclei[35], cytoplasm[36], blood vessels[37], and organelles[79]. Depending on the specific absorption of DNA/RNA molecules, using ultraviolet (UV) exposure with OR-PAM is highly efficient for label-free cell nuclear imaging. The short wavelength of UV light allows focusing to a small light spot, providing subcellular resolution to reveal the morphological information of individual cell nuclei, which is significant for cancer diagnosis[40,80–82]. Recently, histology-like multilayered imaging achieved by UV OR-PAM has been reported[8,49], which could enable fast and label-free intraoperative margin assessment. However, similar to other conventional OR-PAM techniques, the axial resolution in the reported works is acoustically determined, limited by the acoustic bandwidth of the detected PA signal[65]. So far, the sectioning ability of conventional OR-PAM is insufficient to separate signals from different cell layers within one axial acoustic pixel, which decreases the contrast for cell nuclear visualization. To improve the axial resolution using optical sectioning, nonlinear effects can be utilized, such as two-photon absorption[83] and the Grüneisen relaxation (GR) effect[47,84–86]. The Grüneisen parameter of a material relates the thermally induced initial pressure to the thermal energy deposition. As the Grüneisen parameter is temperature dependent, it can be altered by transient light absorption and then relaxed to its baseline value over time (e.g., <1 µs), which is called the GR effect. In this Letter, we demonstrate that the GR effect can be combined with UV OR-PAM, and we achieve label-free optically sectioned images of cell nuclei, revealing their precise distribution in three dimensions, and even their internal structures in a cross-section. Moreover, compared with conventional linear UV OR-PAM (LUV-PAM) images, GRUV-PAM not only greatly improves

the sectioning ability, but also enhances the contrast between cell nuclei and their background

(which comes from other absorbers such as cytoplasm or out-of-focus cell nuclei). This work will

be important for further improving the performance of the UV-PAM system for histologic

imaging. The revealed internal structures in cell nuclei are vital features for making accurate

diagnoses.

4.2 Methods

In GR-PAM, a pre-heating laser pulse is fired before the main PA excitation pulse to obtain

nonlinear PA signals[47]. The pre-heating laser can be either a pulsed laser or a continuously working

laser with a brief on period, and it is coaxially focused at the same lateral position as the main laser

for PA excitation. The pre-heating increases the Grüneisen parameter of the irradiated sample,

which is a factor that affects the subsequently excited PA amplitude. The increased Grüneisen

parameter can be expressed by[2,47]:

$$\Gamma = \Gamma_0 + k\eta\mu_a F_1 \exp\left(-\frac{t}{\Delta}\right) \tag{1}$$

where Γ_0 is the original Grüneisen parameter at the baseline temperature; k is a linear factor

relating the increase of the Grüneisen parameter and the absorbed energy; η is the heat conversion

efficiency; μ_a is the optical absorption coefficient of the sample; F_1 is the optical fluence of the

pre-heating laser; and Δ is the thermal relaxation time, which is on the order of microseconds for

the targeted spatial resolution.

The PA amplitude, from a planer absorber which has a lateral dimension greater than the

optical focal diameter, caused by the sequential laser pulse F_2 can be calculated by the following

integration over the lateral plane[2,47]:

51

$$P = \iint \Gamma\eta\mu_a F_2 ds$$

$$= \iint \left(\Gamma_0\eta\mu_a F_2 + k\eta^2{\mu_a}^2 F_1 F_2 \exp(-\frac{t}{\Delta})\right) ds$$

$$= P_0 + k\eta^2{\mu_a}^2 \exp\left(-\frac{t}{\Delta}\right) \iint F_1 F_2 \, ds \tag{2}$$

where P_0 is the standard PA amplitude without pre-heating.

In GR-PAM, the nonlinear PA signals can be extracted by subtracting the PA signals without heating from the PA signals with heating. If F_1 and F_2 have the same spatial distribution but differ only in intensity by a constant factor theta, i.e., $F_1 = \theta F_2$, the nonlinear PA signals, termed GR signals (P_{GR}), can be computed by:

$$P_{GR} = P - P_0$$

$$= \theta k\eta^2{\mu_a}^2 \exp\left(-\frac{t}{\Delta}\right) \iint {F_2}^2 \, ds \tag{3}$$

The GR signal is proportional to $\iint {F_2}^2 \, ds$, which is no longer invariant with depth. Instead, it decays when absorbers are axially moved away from the optical focus. But in conventional OR-PAM, the PA signal stimulated by F_2 is proportional to $\iint F_2 \, ds$, which is a constant due to the conservation of the total optical energy at different depths. In other words, in GR-PAM, optical sectioning can be achieved in the axial dimension. If we take a Gaussian approximation for the light beam, the axial resolution Δz can be expressed by[47]:

$$\Delta z = 1.8\frac{\lambda}{NA^2} \tag{4}$$

where λ is the optical wavelength, and NA is the numerical aperture of the optical focal lens.

4.3 Results

4.3.1 GRUV-PAM System for Cell Nuclear Imaging

A schematic of the GRUV-PAM system is shown in **Fig. 4.1**. Two pulsed 266 nm lasers (10 kHz pulse repetition rate, QL266-010-O, CrystaLaser Inc., and Wedge-XF-266, Bright Solutions SRL) are each first spatially filtered and expanded by an assembly of a lens (LB4941-UV, Thorlabs Inc.), a pinhole (50 µm diameter, #59-257, Edmund Optics Inc.), and another lens (LB4374-UV, Thorlabs Inc.) to obtain single-mode laser beams. The two filtered beams are then spatially combined by a semi-transparent mirror (beam combiner, BSW20, Thorlabs Inc.). The combined beams are reflected upward by a mirror (PF10-03-F01, Thorlabs Inc.) and tightly focused by an aspheric lens (0.18 effective NA, AFL25-40-S-X, asphericon GmbH) to illuminate the sample from below. The sample is placed on a quartz slide, which provides a transparent window for UV light delivery and a flat sample surface for high quality imaging. For efficient acoustic coupling, the sample is placed beneath a plastic membrane at the bottom of a tank that is filled with water. The GR signal from the plastic membrane can be neglected because it absorbs UV light much less than cell nuclei and it is out of focus. A focused ultrasonic transducer (50 MHz central frequency, 85% bandwidth (one way), V214-BB-RM, Olympus NDT Inc.) is immersed in the water for sensitive PA signal detection. The detected signals are then electrically amplified (56 dB, two ZFL-500LN+, Mini-Circuits, Inc.) and sent to a data acquisition card (ATS9350, Alazar Technologies Inc.). Both conventional LUV-PAM and nonlinear GRUV-PAM C-scan images can be obtained by motorized raster scanning (PLS-85, PI miCos GmbH). Note that photodiodes

(PDA36A, Thorlabs Inc.) are used to measure and correct the lasers' pulse-to-pulse fluctuations for accurate mathematical extraction of the nonlinear PA signals.
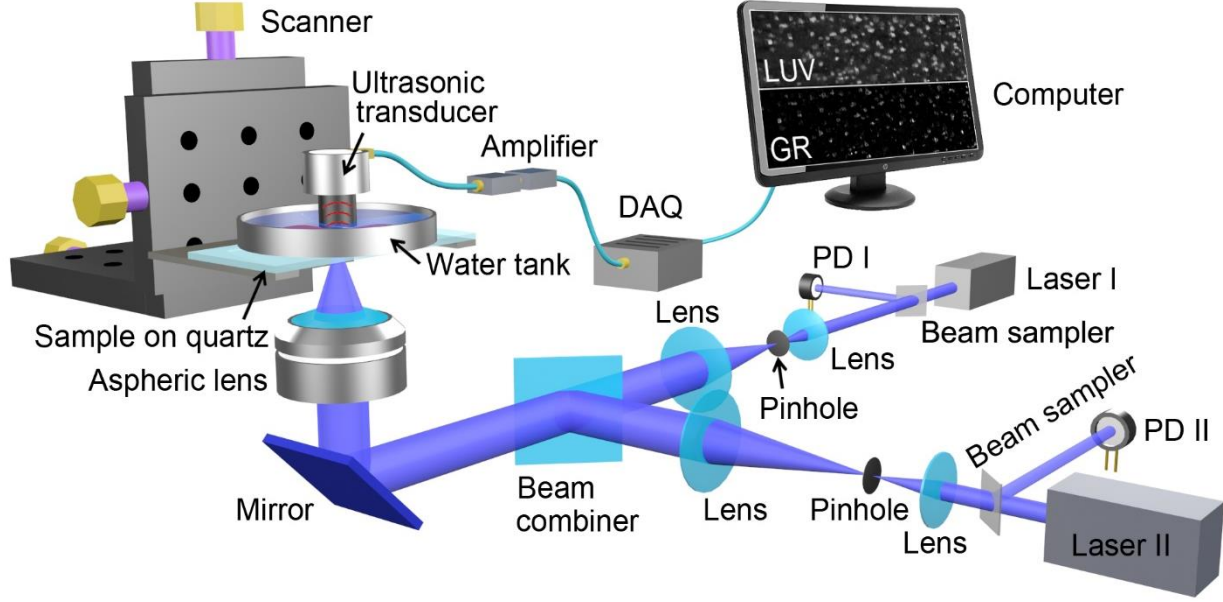
Figure 4.1 Schematic of the GRUV-PAM experimental system. PD, Photo diode; DAQ, Data acquisition card; LUV, LUV-PAM; GR, GRUV-PAM.

4.3.2 Study of the Improved Axial Resolution of the GRUV-PAM System

For demonstration, we imaged mouse brain slices with our GRUV-PAM system. To prevent photo-damage of the sample during scanning, the incident UV pulse energies of the two lasers were limited to about tens of nanojoules (10–25 nJ). Due to the small optical focal spots, the thermal relaxation time is short (<1 μs). Therefore, we used a short delay time, ~150 ns, between the two lasers, for efficient GR effect generation. The delay time was tuned by a delay generator. The pre-heating laser (laser I) had a pulse width of 2 ns, whereas the sequential one (laser II) had a pulse width of 700 ps (**Fig. 4.2a**). The PA signals generated by the first laser (P_0) were weaker than the signals generated by the second laser (P) primarily due to the GR effect (**Fig. 4.2b**). We imaged a cell nucleus using our GRUV-PAM system (The pulse energies of laser I and laser II were 15 nJ

54

and 8 nJ, respectively.). Both P and P_0 signals are plotted on the same time scale for comparison in **Fig. 4.2c**. According to the derivation above, the GR signals (P_{GR}) can be obtained by computing the difference between P and P_0. To show the sectioning capability of LUV-PAM in comparison to GRUV-PAM, we scanned the cell nucleus at different depths, with a step size of 6.25 µm. At each depth (i.e., axial position), we calculated the maximum amplitude projection (MAP) for both LUV-PAM and GRUV-PAM (**Fig. 4.2d**). GRUV-PAM clearly shows sectioning of the cell nucleus. Expectedly, LUV-PAM does not show any observable signal difference within 25 µm, which is still smaller than the acoustic resolution (~48 µm)[8]. The data points for GR are fitted with a Gaussian profile. The full width at half maximum (FWHM) is ~15 µm, which matches well with our theoretical estimation (14.8 µm) with the NA of 0.18 and wavelength of 266 nm[47].
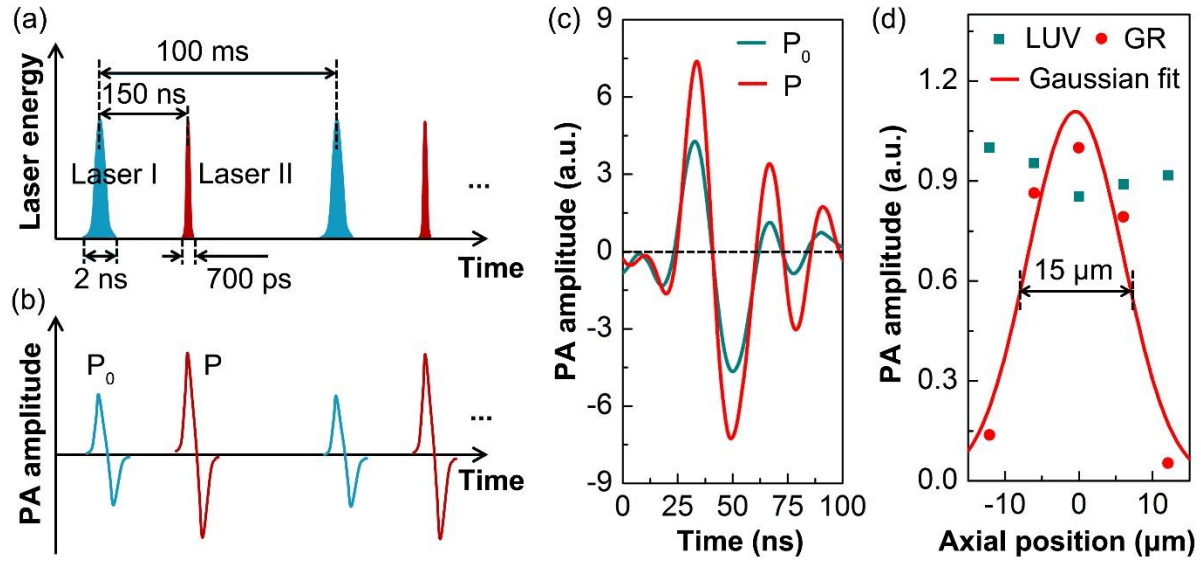
Figure 4.2 Study of the improved performance of the GRUV-PAM system. Schematics of (a) the laser pulse sequence and (b) the corresponding stimulated PA signals. The laser pair excites a mouse brain slice at a 10 kHz repetition rate. In each period, laser II is triggered 150 ns after laser I, which is well within the thermal relaxation time. (c) Experimentally measured PA A-line signal of a cell nucleus stimulated sequentially by laser I and laser II. The amplitude of P is greater than that of P_0 due to the GR effect. (d) Experimentally measured PA amplitudes of a cell nucleus at different optical focal depths. The FWHM of the Gaussian fit is ~15 µm.

55

4.3.3 Imaging a Mouse Brain Slice at Four Different Depths

Next, to show the optical sectioning capability of GRUV-PAM in three dimensions, we imaged a small portion of a mouse brain slice with an axial step size of 6.25 µm at four depths and a lateral step size of 0.94 µm, which was close to the lateral optical focal spot size of the current system. The theoretical lateral resolution is 0.64 µm, improved by $\sqrt{2}$ times over LUV-PAM. Because the main advantage of GRUV-PAM for cell nuclear imaging is its improvement in axial resolution, and to provide the optimal balance between resolution and scanning time, we have used a lateral step size that is slightly larger than the theoretical lateral resolution. Using these parameters for
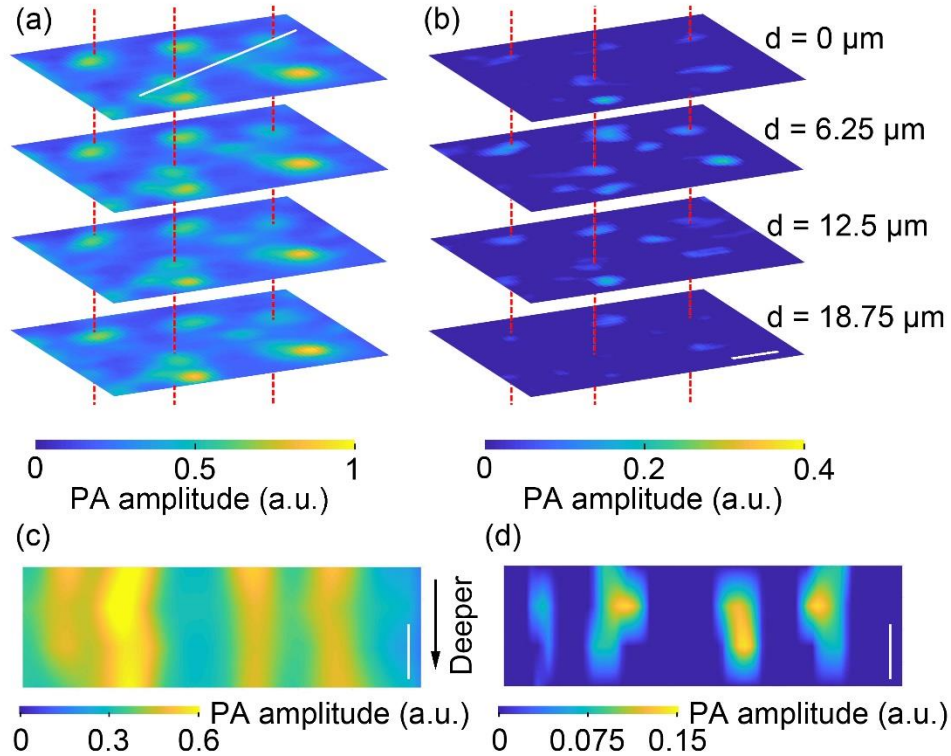
Figure 4.3 Comparison of (a) LUV-PAM and (b) GRUV-PAM images of cell nuclei in a mouse brain slice acquired at four different depths 6.25 µm apart. Only the nuclei near the focal plane appear in the GRUV-PAM images, while the LUV-PAM images show all the nuclei. Three pairs of cell nuclei are marked with red dashed lines for comparison. Depth resolved (c) LUV-PAM and (d) GRUV-PAM images along the white line marked in (a). Scale bars: 10 µm.

GRUV-PAM, the imaging speed was 4×10^4 μm^3/s. The pulse energies of laser I and laser II were 15 nJ and 8 nJ, respectively. In LUV-PAM, all the cell nuclei show similar brightness at different depths (**Fig. 4.3a**), whereas in GRUV-PAM, only the cell nuclei near the optical focal plane appear (**Fig. 4.3b**). Three cell nuclei are marked by red dashed lines to clearly indicate the same pair of nuclei for better comparison. To show the improved axial resolution, **Fig. 4.3c** and **d** show depth resolved LUV-PAM and GRUV-PAM images, respectively, along the white line marked in **Fig. 4.3a**. The results clearly demonstrate that the GRUV-PAM image (**Fig. 4.3d**) reveals individual cell nuclei, while the LUV-PAM image (**Fig. 4.3c**) shows uniform signals at different depths.

4.3.4 Imaging a Mouse Brain Slice with a Large Field-of-view

To further show the importance of GRUV-PAM for medical applications, we imaged a larger field-of-view (440×130 μm^2) of a mouse brain slice so that more cell nuclei could be seen (The pulse energies of laser I and laser II were 25 nJ and 20 nJ, respectively.). The LUV-PAM image is shown in **Fig. 4.4a**, and the GRUV-PAM image of the corresponding region is shown in **Fig. 4.4b**. After normalizing the two images, it is clear that the GRUV-PAM image (**Fig. 4.4b**) has better contrast than the LUV-PAM image (**Fig. 4.4a**). Within the zoomed-in regions in **Fig. 4.4a** and **b**, the internal structures of the cell nuclei are invisible in LUV-PAM (**Fig. 4.4c**), but are revealed in the GRUV-PAM image (**Fig. 4.4d**). These internal features are critical to making accurate diagnoses. GRUV-PAM also provides better contrast. To show the improvement of contrast quantitatively, we compared two line profiles of **Fig. 4.4a** and **b**. The contrast was quantified as $c = (PA_{max} - PA_{min})/PA_{min}$, where PA_{max} is the peak pixel value of the nucleus, and PA_{min} is the smallest pixel value of the nucleus. The contrast is enhanced by a factor of ~3.3 for the line profile in **Fig. 4.4e**. **Fig. 4.4f** shows that the out-of-focus signals from deeper nuclei or cytoplasm are suppressed, and thus a better contrast is achieved in GRUV-PAM.
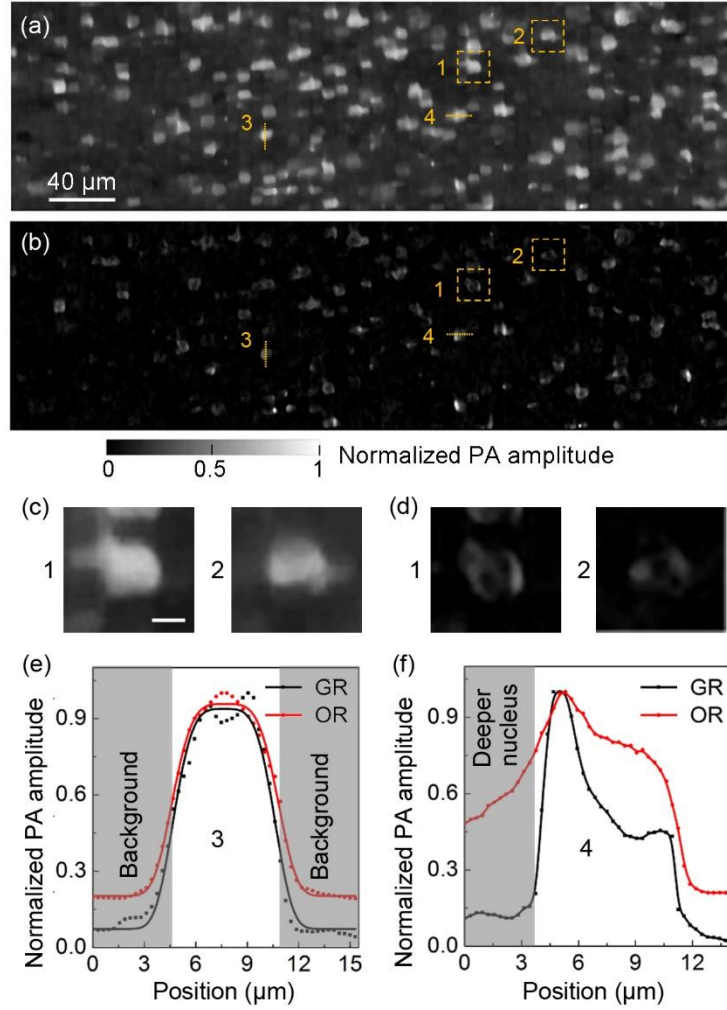
Figure 4.4 Comparison of (a) LUV-PAM and (b) GRUV-PAM images of the surface of a mouse brain slice. (c), (d) Zoomed-in views of the orange dashed box regions (1) and (2) in (a) and (b), respectively. (e) Cross-sectional normalized PA amplitude distribution along the orange line (3) in (a) and (b). (f) Cross-sectional normalized PA amplitude distribution along the orange line (4) in (a) and (b). Scale bar for (c) and (d): 5 µm.

4.4 Conclusions and Discussions

To conclude, we have developed a GRUV-PAM system with a 15 µm axial resolution. The theoretical lateral resolution is 0.64 µm. In comparing its performance with conventional LUV-PAM using mouse brain slices, the advantages of GRUV-PAM are clear. The sectioning capability is determined optically instead of acoustically. Benefitting from the optical sectioning imaging

58

capability of GRUV-PAM, accurate three-dimensional distributions and internal structures of cell nuclei can be revealed, which are important diagnostic features in many cancer diseases. Moreover, the contrast in cell nuclear imaging is also improved, which boosts the image quality further. An aspheric lens with a higher NA can be used to further improve both the axial and lateral resolutions. However, because a correspondingly smaller scanning step size would be needed and thus decrease the imaging speed, the optimal value of NA used in the system will depend on the specific application. Because two sequential excitations are needed in GR-PAM to trigger the nonlinear effect, the pulse energies should be controlled carefully to prevent any sample damage. In summary, we believe that, given its optical sectioning capability, UV-PAM will find potential applications in clinical settings.

Chapter 5 Use of a Single Xenon Flash Lamp for Photoacoustic Computed Tomography of Multiple-centimeter-thick Biological Tissue *Ex Vivo* and a Whole Mouse Body *In Vivo*

While lasers have been commonly used as illumination sources in photoacoustic imaging, their high purchase and maintenance costs, as well as their bulkiness, have hindered the rapid clinical dissemination of photoacoustic imaging. With this in mind, in this chapter, we explore an alternative illumination source for photoacoustic tomography — a xenon flash lamp with high pulse energy and a micro-second pulse width. We demonstrate that, by using a single xenon flash lamp, we can image both a black latex cord placed in chicken breast tissue at a depth of up to 3.5 cm *ex vivo*, and an entire mouse body *in vivo*. Our findings indicate that the xenon flash lamp, producing optical illumination that is safe for humans, can be potentially applied to human tissue imaging. The work in this chapter has been published in *Journal of Biomedical Optics*[87].

5.1   Background

In recent years, photoacoustic (PA) tomography (PAT) has demonstrated its capability of providing noninvasive, real-time imaging of significant anatomical and physiological information

and shown great potential to impact the clinical assessment and treatment of diseases[33,34,88]. In PAT, pulsed lasers have long been the typical sources of illumination. Their superior pulse energy and short pulse duration provide strong acoustic waves for sensitive detection and high image resolution[2,89]. However, other features of the laser, such as its spatial and temporal coherence, are often unnecessary for efficient PA wave generation. More importantly, lasers' high cost, maintenance fees, laborious maintenance procedures, and bulky sizes hinder the rapid development of PAT for clinical usage. Clearly, a cost-effective and compact alternative illumination source would benefit certain applications. To this end, researchers have investigated pulsed laser diodes (LDs)[90–93], light emitting diodes (LEDs)[94,95], and xenon flash lamps (XFLs)[96]. Using pulsed LDs, Upputuri et al. have imaged a blood-filled tube in chicken breast tissue up to 2 cm deep[93]. However, pulsed LDs are typically available only at wavelengths greater than 800 nm, which limits the choices of label-free absorption based contrasts. Using LEDs, Adachi et al. have successfully imaged printed characters[95]. However, modulated LEDs have a long pulse width, which limits the bandwidth of the acoustic signals[2,89]. Although Allen et al. have recently demonstrated that overdriving LEDs could provide a much shorter pulse width (200 ns), which improved the acoustic wideband, the pulse energy was only ~10 µJ[94]. In comparison, a XFL has a much wider spectrum, a much higher pulse energy, and a sufficiently short pulse width. However, previous demonstrations by Kruger[96] used a XFL with a relatively long temporal pulse width of ~5 µs, which severely degraded the image resolution. Therefore, Kruger did not provide PA images. In this work, we re-visited the XFL idea and demonstrated, for the first time, the use of a single XFL with high pulse energy and short temporal pulse width for photoacoustic computed tomography (PACT) of both biologically mimicking phantoms and tissues *ex vivo* and an entire

mouse body *in vivo*. Traditional pulsed laser based PACT has been used for performance comparisons.

5.2 Methods

5.2.1 Xenon Flash-Lamp-Based Photoacoustic Computed Tomography (XFL-PACT)

Fig. 5.1a and **b** show schematics of our laser and XFL experimental setups, respectively. For laser illumination (**Fig. 5.1a**), we used a Q-switched Nd:YAG laser (Brilliant B, Quantel). The laser pulse energy was ~5 mJ, with a ~5 ns pulse width. The laser beam was reflected by a prism to illuminate the sample from the top. An optical diffuser homogenized and expanded the laser beam. For acoustic wave detection, a focused ultrasonic transducer (Olympus, 25.4 mm diameter, and 25.4 mm focal length) was immersed in water on the same plane as the sample. The ultrasonic transducer was circularly scanned around the target in the trajectory shown by the orange dashed lines in **Fig. 5.1a–e**. The ultrasonic transducer was replaced by a ring-shaped ultrasonic transducer array with 512 elements to improve the signal-to-noise ratio (SNR) with more averaging and to avoid mechanical scanning for imaging fast dynamics (**Fig. 5.1f** and **g**).

For the XFL setup (**Fig. 5.1b**), the optical system was simplified by directly illuminating the sample with the XFL (L4634, Hamamatsu Photonics K. K.). The spectrum of the XFL light spanned from 240 to 2000 nm (**Fig. 5.2**). The repetition rate could be tuned from 10 to 100 Hz. The pulse energy was ~3 mJ with ~1 μs pulse width. The divergence angle and output beam diameter were ~15° and ~2 cm, respectively. Thus, with 6 cm spacing between the lamp's output and the sample plane, the illumination light diverged enough to cover an imaging area of ~20 cm^2.

Note that the circuit of the XFL was modified by externally adding two 0.1 µF capacitors in order to operate the XFL at its highest possible output. The ANSI maximum permissible exposure (MPE) on the skin surface is 20 mJ/cm^2 for the visible spectral range—covering most of the XFL spectrum, while the MPE is 3 mJ/cm^2 for the ultraviolet spectral range[97]. Nevertheless, the XFL fluence on the object surface is only ~0.15 mJ/cm^2. Therefore, XFL illumination is safe for human subjects and well within the ANSI safety limits.
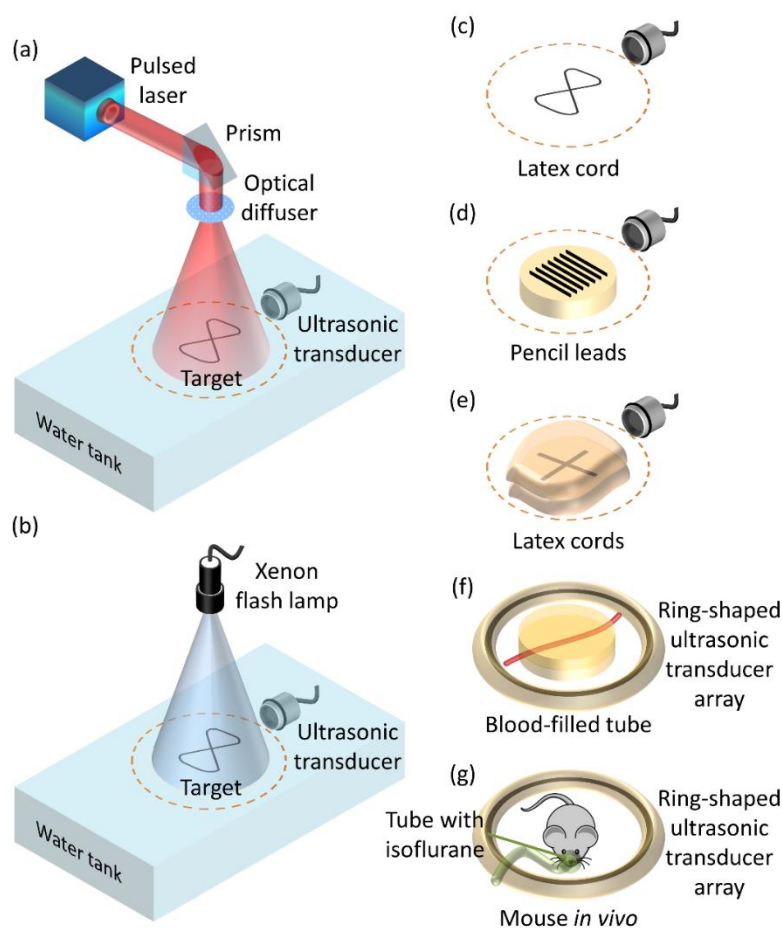
Figure 5.1 Schematics of the experimental setups and imaging targets. Experimental setups for (a) laser illumination and (b) XFL illumination. Targets used in the experiments: (c) pure latex cord; (d) pencil leads laid on an agar-water gel; (e) latex cords sandwiched by pieces of chicken breast tissue with the same thickness; (f) blood-filled tube embedded in agar-water gel; (g) a live mouse. The dashed circles in (a)–(e) represent the scanning trajectory of the ultrasonic transducer. A ring-shaped ultrasonic transducer array was used for targets (f) and (g).
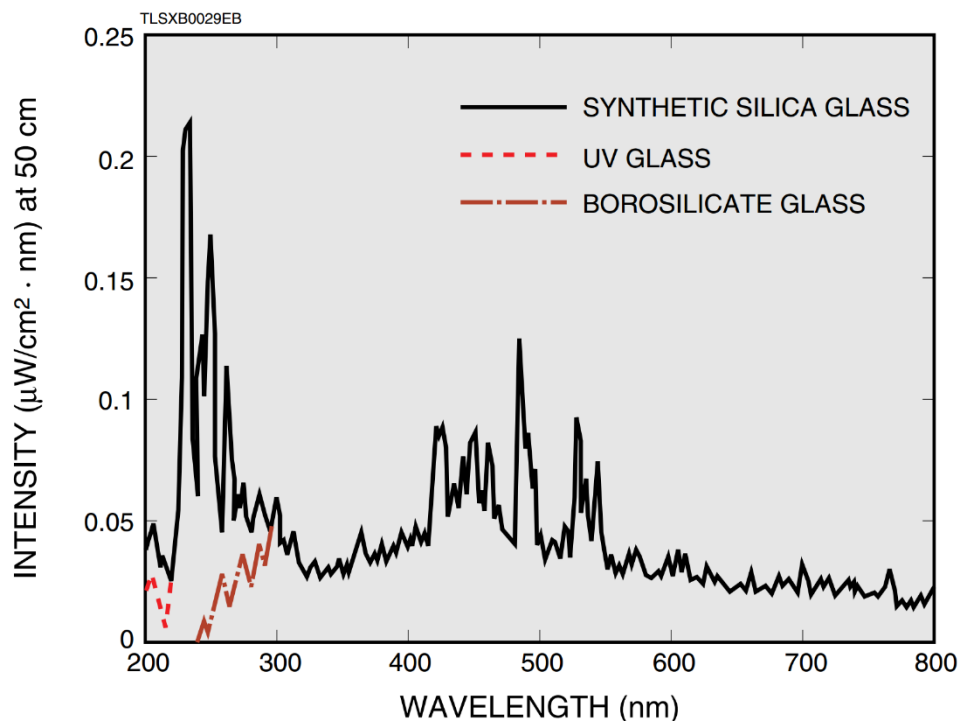
Figure 5.2 Spectra of the XFL with various housings extracted from its specifications. Borosilicate glass is used for our XFL. (https://www.hamamatsu.com/resources/pdf/etd/Xe-F_TLS1003E.pdf, Hamamatsu Photonics K. K.).

5.3   Results

To reveal the potential of using a high-energy pulsed XFL as an alternative light source in PACT, two different latex phantoms, one pencil lead phantom, two blood-filled tube phantoms, and a live mouse were used: (i) a latex cord with a diameter of 1.5 mm, bent into the shape of the number "eight" (**Fig. 5.1c**), (ii) seven pencil leads with a diameter of 0.7 mm, laid on the surface of an agar-water gel (**Fig 5.1d**), (iii) the same latex cords in a cross shape, sandwiched between pieces of chicken breast tissue (**Fig. 5.1e**), (iv) blood-filled tubes with a diameter of 1.5 mm, embedded 1 cm deep in an agar-water gel without and with a scattering medium (**Fig. 5.1f**), and (v) an entire mouse body *in vivo* (**Fig 5.1g**).

64

5.3.1 Study of the Feasibility with XFL-PACT

First, to validate the feasibility of using a XFL in PACT, a latex cord (**Figs. 5.1c** and **5.3a**) was imaged. The number "eight" shape enabled examining both the *x*-axis and *y*-axis resolutions. To find the optimal ultrasonic transducer for xenon flash-lamp-based PACT, four focused ultrasonic transducers with varied center frequencies (0.5, 1.0, 3.5, and 5.0 MHz) were used to image the same phantom. The single-element ultrasonic transducers scanned around the phantom circularly in 400 steps. **Fig. 5.3b–e** show the reconstructed images acquired with XFL illumination (hereafter referred to as flash-lamp-excited images) using the set of ultrasonic transducers. The flash-lamp-excited images acquired by 0.5 and 1.0 MHz ultrasonic transducers both show clear features of the phantom with high contrast. However, the other two images, acquired by 3.5 and 5.0 MHz ultrasonic transducers, are barely recognizable. A possible reason for this difference is that the pulse width of the XFL is relatively long (~1 μs), which limits the frequencies of PA signals less than 1 MHz. The contrast-to-noise ratio (CNR) was calculated as the mean of the enveloped PA amplitude in the region of interest (ROI) minus the mean of the enveloped background PA amplitude, divided by the standard deviation of the enveloped background PA amplitude, where the ROI is the target region. The CNRs for **Fig. 5.3b–e** are 24.2, 22.2, 1.1, and 1.0, respectively. To better analyze the two images with high contrast, frequency spectra of the corresponding raw data are shown in **Fig. 5.3g**. As shown by the frequency spectra, using a 1 MHz ultrasonic transducer provides only a slight resolution improvement over that achieved by using a 0.5 MHz transducer. This modest improvement was because the two data sets consist of similar frequency components, which were all <1 MHz. Therefore, to generate the flash-lamp-based PACT images with the highest CNR, the 0.5 MHz ultrasonic transducer is the best option.
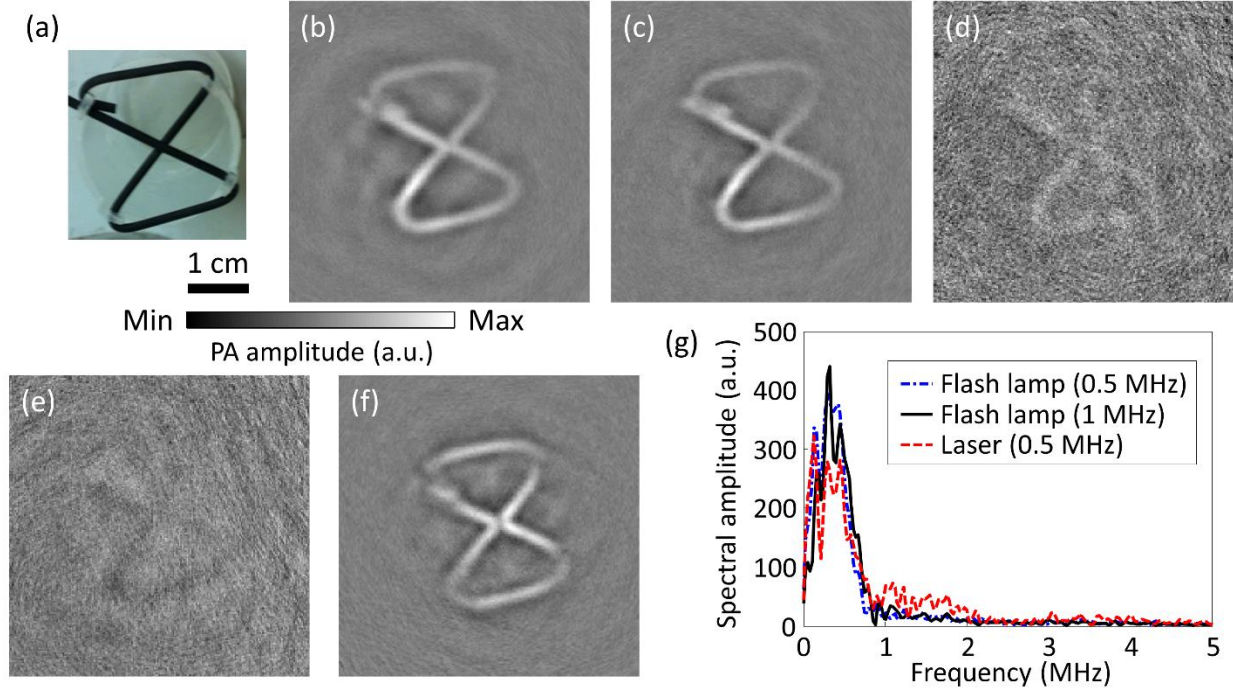
Figure 5.3 PACT images and frequency spectra of the pure latex cord acquired using laser or XFL illumination and ultrasonic transducers with varied center frequencies. (a) Photograph of the pure latex cord. PACT images acquired with XFL illumination and (b) 0.5, (c) 1.0, (d) 3.5, and (e) 5.0 MHz ultrasonic transducers. (f) PACT image acquired with laser illumination and the 0.5 MHz ultrasonic transducer. (g) Averaged frequency spectra of the raw photoacoustic signals acquired with the laser and XFL illumination.

By comparing the flash-lamp-excited and laser-excited images acquired with the same 0.5 MHz ultrasonic transducer (**Fig. 5.3b** and **f**), similar features can be observed, despite insignificant image blurring due to the long pulse width of the XFL. A spectral analysis was performed for further comparison between **Fig. 5.3b** and **f**. As shown in **Fig. 5.3g**, similar spectra can be observed, except for the frequency components ~>1 MHz, where the relative (with respect to components < 1 MHz) spectral amplitude of the laser-acquired data is higher. Thus, with 0.5 MHz ultrasonic transducer acquisition, the quality of the image produced by XFL excitation is similar to that of the image produced by laser excitation. In the following experiments, we chose the 0.5 MHz focused ultrasonic transducer for all measurements.

66

5.3.2 Study of the Imaging Resolution with XFL-PACT

To characterize the imaging resolution of XFL-PACT, seven pencil leads were placed 6 mm apart atop an agar-water gel (3% agar) which held the pencil leads in place (**Figs. 5.1d** and **5.4a**). Laser-excited and flash-lamp-excited images are shown in **Fig. 5.4b** and **c**, respectively. The imaging resolution was defined as the full-width-at-half-maximum of the reconstructed signals in the direction perpendicular to the pencil leads. Five adjacent line profiles perpendicular to the pencil leads were used to calculate the average imaging resolutions for both flash-lamp-excited and laser-excited images. **Fig. 5.4d** plots their imaging resolutions versus their off-center distances. The two resolution plots overlap highly, showing that the short pulsed XFL preserves the imaging resolution well. The average in-plane imaging resolution within the 25 mm radius area is ~1.5 mm for both the laser-excited and flash-lamp-excited images.
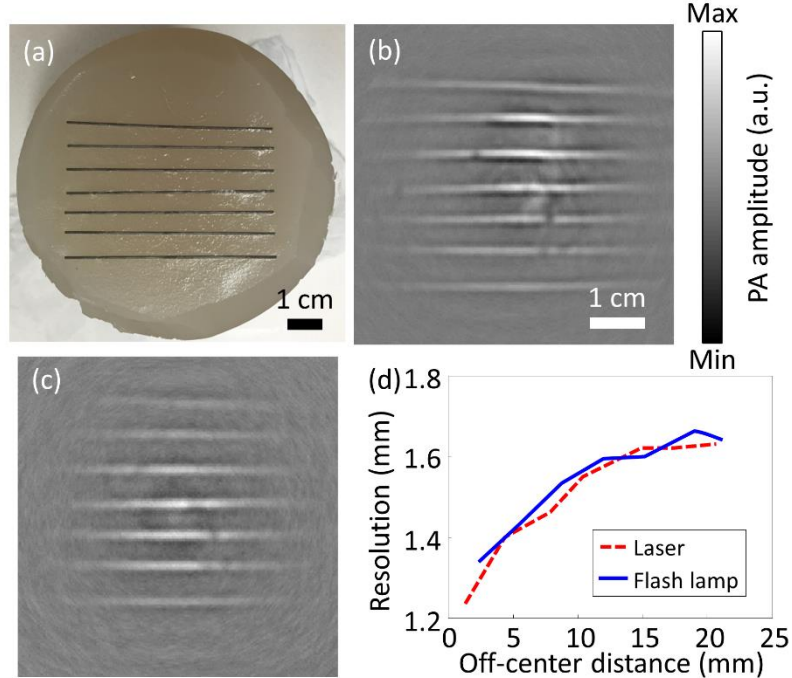
Figure 5.4 PACT of a pencil lead phantom. (a) Photograph of the pencil lead phantom. PACT images acquired with (b) laser and (c) XFL illumination. (d) Plots of resolution versus the off-center distance of this line phantom.

5.3.3 Study of the Maximum Imaging Depth with XFL-PACT

To demonstrate the practicability of using a XFL for biomedical applications like deep tissue imaging, we carried out another experiment to explore the maximum depth where a recognizable PA image can still be achieved. Here, we sandwiched two crossed latex cords (**Fig. 5.1e**) between pieces of chicken breast tissue, with the same thickness on the top, bottom and sides. **Fig. 5.5a** is a photograph of the phantom with the top pieces of chicken breast tissue removed. Note that the bottom and side chicken breast tissue was essential to prevent any stray light from bypassing the top chicken breast tissue and illuminating the latex cross via an unscattered path. Hence, no matter how the light traveled, it always traversed, at the least, the preset thicknesses of chicken breast tissue. To determine the maximum penetration depth, chicken breast slices with different thicknesses (1.0, 2.0, 3.0, 3.5, and 4.0 cm) were used to sandwich the cross phantom. The corresponding reconstructed images are shown in **Fig. 5.5b–f**. Four times averaging was used to improve the SNR by a factor of 2 without significantly lengthening the scanning time. All the reconstructed images, except the image sandwiched by 4.0 cm thick chicken breast tissue, clearly show the cross structures, with different extents of artifacts. Artifacts around the cross structures can be suppressed by better sandwiching the latex cords to reduce air bubbles between the interfaces. The CNRs for **Fig. 5.5b–e** are 16.7, 8.6, 4.6, and 2.9, respectively. As shown in **Fig. 5.5g**, the best fitting exponential decay curve proves that CNRs decay exponentially with penetration depths. Our experimental results supported that a single XFL could achieve 3.5 cm deep tissue imaging of black latex cords with a CNR of around 2.9, which is enough for many biomedical applications, such as human breast cancer and skin melanoma imaging. Note that multiple XFLs can be used to further improve the CNR and thus the penetration depth.
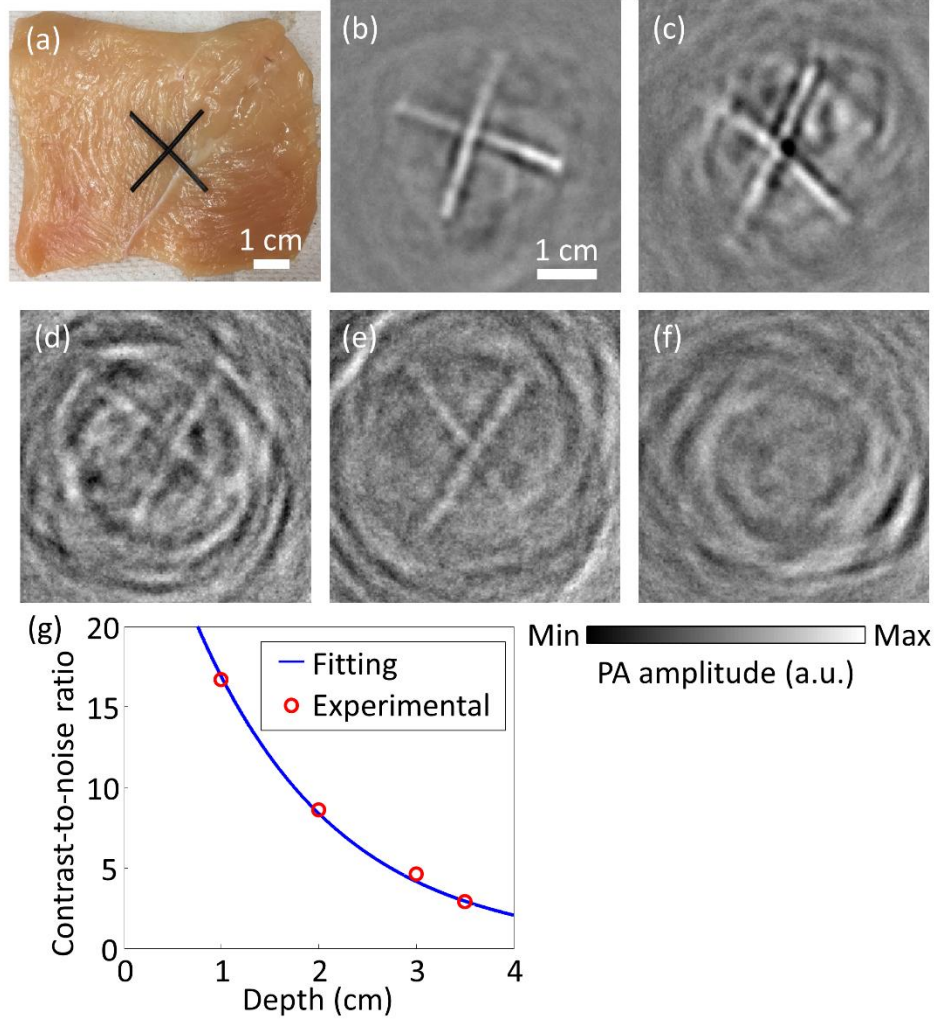
Figure 5.5 XFL-PACT of tissue phantoms made of latex cords sandwiched by chicken breast tissue with varied preset thicknesses. (a) Photograph of an exposed phantom with the top chicken breast tissue removed. (b)–(f) PACT images of the phantoms. The surrounding chicken breast tissue had thicknesses of (b) 1.0 cm, (c) 2.0 cm, (d) 3.0 cm, (e) 3.5 cm, and (f) 4.0 cm. (g) Plot of CNR versus the depth of the latex cords, showing both experimental data points and best fitting exponential decay curve.

5.3.4 Imaging of a Whole Mouse Body *In Vivo* with XFL-PACT

To demonstrate the full potential of flash-lamp-based PACT for blood imaging, we imaged blood-filled tubes, which were embedded 1 cm deep inside an agar-water gel (3%) without and with 1% intralipid (**Figs. 5.1f**, **5.6a** and **5.6b**). To image the blood, which is less absorbing than the latex cord, we replaced the single-element ultrasonic transducer with a ring-shaped ultrasonic transducer array with 512 elements to improve SNR by employing more averaging. In particular, 1000 times

averaging was used to image the blood-filled tube. We can clearly see the blood-filled tube in the clear medium phantom from the flash-lamp-excited image (**Fig. 5.6c**). The blood-filled tube can also be observed with sufficient contrast even inside the scattering medium at the same depth (**Fig. 5.6d**).
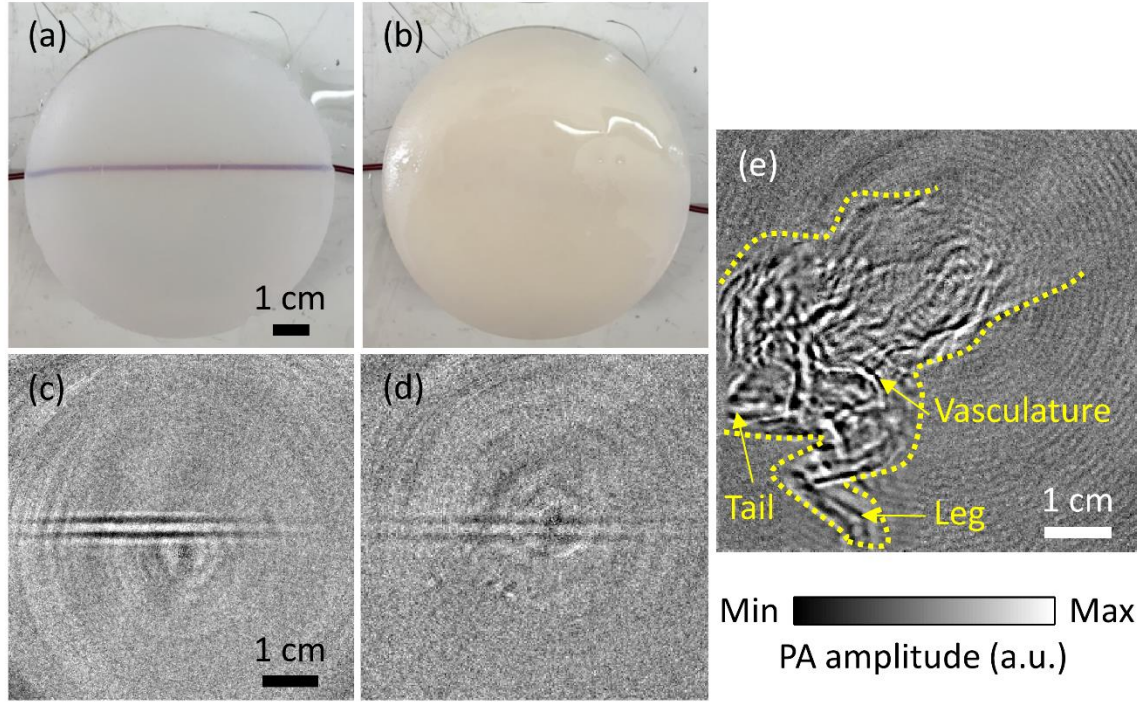
Figure 5.6 XFL-PACT of blood-filled tube phantoms made by embedding blood-filled tubes at a depth of 1 cm inside an agar-water gel without and with a scattering medium, and a whole mouse body *in vivo*. (a),(b) Photographs of the blood-filled tube phantoms without and with 1% intralipid, respectively. (c),(d) PACT images of the phantoms (a) and (b), respectively. (e) PACT image of the whole mouse body *in vivo*. Different structures, such as the vasculature, leg, and tail are labeled. The mouse body is also outlined with yellow dashed lines.

With, at the least, a 1 cm imaging depth for blood, we further imaged a whole mouse *in-vivo* (**Fig. 5.1g**) with 5000 times averaging. The mouse's body was completely immersed in water, but the head was above water so that the mouth could be connected to a tube supplying constant anesthetic gas (isoflurane). The flash-lamp-excited image is shown in **Fig. 5.6e**, with a CNR of 21.7. We can easily recognize different structures of the mouse, including the vasculature in the

70

body, legs, and tail. Note that mouse head was not imaged here because it was not immersed in water.

5.4 Conclusions and Discussions

To conclude, we have demonstrated the feasibility of using a single XFL as the illumination source for PACT. Taking CNR as the main concern, the optimal ultrasonic transducer for a XFL was found to be a focused one with a center frequency of 0.5 MHz. The average in-plane imaging resolution was ~1.5 mm within the imaging field-of-view. Different phantoms were used for validation, and all of them showed promising results. Flash-lamp-excited images showed structures similar to those in the laser-excited images, and the demonstrated maximum penetration depth for imaging black latex cords was 3.5 cm in the chicken breast tissue, which is around one-half of the maximum penetration depth reported by using lasers[34]. A blood-filled tube at a depth of 1 cm inside a scattering medium and a whole mouse body *in-vivo* can also be imaged with a single XFL illumination, which can open up many cost-effective applications for flash-lamp-based PACT. Using a single XFL with minimal optical and acoustic components, a complete PACT system can be appealingly compact and cheap, facilitating the usage of PAT in clinics and global healthcare. For example, with a safe XFL, it may be possible to implement an inexpensive and portable PA handheld probe to detect skin melanoma[98,99] and breast tumor in humans[100].

Chapter 6 Summary and Outlook

In this dissertation, we have developed PAT devices for translational medicine and basic science research, including UV-PAM for providing fast and multilayered histology of unprocessed human breast cancer without labels; automated mPAM system for achieving label-free and 3D imaging of whole organs; GRUV-PAM for extracting accurate 3D cell nuclear distributions and internal structures; XFL-PACT for low-cost deep tissue imaging.

In Chapter 2, we demonstrated that with UV laser illumination, UV-PAM system provides label-free and histology-like images of unprocessed breast cancer specimens. The multilayered imaging capability of UV-PAM provides additional information to pathologists for potentially more accurate diagnosis.

In Chapter 3, we developed the first automated mPAM system for label-free and whole-organ imaging with subcellular resolution. We have shown that mPAM is applicable to different organs (e.g., mouse brains, lung, and kidney) and commonly used embedding materials (e.g., paraffin and agarose). With more wavelengths, label-free mPAM has shown the ability to image DNA/RNA, hemoglobins, lipids, and cytochromes.

In Chapter 4, we upgraded our UV-PAM system with GR effect, which is named as GRUV-PAM. This upgrade allows GRUV-PAM to visualize the detailed 3D cell nuclear distributions and internal structures of a biological tissue (e.g., a mouse slice), further improving the accuracy of the multilayered imaging capability of UV-PAM.

In Chapter 5, we demonstrated that with a single XFL illumination, PACT images with comparable image quality acquired with laser illumination are obtained. We applied our XFL-

PACT system to image a tumor mimicking phantom at a depth up to 3.5 cm *ex vivo*, and to image a whole mouse body *in vivo*.

The application of UV-PAM to high-speed surgical margin determination is captivating. The next natural step is to improve the scanning speed of our UV-PAM to fulfill clinical needs. Imaging parallelization with multiple optical foci and a multi-element ultrasonic transducer array can be employed to reduce the scanning time by two to three orders of magnitudes.

The exploration of novel contrasts of PAT is still going on. For endogenous contrast imaging, we expect to include more endogenous contrasts, such as collagen in the near infrared range for label-free mouse brain imaging, and specific biomolecules at their "fingerprint" wavelengths in the mid-infrared range. By extending the wavelength range from UV to mid-infrared, we expect to provide a more complete map of all biomolecules without labeling and high fidelity.

The low-cost and highly portable capabilities of XFL-PACT open up new possibilities (e.g., low-cost deep tissue imaging in undeveloped countries). The broadband nature of a XFL also enables the potential for low-cost hyperspectral imaging of PACT, potentially imaging different biomolecules by adding optical filters.

References

1.   Wang, L. V & Yao, J. A practical guide to photoacoustic tomography in the life sciences. *Nat. Methods* **13,** 627–638 (2016).

2.   Wang, L. V. & Wu, H.-I. *Biomedical Optics: Principles and Imaging*. (Wiley, 2007).

3.   Hai, P., Zhou, Y., Liang, J., Li, C. & Wang, L. V. Photoacoustic tomography of vascular compliance in humans. *J. Biomed. Opt.* **20,** 126008 (2015).

4.   Hai, P., Zhou, Y., Gong, L. & Wang, L. V. Quantitative photoacoustic elastography in humans. *J. Biomed. Opt.* **21,** 66011 (2016).

5.   Hai, P., Yao, J., Li, G., Li, C. & Wang, L. V. Photoacoustic elastography. *Opt. Lett.* **41,** 725–728 (2016).

6.   Yao, J., Ke, H., Tai, S., Zhou, Y. & Wang, L. V. Absolute photoacoustic thermometry in deep tissue. *Opt. Lett.* **38,** 5228–5231 (2013).

7.   Jo, J., Lee, C. H., Kopelman, R. & Wang, X. In vivo quantitative imaging of tumor pH by nanosonophore assisted multispectral photoacoustic imaging. *Nat. Commun.* **8,** 471 (2017).

8.   Wong, T. T. W. *et al.* Fast label-free multilayered histology-like imaging of human breast cancer by photoacoustic microscopy. *Sci. Adv.* **3,** e1602168 (2017).

9.   American Cancer Society. Breast Cancer Facts & Figures 2017-2018. *Atlanta Am. Cancer Soc. Inc.* (2017).

10.   Moran, M. S. *et al.* Society of Surgical Oncology–American Society for Radiation Oncology Consensus Guideline on Margins for Breast-Conserving Surgery With Whole-Breast Irradiation in Stages I and II Invasive Breast Cancer. *J. Clin. Oncol.* **88,** 534–564 (2014).

74

11. van Dongen, J. A. *et al.* Long-term results of a randomized trial comparing breast-conserving therapy with mastectomy: European organization for research and treatment of cancer 10801 trial 4606. *J. Natl. Cancer Inst.* **92,** 1143–1150 (2000).

12. Park, C. C. *et al.* Outcome at 8 years after breast-conserving surgery and radiation therapy for invasive breast cancer: influence of margin status and systemic therapy on local recurrence. *J Clin Oncol* **18,** 1668–1675 (2000).

13. Kunos, C. *et al.* Breast conservation surgery achieving >= 2 mm tumor-free margins results in decreased local-regional recurrence rates. *Breast J.* **12,** 28–36 (2006).

14. Chagpar, A. B. *et al.* A Randomized, Controlled Trial of Cavity Shave Margins in Breast Cancer. *N. Engl. J. Med.* **373,** 503–510 (2015).

15. Pleijhuis, R. G. *et al.* Obtaining adequate surgical margins in breast-conserving therapy for patients with early-stage breast cancer: current modalities and future directions. *Ann. Surg. Oncol.* **16,** 2717–2730 (2009).

16. Peters, N. H. G. M. *et al.* Preoperative MRI and surgical management in patients with nonpalpable breast cancer: The MONET - Randomised controlled trial. *Eur. J. Cancer* **47,** 879–886 (2011).

17. Turnbull, L. *et al.* Comparative effectiveness of MRI in breast cancer (COMICE) trial: a randomised controlled trial. *Lancet* **375,** 563–571 (2010).

18. Allweis, T. M. *et al.* A prospective, randomized, controlled, multicenter study of a real-time, intraoperative probe for positive margin detection in breast-conserving surgery. *Am. J. Surg.* **196,** 483–489 (2008).

19. Karni, T. *et al.* A device for real-time, intraoperative margin assessment in breast-conservation surgery. *Am. J. Surg.* **194,** 467–473 (2007).

20. Coopey, S. B. *et al.* Lumpectomy Cavity Shaved Margins Do Not Impact Re-excision Rates in Breast Cancer Patients. *Ann. Surg. Oncol.* **18,** 3036–3040 (2011).

21. Krekel, N. M. A. *et al.* Intraoperative ultrasound guidance for palpable breast cancer excision (COBALT trial): A multicentre, randomised controlled trial. *Lancet Oncol.* **14,** 48–54 (2013).

22. Valdes, E. K., Boolbol, S. K., Cohen, J.-M. & Feldman, S. M. Intra-operative touch preparation cytology; does it have a role in re-excision lumpectomy? *Ann. Surg. Oncol.* **14,** 1045–1050 (2007).

23. Singletary, S. E. Surgical margins in patients with early-stage breast cancer treated with breast conservation therapy. *Am. J. Surg.* **184,** 383–393 (2002).

24. McCahill, L. E. *et al.* Variability in Reexcision Following Breast Conservation Surgery. *JAMA J. Am. Med. Assoc.* **307,** 467–475 (2012).

25. Abe, O. *et al.* Effects of radiotherapy and of differences in the extent of surgery for early breast cancer on local recurrence and 15-year survival: An overview of the randomised trials. *Lancet* **366,** 2087–2106 (2005).

26. Jeevan, R. *et al.* Reoperation rates after breast conserving surgery for breast cancer among women in England: retrospective study of hospital episode statistics. *Bmj* **345,** e4505 (2012).

27. Jacobs, L. Positive margins: the challenge continues for breast surgeons. *Ann. Surg. Oncol.* **15,** 1271–1272 (2008).

28. Lee, M. C. *et al.* Determinants of breast conservation rates: Reasons for mastectomy at a Comprehensive Cancer Center. *Breast J.* **15,** 34–40 (2009).

29. Jung, W. *et al.* Factors associated with re-excision after breast-conserving surgery for early-

stage breast cancer. *J. Breast Cancer* **15,** 412–419 (2012).

30. Balch, G. C., Mithani, S. K., Simpson, J. F. & Kelley, M. C. Accuracy of intraoperative gross examination of surgical margin status in women undergoing partial mastectomy for breast malignancy. *Am. Surg.* **71,** 22–28 (2005).

31. Huston, T. L., Pigalarga, R., Osborne, M. P. & Tousimis, E. The influence of additional surgical margins on the total specimen volume excised and the reoperative rate after breast-conserving surgery. *Am. J. Surg.* **192,** 509–512 (2006).

32. Kobbermann, A. *et al.* Impact of routine cavity shave margins on breast cancer re-excision rates. *Ann. Surg. Oncol.* **18,** 1349–1355 (2011).

33. Wang, L. V. Multiscale photoacoustic microscopy and computed tomography. *Nat. Photon.* **3,** 503–509 (2009).

34. Wang, L. V. & Hu, S. Photoacoustic Tomography: In Vivo Imaging from Organelles to Organs. *Science* **335,** 1458–1462 (2012).

35. Yao, D.-K., Maslov, K., Shung, K. K., Zhou, Q. & Wang, L. V. In vivo label-free photoacoustic microscopy of cell nuclei by excitation of DNA and RNA. *Opt. Lett.* **35,** 4139–4141 (2010).

36. Wang, L. V, Zhang, C., Zhang, S. & Yao, D. Label-free photoacoustic microscopy of cytochromes. *J. Biomed. Opt.* **18,** 20504 (2013).

37. Yao, J. *et al.* High-speed label-free functional photoacoustic microscopy of mouse brain in action. *Nat. Methods* **12,** 407–410 (2015).

38. Zhang, H. F., Maslov, K., Stoica, G. & Wang, L. V. Functional photoacoustic microscopy for high-resolution and noninvasive in vivo imaging. *Nat. Biotechnol.* **24,** 848–851 (2006).

39. Allen, T. J., Hall, A., Dhillon, A. P., Owen, J. S. & Beard, P. C. Spectroscopic photoacoustic

imaging of lipid-rich plaques in the human aorta in the 740 to 1400 nm wavelength range. *J. Biomed. Opt.* **17,** 61209 (2012).

40. Zink, D., Fische, A. H. & Nickerson, J. A. Nuclear structure in cancer cells. *Nat. Rev. Cancer* **4,** 677–687 (2004).

41. Yao, D.-K., Chen, R., Maslov, K., Zhou, Q. & Wang, L. V. Optimal ultraviolet wavelength for in vivo photoacoustic imaging of cell nuclei. *J. Biomed. Opt.* **17,** 56004 (2012).

42. Xia, J. *et al.* Wide-field two-dimensional multifocal optical-resolution photoacoustic-computed microscopy. *Opt. Lett.* **38,** 5236–5239 (2013).

43. Yu, K. *et al.* Predicting non-small cell lung cancer prognosis by fully automated microscopic pathology image features. *Nat. Commun.* **7,** 12474 (2016).

44. Hsiao, T.-C. *et al.* Deep-penetration photoacoustic array imaging of calcifications. *J. Biomed. Opt.* **18,** 66002 (2013).

45. Liberman, L. *et al.* The Breast Imaging Reporting and Data System: Positive Predictive Value of Mammographic Features and Final Assessment Categories. *Am. J. Roentgenol.* **73,** 35–40 (1998).

46. Baker, R., Rogers, K. D., Shepherd, N. & Stone, N. New relationships between breast microcalcifications and cancer. *Br. J. Cancer* **103,** 1034–1039 (2010).

47. Wang, L., Zhang, C. & Wang, L. V. Grueneisen relaxation photoacoustic microscopy. *Phys. Rev. Lett.* **113,** 174301 (2014).

48. Abdalla, F. *et al.* Correlation of Nuclear Morphometry of Breast Cancer in Histological Sections with Clinicopathological Features and Prognosis. *Anticancer Res.* **29,** 1771–1776 (2009).

49. Wong, T. T. W. *et al.* Label-free automated three-dimensional imaging of whole organs by

microtomy-assisted photoacoustic microscopy. *Nat. Commun.* **8,** 1386 (2017).

50. Amunts, K. *et al.* BigBrain: An Ultrahigh-Resolution 3D Human Brain Model. *Science* **340,** 1472–1475 (2013).

51. Lein, E. S. *et al.* Genome-wide atlas of gene expression in the adult mouse brain. *Nature* **445,** 168–176 (2007).

52. Li, A. *et al.* Micro-Optical Sectioning Tomography to Obtain a High-Resolution Atlas of the Mouse Brain. *Science* **330,** 1404–1408 (2010).

53. Ragan, T. *et al.* Serial two-photon tomography for automated ex vivo mouse brain imaging. *Nat. Methods* **9,** 255–258 (2012).

54. Hama, H. *et al.* Scale: a chemical approach for fluorescence imaging and reconstruction of transparent mouse brain. *Nat. Neurosci.* **14,** 1481–1488 (2011).

55. Chung, K. *et al.* Structural and molecular interrogation of intact biological systems. *Nature* **497,** 332–337 (2013).

56. Xu, Y., Pickering, J. G., Nong, Z. & Gibson, E. A Method for 3D Histopathology Reconstruction Supporting Mouse Microvasculature Analysis. *PLoS One* **10,** e0126817 (2015).

57. Ju, T. *et al.* 3D volume reconstruction of a mouse brain from histological sections using warp filtering. *J. Neurosci. Methods* **156,** 84–100 (2006).

58. Gibson, E. *et al.* 3D prostate histology image reconstruction: Quantifying the impact of tissue deformation and histology section location. *J Pathol Inf.* **4:31,** (2013).

59. Song, Y., Treanor, D., Bulpitt, A. J. & Magee, D. R. 3D reconstruction of multiple stained histology images. *J Pathol Inf.* **4:7,** (2013).

60. Wang, C., Gosno, E. B. & Li, Y. Fully automatic and robust 3D registration of serial-section

microscopic images. *Sci. Rep.* **5,** 15051 (2015).

61. Roberts, N. *et al.* Toward Routine Use of 3D Histopathology as a Research Tool. *Am J Pathol* **180,** 1835–1842 (2012).

62. Wang, H. *et al.* Label-Free Bond-Selective Imaging by Listening to Vibrationally Excited Molecules. *Phys. Rev. Lett.* **106,** 238106 (2011).

63. Ting, J. T., Daigle, T. L., Chen, Q. & Guoping, F. Acute brain slice methods for adult and aging animals: application of targeted patch clamp analysis and optogenetics. *Methods Mol Biol* **1183,** 221–242 (2014).

64. Zhang, C., Maslov, K. & Wang, L. V. Subwavelength-resolution label-free photoacoustic microscopy of optical absorption in vivo. *Opt. Lett.* **35,** 3195–3197 (2010).

65. Maslov, K. & Wang, L. V. In vivo photoacoustic microscopy with 7.6-µm axial resolution using a commercial 125-MHz ultrasonic transducer transducer. *J. Biomed. Opt.* **17,** 116016 (2012).

66. Lorenz, C., Carlsen, I., Buzug, T. M., Fassnacht, C. & Weese, J. A Multi-scale Line Filter with Automatic Scale Selection Based on the Hessian Matrix for Medical Image Segmentation. *Scale-sp. Theory Comput. Vis.* **1252,** 152–163

67. Shim, K. Vibratome Sectioning for Enhanced Preservation of the Cytoarchitecture of the Mammalian Organ of Corti. *J. Vis. Exp.* **17,** 2793 (2011).

68. Abdelaal, H. M. *et al.* Comparison of Vibratome and Compresstome sectioning of fresh primate lymphoid and genital tissues for in situ MHC-tetramer and immunofluorescence staining. *Bol. Proced. Online* **17,** 2 (2015).

69. Sallee, C. J. & Russell, D. F. Embedding of neural tissue in agarose or glyoxyl agarose for vibratome sectioning. *Biotech Histochem.* **68,** 360–368 (1993).

70. Johnson, G. A. *et al.* Waxholm space: an image-based reference for coordinating mouse brain research. *Neuroimage* **53,** 365–372 (2011).

71. Taruttis, A. & Ntziachristos, V. Advances in real-time multispectral optoacoustic imaging and its applications. *Nat Photon.* **9,** 219–227 (2015).

72. Hai, P., Yao, J., Maslov, K. I., Zhou, Y. & Wang, L. V. Near-infrared optical-resolution photoacoustic microscopy. **39,** 5192–5195 (2014).

73. Nedosekin, D. A., Sarimollaoglu, M., Shashkov, E. V, Ekaterina, I. & Zharov, V. P. Ultra-fast photoacoustic flow cytometry with a 0.5 MHz pulse repetition rate nanosecond laser. *Opt. Express* **18,** 8605–8620 (2010).

74. Wang, L., Maslov, K., Yao, J., Rao, B. & Wang, L. V. Fast voice-coil scanning optical-resolution photoacoustic microscopy. *Opt. Lett.* **36,** 139–141 (2011).

75. Song, L., Maslov, K. & Wang, L. V. Multifocal optical-resolution photoacoustic microscopy in vivo. *Opt. Lett.* **36,** 1236–1238 (2011).

76. Liu, X. *et al.* Label-free cell nuclear imaging by Grüneisen relaxation photoacoustic microscopy. *Opt. Lett.* **43,** 947–950 (2018).

77. Cox, B., Laufer, J. G., Arridge, S. R. & Beard, P. C. Quantitative spectroscopic photoacoustic imaging: a review. *J. Biomed. Opt.* **17,** 61202 (2012).

78. Xiang, L., Wang, B., Ji, L. & Jiang, H. 4-D photoacoustic tomography. *Sci. Rep.* **3,** 1113 (2013).

79. Danielli, A. *et al.* Label-free photoacoustic nanoscopy. *J. Biomed. Opt.* **19,** 86006 (2014).

80. Rønnov-Jessen, L., Petersen, O. W. & Bissell, M. J. Cellular changes involved in conversion of normal to malignant breast: importance of the stromal reaction. *Physiol. Rev.* **76,** 69–125 (1996).

81. Weigelt, B. & Reis-Filho, J. S. Histological and molecular types of breast cancer: is there a unifying taxonomy? *Nat. Rev. Clin. Oncol.* **6,** 718–730 (2009).

82. Petushi, S., Garcia, F. U., Haber, M. M., Katsinis, C. & Tozeren, A. Large-scale computations on histology images reveal grade-differentiating parameters for breast cancer. *BMC Med. Imaging* **6,** 14 (2006).

83. Benninger, R. K. P. & Piston, D. W. *Two-Photon Excitation Microscopy for the Study of Living Cells and Tissues. Curr. Protoc. Cell Biol.* **Chapter 4,** (2003).

84. Ma, J. *et al.* Grueneisen relaxation photoacoustic microscopy in vivo. *J. Biomed. Opt.* **21,** 66005 (2016).

85. Shi, J., Wang, L., Noordam, C. & Wang, L. V. Bessel-beam Grueneisen relaxation photoacoustic microscopy with extended depth of field. *J. Biomed. Opt.* **20,** 116002 (2015).

86. Tian, C., Xie, Z., Fabiilli, M. L., Wang, X. & Arbor, A. Imaging and sensing based on dual-pulse nonlinear photoacoustic contrast: a preliminary study on fatty liver. *Opt. Lett.* **40,** 2253–2256 (2015).

87. Wong, T. T. W. *et al.* Use of a single xenon flash lamp for photoacoustic computed tomography of multiple-centimeter-thick biological tissue ex vivo and a whole mouse body in vivo. *J. Biomed. Opt.* **22,** (2017).

88. Beard, P. Biomedical photoacoustic imaging. *Interface Focus* **1,** 602–631 (2011).

89. Wang, L. V. Tutorial on photoacoustic microscopy and computed tomography. *IEEE J. Sel. Top. Quantum Electron.* **14,** 171–179 (2008).

90. Allen, T. J. & Beard, P. C. Pulsed near-infrared laser diode excitation system for biomedical photoacoustic imaging. *Opt. Lett.* **31,** 3462–3464 (2006).

91. Zeng, L., Liu, G., Yang, D. & Ji, X. Portable optical-resolution photoacoustic microscopy

with a pulsed laser diode excitation. *Appl. Phys. Lett.* **102,** 53704 (2013).

92. Kolkman, R. G. M., Steenbergen, W. & van Leeuwen, T. G. In vivo photoacoustic imaging of blood vessels with a pulsed laser diode. *Lasers Med. Sci.* **21,** 134–139 (2006).

93. Upputuri, P. K. & Pramanik, M. Performance characterization of low-cost, high-speed, portable pulsed laser diode photoacoustic tomography (PLD-PAT) system. *Biomed. Opt. Express* **6,** 4118 (2015).

94. Allen, T. J. & Beard, P. C. High power visible light emitting diodes as pulsed excitation sources for biomedical photoacoustics. *Biomed. Opt. Express* **7,** 1260 (2016).

95. Adachi, Y. & Hoshimiya, T. Photoacoustic imaging with multiple-wavelength light-emitting diodes. *Jpn. J. Appl. Phys.* **52,** 07HB06 (2013).

96. Kruger, R. A. Photoacoustic Ultrasound.pdf. *Med. Phys.* **21,** 127–131 (1994).

97. Laser Institute of America New York. American National Standard for Safe Use of Lasers. **ANSI Z136.,** 1–2000 (2000).

98. Zhou, Y., Xing, W., Maslov, K. I., Cornelius, L. A. & Wang, L. V. Handheld photoacoustic microscopy to detect melanoma depth in vivo. *Opt. Lett.* **39,** 4731 (2014).

99. Zhou, Y. *et al.* Noninvasive Determination of Melanoma Depth using a Handheld Photoacoustic Probe. *J. Invest. Dermatol.* **137,** 1370–1372 (2017).

100. Diot, G. *et al.* Multispectral Optoacoustic Tomography (MSOT) of Human Breast Cancer. *Clin Cancer Res.* **23,** 6912–6923 (2017).

Vita

(Terence) Tsz Wai Wong

EDUCATION

Feb 2017 – present   **California Institute of Technology (Caltech)**

Ph.D. visiting student in Medical Engineering (MedE)

Sept 2013 – present   **Washington University in St. Louis (WUSTL)**

Ph.D. candidate in Biomedical Engineering (BME)

Sept 2011 – Aug 2013   **University of Hong Kong (HKU)**

M.Phil. in Electrical and Electronic Engineering (ELEC)

Sept 2008 – Aug 2011   **University of Hong Kong (HKU)**

B.Eng. in Medical Engineering (MedE)

(First Class Honors)

REFEREED JOURNAL PUBLICATIONS

1. Wen Bao, **Terence T. W. Wong**, Hsun-Chia Hsu, Yuecheng Shen, and Lihong V. Wang, "High-speed acoustic feedback based adaptive optics photoacoustic microscopy for microvascular imaging *in vivo*," (*manuscript in preparation*)

2. Yang Li, **Terence T. W. Wong**, Junhui Shi, and Lihong V. Wang, "Multifocal optical resolution photoacoustic microscopy through an ergodic cavity," (*manuscript in preparation*)

3. Hsun-Chia Hsu, Lei Li, Junjie Yao, **Terence T. W. Wong**, Junhui Shi, Konstantin Maslov, and Lihong V. Wang, "Dual-axis illumination photoacoustic microscopy for *in vivo* deep mouse brain imaging," (*submitted*)

4. Yuan Qu, Lei Li, Yuecheng Shen, Junjie Yao, **Terence T. W. Wong**, and Lihong V. Wang, "Dichroism-sensitive photoacoustic computed tomography," *Optica* (*accepted*)

5. Toru Imai, Junhui Shi, **Terence T. W. Wong**, Lei Li, Liren Zhu, and Lihong V. Wang, "High-throughput ultraviolet photoacoustic microscopy with multifocal excitation," *J. Biomed. Opt.* **23**(3), 036007 (2018)

6. Xiaowei Liu*, **Terence T. W. Wong***, Junhui Shi, Jun Ma, and Lihong V. Wang, "Label-free cell nuclear imaging by Grüneisen relaxation photoacoustic microscopy," *Opt. Lett.* **43**(4), 947-950 (2018) (*The authors contributed equally to the work)

7. Yan Liu, Yuecheng Shen, Haowen Ruan, Frank Bordie, **Terence T. W. Wong**, Changhuei Yang, and Lihong V. Wang, "Focusing light through *ex vivo* human cataract to stimulate retina with ultrasonically-guided wavefront shaping," *J. Biomed. Opt.* **23**(1), 010501 (2018)

8. **Terence T. W. Wong**, Ruiying Zhang, Chi Zhang, Hsun-Chia Hsu, Konstantin Maslov, Lidai Wang, Junhui Shi, Ruimin Chen, K. Kirk Shung, Qifa Zhou, and Lihong V. Wang, "Label-free automated three-dimensional imaging of whole organs by microtomy-assisted photoacoustic microscopy," *Nat. Commun.* **8**, 1386 (2017)

9. **Terence T. W. Wong**, Ruiying Zhang, Pengfei Hai, Chi Zhang, Miguel A. Pleitez, Rebecca L. Aft, Deborah V. Novack, and Lihong V. Wang, "Fast label-free multi-layered histology-like imaging of human breast cancer by photoacoustic microscopy," *Sci. Adv.* **3**, e1602168 (2017) *(also selected as the cover rotator story in Science Advances)*

10. **Terence T. W. Wong**, Yong Zhou, Alejandro Garcia-Uribe, Lei Li, Konstantin Maslov, Li Lin, Lihong V. Wang, "Use of a single xenon flash lamp for photoacoustic computed tomography of multiple-centimeter-thick biological tissue *ex vivo* and a whole mouse body *in vivo*," *J. Biomed. Opt.* **22**(4), 041003 (2016)

11. Junjie Yao, Lidai Wang, Joon-Mo Yang, Konstantin I. Maslov, **Terence T. W. Wong**, Lei Li, Chih-Hsien Huang, Jun Zou, and Lihong V. Wang, "High-speed label-free functional photoacoustic microscopy of mouse brain in action," *Nat. Methods* **12**(5), 407-410 (2015) *(also featured by Science, doi:10.1126/science.aab0393)*

12. Li Lin, Jun Xia, **Terence T. W. Wong**, Lei Li, and Lihong V. Wang, "*In vivo* deep brain imaging of rats using oral-cavity illuminated photoacoustic computed tomography," *J. Biomed. Opt.* **20**(1), 016019 (2015)

13. Xiaoming Wei, Andy K. S. Lau, **Terence T. W. Wong**, Chi Zhang, Kevin K. Tsia, and Kenneth K. Y. Wong, "Coherent laser source for high frame-rate optical time-stretch microscopy at 1.0 μm," *IEEE J. Sel. Top. In Quant. Electron.* **20**(5), 1100306 (2014)

14. Andy K. S. Lau, **Terence T. W. Wong**, Kenneth K. Y. Ho, Matthew T. H. Tang, Antony C. S. Chan, Edmund Y. Lam, Anderson H. C. Shum, Kenneth K. Y. Wong, and Kevin K. Tsia, "Interferometric time-stretch microscopy for ultrafast quantitative cellular and tissue imaging at 1 µm" *J. Biomed. Opt.* **19**(7), 076001 (2014)

15. Antony C. S. Chan, **Terence T. W. Wong**, Kenneth K. Y. Wong, Edmund Y. Lam, and Kevin K. Tsia, "Speed-dependent resolution analysis of ultrafast laser-scanning fluorescence microscopy," *J. Opt. Soc. Am. B* **31**(4), 755-764 (2014) *(also selected for publication in Virtual Journal for Biomedical Optics, Vol 9, Iss. 6, (2014))*

16. **Terence T. W. Wong**, Andy K. S. Lau, Kenneth K. Y. Ho, Matthew T. H. Tang, Joseph D. F. Robles, Xiaoming Wei, Antony C. S. Chan, Anson H. L. Tang, Edmund Y. Lam, Kenneth K. Y. Wong, Godfrey C. F. Chan, H. C. Shum, and Kevin K. Tsia, "Asymmetric-detection time-stretch optical microscopy (ATOM) for ultrafast high-contrast cellular imaging in flow," *Sci. Rep.* **4**, 3656 (2014)

17. **Terence T. W. Wong**, Andy K. S. Lau, Kenneth K. Y. Wong, and Kevin K. Tsia, "Optical time-stretch confocal microscopy at 1 μm," *Opt. Lett.* **37**(16), 3330 (2012) *(also selected for publication in Virtual Journal for Biomedical Optics, Vol 7, Iss. 10, (2012))*

CONFERENCE ABSTRACTS/PROCEEDINGS

1. **Terence T. W. Wong**, Xiaowei Liu, Junhui Shi, and Lihong V. Wang, "Photoacoustic microscopy for label-free optical sectioning cell nuclear imaging based on the Grüneisen relaxation effect," SPIE Photonics West 2018 BiOS, San Francisco, California, U.S.A, (Feb 2018) *(Finalist of the Best Paper Award: top 7 out of 248 papers)*

2. **Terence T. W. Wong**, Ruiying Zhang, Hsun-Chia Hsu, Konstantin Maslov, Junhui Shi, Ruimin Chen, K. Kirk Shung, Qifa Zhou, and Lihong V. Wang, "Whole-organ atlas imaged by label-free high-resolution photoacoustic microscopy assisted by a microtome," SPIE Photonics West 2018 BiOS, San Francisco, California, U.S.A, (Feb 2018)

3. **Terence T. W. Wong**, Ruiying Zhang, Pengfei Hai, Rebecca L. Aft, Deborah V. Novack, and Lihong V. Wang, "Photoacoustic microscopy enables multilayered histological imaging of human breast cancer without staining," SPIE Photonics West 2018 BiOS, San Francisco, California, U.S.A, (Feb 2018)

4. Yuan Qu, Lei Li, Yuecheng Shen, Junjie Yao, **Terence T. W. Wong**, and Lihong V. Wang, "Imaging dichroism by photoacoustic computed tomography," SPIE Photonics West 2018 BiOS, San Francisco, California, U.S.A, (Feb 2018)

5. **Terence T. W. Wong**, Yong Zhou, Alejandro Garcia-Uribe, Lei Li, Konstantin Maslov, and Lihong V. Wang, "Photoacoustic tomography using a single xenon flash lamp," SPIE Photonics West 2015 BiOS, San Francisco, California, U.S.A, (Feb 2015)

6. Ruiying Zhang, **Terence T. W. Wong**, Chi Zhang, Konstantin Maslov, Lidai Wang, Ruimin Chen, Deborah V. Novack, Rebecca L. Aft, Qifa Zhou, and Lihong V. Wang, "Margin analysis of biological specimens with photoacoustic microscopy," SPIE Photonics West 2015 BiOS, San Francisco, California, U.S.A, (Feb 2015)

7. Li Lin, Jun Xia, **Terence T. W. Wong**, Lei Li, and Lihong V. Wang, "Photoacoustic imaging with internal illumination," SPIE Photonics West 2015 BiOS, San Francisco, California, U.S.A, (Feb 2015)

8. Xiaoming Wei, Andy K. S. Lau, **Terence T. W. Wong**, Chi Zhang, Kevin K. Tsia, Kenneth K. Y. Wong, "Coherent laser source for optical time-stretched microscopy," Conference on Lasers and Electro Optics/Quantum Electronics and Laser Science Conference (CLEO/QELC), San Jose, California, U.S.A, (June 2014)

9. Antony C. S. Chan, **Terence. T. W. Wong**, Edmund Y. Lam, Kevin K. Tsia, "Revisit laser scanning fluorescence microscopy performance under fluorescence-lifetime-limited regime," SPIE Photonics West 2014 BiOS, San Francisco, California, U.S.A, (Feb 2014)

10. **Terence T. W. Wong**, Andy K. S. Lau, Matthew Y. H. Tang, Kenneth K. Y. Ho, Kenneth K. Y. Wong, Anderson H. C. Shum, Kevin K. Tsia, "Asymmetric-detection time-stretch optical microscopy (ATOM) for high-contrast and high-speed microfluidic cellular imaging," SPIE Photonics West 2014 BiOS, San Francisco,

California, U.S.A, (Feb 2014)

11. Andy K. S. Lau, **Terence T. W. Wong**, Kenneth K. Y. Ho, Matthew Y. H. Tang, Joseph D. F. Robles, Xiaoming Wei, Antony C. S. Chan, Anson H. L. Tang, Edmund Y. Lam, Kenneth K. Y. Wong, Godfrey C. F. Chan, H. C. Shum, and Kevin K. Tsia, "Ultrafast high-contrast microfluidic cellular imaging by asymmetric-detection time-stretch optical microscopy (ATOM)," **(Postdeadline paper)** 2013 Frontiers in Optics/Laser Science XXIX (FiO/LS), in Orlando, Florida, (Oct 2013)

12. Andy K. S. Lau, **Terence T. W. Wong**, Kenneth K. Y. Wong, Kevin K. Tsia, "Megahertz-scan-rate quantitative tissue imaging by interferometric time-stretch microscopy," in Asia Communications and Photonics Conference (ACP), Beijing, China, (Dec 2013)

13. Kevin K. Tsia, Kenneth K. Y. Wong, Andy K. S. Lau, **Terence T. W. Wong**, "Optical Time-Stretch Microscopy for ultrafast Optofluidic Imaging," 7th International Conference on Nanophotonics/3rd Conference on Advances in Optoelectronics and Micro/Nano Optics (ICNP/AOM), Hong Kong, China, (May 2013) *(INVITED)*

14. **Terence T. W. Wong**, Matthew Y. H. Tang, Andy K. S. Lau, Antony C. S. Chan, Edmund Y. Lam, Kenneth K. Y. Wong, Anderson H. C. Shum, Kevin K. Tsia, "Ultrafast flow imaging by 1 μm time-stretch microscopy," Novel Techniques in Microscopy (NTM), paper NW1B.5, Waikoloa Beach, Hawaii, USA, (Apr 2013)

15. Andy K. S. Lau, **Terence T. W. Wong**, Antony C. S. Chan, Edmund Y. Lam, Kenneth K. Y. Wong, Kevin K. Tsia, "Interferometric time-stretch microscopy for ultrafast quantitative cellular imaging at 1 μm," Novel Techniques in Microscopy (NTM), paper NW1B.4, Waikoloa Beach, Hawaii, USA, (Apr 2013)

16. **Terence T. W. Wong**, Yi Qiu, Andy K. S. Lau, JingJiang Xu, Antony C. S. Chan, Kenneth K. Y. Wong, Kevin K. Tsia, "Cost effective approaches for high-resolution bioimaging by time-stretched confocal microscopy at 1μm," Photonics Asia, paper 8853-65, Beijing, China, (Nov 2012)

17. **Terence T. W. Wong**, Andy K. S. Lau, Kenneth K. Y. Wong, Kevin K. Tsia, "Cellular imaging by time-stretch confocal microscopy in the 1μm window," Frontier in Optics/Laser Science XXVIII (FiO/LS) meeting, paper FTu1C.3, Rochester, New York, USA, (Oct 2012)

18. **Terence T. W. Wong**, Antony C. S. Chan, Kenneth K. Y. Wong, Kevin K. Tsia, "Pixel super-resolution in serial time-encoded amplified microscopy (STEAM)," in Conference on Lasers and Electro Optics / Quantum Electronics and Laser Science Conference (CLEO/QELC), paper CTu3J.4, San Jose, California, USA, (May 2012)

BOOK CHAPTER

Andy K. S. Lau, **Terence T. W. Wong**, Ho Cheung Shum, Kenneth K. Y. Wong, Kevin K. Tsia, *"Ultrafast Microfluidic Cellular Imaging by Optical Time-Stretch," Imaging Flow Cytometry: Methods and Protocols, (Methods in Molecular Biology)*, Humana Press Inc. (2015)

PATENT

Kevin K. Tsia, **Terence T. W. Wong**, Andy K. S. Lau, and Anson H. L. Tang. "Apparatus and Methods for quantitative phase-gradient chirped-wavelength-encoded optical imaging," US pending patent (No. US20160327776 A1).

PROFESSIONAL ACTIVITY

Reviewer of Journal *Scientific Reports*, *Biomedical Optics Express*, *Optics Communications*, and *The Scientific World Journal*.